A WATER-SOLUBLE COBALT SULFIDE SUPERATOM FOR FLOW BATTERY APPLICATIONS AND CRYSTALLINE FRAMEWORK SYNTHESIS

by

Matthew B. Freeman

A thesis submitted to the faculty of
The University of North Carolina at Charlotte
in partial fulfillment of the requirements
for the degree of Master of Science in
Chemistry

Charlotte

2019

Approved by:

Dr. Christopher M. Bejger

Dr. Daniel Rabinovich

Dr. Bernadette T. Donovan-Merkert

Dr. Stuart T. Smith

ABSTRACT

MATTHEW BRIAN FREEMAN. A Water-soluble Cobalt Sulfide Superatom for Flow
Battery Applications and Crystalline Framework Synthesis (Under the direction of
DR. CHRISTOPHER M. BEJGER)

Metal sulfide clusters are attractive components for flow batteries owing to the abundance of their constituent atoms and their tunable size, solubility, and redox properties. We prepared an atomically precise cobalt sulfide cluster, $Co_6S_8(PTA)_6{\bullet}4HCl$ (PTA = 1,3,5-triaza-7-phosphaadamantane) (**1**), in a single step using low-cost precursors and water solubilizing phosphine ligands. Compound **1** represents the first structurally characterized, water-soluble cobalt-sulfide cluster. Remarkably, cluster **1** undergoes two electrochemically reversible oxidations in aqueous solutions and is stable in air. The first redox process is chemically reversible during charge–discharge experiments using a static cell and aqueous solutions of NaCl. An aqueous cell comprising methyl viologen (MV^{2+}) as the anolyte and an anion exchange membrane provides an operating $V_{cell} = 0.63$ V.

Additionally, cluster **1** was used as a preformed metalloligand in the synthesis of a novel coordination solid. Heating a 1:2 mixture $Co_6S_8(PTA)_6{\bullet}4HCl$ and CuI in a solution of acetonitrile/water under solvothermal conditions leads to the formation of dark black crystals. The resulting three-dimensional framework (**2**) contains three distinct cluster constituents ($2[Co_6S_8(PTA)_6{\bullet}H^+]{\bullet}2[Cu_4I_4]{\bullet}[Cu_4I_6^{2-}]$) and exhibits reversible redox behavior in the solid state. Framework **2** was structurally characterized using single crystal X-ray diffraction and powder X-ray diffraction. The UV-Vis diffuse reflectance spectrum of framework **2** was measured and used to calculate the band gap (1.98 eV) based on the Kubelka-Munk function.

ACKNOWLEDGEMENTS

I would like to thank my research advisor Dr. Christopher Bejger first and foremost amongst those who have helped me along the way. I first met Dr. Bejger at a meet and greet pizza party as a humble undergraduate. Thankfully I was permitted to join your research laboratory, to become the first student to work under you at UNCC. The mentoring you provided me has allowed me to build a great amount of experience ranging from troubleshooting laboratory equipment and synthetic issues to social and communication skills. You have helped inspire me to become the researcher I am today. I have enjoyed the past 4 years working for you and it will be a bitter sweet moment leaving lab while graduating from UNCC.

A lot of work could not have been done without the assistance from the others working around me in the laboratory. I learned as much from them as they did from me. Jessica Shott was the first graduate student who worked alongside of me. Thank you for keeping an eye on me during your time here and for helping me learn the ways of research. Dr. Le Wang also played a large part in my research, your lessons about crystallography and secrets to the art of growing beautiful crystals are priceless. I do appreciate the bits of mandarin you taught to me, your hieroglyphics still continue to decorate the glass of our fume hoods. Ozi “Lil Debbie” Edokobi was an undergraduate who I had the pleasure of working with during my last year. Out of the many people who thought our chemistry stinks, it did not stop you from braving up to the hydrogen sulfide reaction! This next publication could not have been completed so timely without your assistance. Lastly, I would like to thank Jonathan for making lab a fun place to work and continuing to keep me sharp by always asking me for the “Why?” behind all things I say.

Thank you to all of my committee members: Dr. Donovan Merkert, Dr. Stuart Smith, and Dr. Dan Rabinovich, who made the time to guide me through my Master of Science degree. Without the advice and guidance given to me, this work would not be what it currently is today. Others outside of my lab group have also contributed to my successful graduate career. Dr. Craig Ogle and Adam “The Juice” Fessler have always offered good advice, always allowed me to borrow odds and ends, and have kept a hot pot of coffee readily available for those in need. Dr. Cliff Carlin and Dr. Jon Merkert were always willing to assist me when there were issues with our electrochemical experiments. Their wisdom helped us build up to our full asymmetrical H-cell experiment. I would like to acknowledge Dr. Dan Jones and Margret for helping us obtain all of our needed crystal data. These structures played an important role in all of our manuscripts. I would also like to thank Dr. Markus Etzkorn who always ensured that I was on track and for trying to help whenever we seemed unsure. Lastly, I need to thank Dr. Michael Walter who always gave us helpful suggestions and collaboratively worked with us allowing us to make efficient progress on our projects.

I greatly appreciate the generous support of Dr. Thomas D. Walsh. The fellowship allowed me to support my growing family at home while making great amounts of progress on my research. This fellowship did not only benefit me but those in lab around me. Without having the responsibilities of teaching and grading classes, I had the opportunity to mentor and teach those working alongside me, so they too can benefit from my growing experience.

Last of all, I would like to thank my family for pushing me to where I am today. My parents have generously helped me though my college career and I would not be at the

point I am now without their constant support. I would like to thank my wife, Dioema, and my step daughter, Ninel, for keeping me happy and ensuring I always had a hot meal to eat and clean clothes (gym shorts) to wear. Without you guys I’d probably look like a caveman that lived under a rock. Alessandro, thank you for being my alarm clock every morning at 7:30 AM sharp. I can always rely on you to get me up no matter the amount of sleep I got during the night.

TABLE OF CONTENTS

CHAPTER1: COBALT SULFIDE OCTAHEDRAL CLUSTERS FOR AQUEOUS REDOX FLOW BATTERIES 1

1.1 Introduction 1

1.1.1 Redox Flow Batteries 1

1.1.2 Fabrication Considerations 4

1.1.3Performance Analysis 9

1.1.4 State of the Art 11

1.1.5 Metal Sulfide Clusters 15

1.1.6 Research Objectives 18

1.2 Results and Discussion 20

1.2.1 Synthesis and Structural Characterization of $Co_6S_8(PTA)_6$•4HCl 20

1.2.2 Solubility 23

1.2.3 Electrochemical Characterization by Cyclic Voltammetry 25

1.2.4 Cost Analysis 30

1.2.5 Symmetrical H-cell Fabrication and Performance Analysis 31

1.2.6 Asymmetrical H-cell Fabrication and Performance Analysis 34

1.3 Experimental Details 38

1.3.1 General Synthetic Information 38

1.3.2 Synthesis of $Co_6S_8(PTA)_6$•4HCl 38

1.3.3 Conclusion 39

1.3.4 Future Work 40

CHAPTER 2: $Co_6S_8(PTA)_6$: A SUPERATOMIC METALLOLIGAND FOR ORDERED TERNARY CLUSTER SOLIDS 42

2.1 Introduction 42

2.1.1 Clusters as Building Block in Solid-State Materials 42

2.1.2 Multicluster Ionic Solids: Salt Metathesis and Charge Transfer 43

2.1.3 Multicluster Coordination: In-Situ Formation 44

2.1.4 Multicluster Formation: Post Synthetic Modification 46

2.1.5 Multicluster Formation: Metalloligand Linker 48

2.1.6 Research Objectives 51

2.2 Results and Discussion 52

1.2.5 Synthesis and Structural Characterization of $2[Co_6S_8(PTA)_6H^+]•2[Cu_4I_4]•[Cu_4I_6^{2-}]$ 52

2.2.2 Thermogravimetric Analysis 55

2.2.3 Cyclic Voltammetry 56

2.2.4 Photophysical Measurements 58

2.3 Experimental Details 60

2.3.1 General Synthetic Information 60

2.3.2 Synthesis of $2[Co_6S_8(PTA)_6H^+]•2[Cu_4I_4]•[Cu_4I_6^{2-}]$ 61

2.3.3 Conclusion 61

2.3.4 Future Work 61

REFERENCES 63

APPENDIX A: INSTRUMENTATION & DATA COLLECTION FOR $Co_6S_8(PTA)_6•4HCl$ 69

APPENDIX B: CRYSTAL DATA FOR $Co_6S_8(PTA)_6•4HCl$ 71

APPENDIX C: SOLUBILITY EXPERIMENTS FOR $Co_6S_8(PTA)_6•4HCl$ 72

APPENDIX D: WATERGATE ^{1}H NMR SPECTRUM OF $Co_6S_8(PTA)_6$•4HCl (D_2O, 500 MHz, 25 ^oC) 74

APPENDIX E: WATERGATE ^{1}H NMR SPECTRUM OF $Co_6S_8(PTA)_6$•4HCl (D_2O/Sat K_2CO_3, 500 MHz, 25 ^oC) 75

APPENDIX F: ^{31}P NMR OF $Co_6S_8(PTA)_6$•4HCl (D_2O, 500 MHz, 25 ^oC) 76

APPENDIX G: EVANS METHOD SAMPLE PREPARATION 77

APPENDIX H: ELECTROCHEMICAL CONSTANT EXPERIMENTS 78

APPENDIX I HALF-CELL PARAMETERS WITH THEORETICAL CAPACITY CALCULATION SAMPLE 79

APPENDIX J: FULL CELL EXPERIMENT 81

APPENDIX K: INSTRUMENTATION & DATA COLLECTION FOR $2[Co_6S_8(PTA)_6H^+]$•$2[Cu_4I_4]$•$[Cu_4I_6{}^{2-}]$ 82

APPENDIX L: CRYSTAL DATA FOR $2[Co_6S_8(PTA)_6H^+]$•$2[Cu_4I_4]$•$[Cu_4I_6{}^{2-}]$ 84

APPENDIX M: POWDER X-RAY DIFFRACTION (PXRD) 85

APPENDIX N: SCANNING ELECTRON MICROSCOPY IMAGES OF $2[Co_6S_8(PTA)_6H^+]$•$2[Cu_4I_4]$•$[Cu_4I_6{}^{2-}]$ 86

APPENDIX O: MODIFIED GLASSY CARBON ELECTRODE WITH $2[Co_6S_8(PTA)_6H^+]$•$2[Cu_4I_4]$•$[Cu_4I_6{}^{2-}]$ 87

LIST OF TABLES

TABLE 1.1. Tabulated values of the electrochemical window at different electrode surfaces under different conditions in aqueous solutions. 5

TABLE 1.2. The calculated solubility and adsorption coefficients from experimentally obtained data in both deionized (DI) water and hydrochloric acid solutions. (Reproduced from ref 9 with permission from The Royal Society of Chemistry.) 24

TABLE 1.3. Change in potential of 1 mM **1** in a citric acid and sodium phosphate dibasic buffer at various pH. Cyclic voltammograms were run at 100 mV s^{-1} on a GCE and referenced versus a Ag/AgCl electrode with the report potential for the monocation only. 26

TABLE 1.4. Experimentally determined diffusion and electron transfer coefficient tested in both salt water and acidic solutions. (Reproduced from ref 9 with permission from The Royal Society of Chemistry.) 29

TABLE 1.5. Preliminary cost analysis for preparation of **1**. (Reproduced from ref 9 with permission from The Royal Society of Chemistry.) 30

TABLE 1.6. Price comparison of active electrolytes estimated on an industrial scale. .. 31

TABLE 1.7. Experimentally measured concentration of **1** calculated through the capacity. (Reproduced from ref 9 with permission from The Royal Society of Chemistry.).. 36

LIST OF FIGURES

FIGURE 1.1. General scheme of a redox flow battery (RFB)... 2

FIGURE 1.2. A plot of power output versus time for a 30 MW wind farm (red), 6 MW vanadium flow battery (blue), and the smoothed overall output (black). (Reprinted with permission from ref 6. Copyright 2013 Sumitomo Electric.).. 3

FIGURE 1.3. Cost of a) solvent and b) electrolyte based on market prices of 4L HPLC grade solvents and 98% pure electrolytes from Sigma Aldrich (2019). Solvent List: Nitromethane, (NM); propylene carbonate (PC); N,N-dimethylformamide (DMF); acetonitrile (MeCN); tetrahydrofuran (THF); dichloromethane (DCM); water (H_2O). Electrolyte List: Tetraethylammonium hexafluorophosphate ($TEAPF_6$); tetrabutylammonium tetrafluoroborate ($TBABF_4$); tetrabutylammonium hexafluorophosphate ($TBAPF_6$); sulfuric acid (H_2SO_4); hydrochloric acid (HCl); sodium chloride (NaCl).. 4

FIGURE 1.4. Open circuit potential (E_{oc}) of the ARFB dependence on the half reaction potentials of the anolyte (E_a) and catholyte (E_c). 6

FIGURE 1.5. Elemental abundance on Earth sorted by atomic number and normalized against silicon... 7

FIGURE 1.6. The cost analysis of a vanadium redox flow battery (VFB) for the a) power intensive case (0.25 MWh) and the b) energy intensive case (4 MWh) (Reprinted with permission from ref 8. Copyright 2012 Elsevier.)....... 8

FIGURE 1.7. The cell design of an a) asymmetric H-cell and a b) symmetric H-cell..... 11

FIGURE 1.8. Graphical depiction of the current commercial VFB. (Reprinted with permission from ref 16. Available under Creative Commons Attribution License (CC BY))..... 12

FIGURE 1.9. a) Graphical depiction (left) of commercially available 2,6-DHAQ (blue) anolyte coupled to a ferricyanide (gold) catholyte in a high pH ARFB tested by Marshack and coworkers with the cyclic voltammogram of the active species (right). b) Structure of 2,6-DHAQ used by Marshack and Aziz's derivative 2,6-DBEAQ. (Reprinted (adapted) with permission from ref 21. Copyright 2015 The American Association for the Advancement of Science.).. 13

FIGURE 1.10. A graphical depiction of an ARFB using a water-soluble ferrocene derivative as the catholyte (red/green) and methyl viologen as the anolyte (purple) reported by Long and coworkers. (Reprinted (adapted) with permission from ref 5. Copyright 2017 American Chemical Society.) 14

FIGURE 1.11. Common geometries of MSCs with trigonal bipyramidal, tetrahedral, octahedral, and oligomeric depicted, respectively. 15

FIGURE 1.12. Single crystal X-ray diffraction (SCXRD) structure of an IspH protein complexed with dimethallyl diphosphate (DMAPP) with the iron (rust red) and sulfur (yellow) seen bound in the middle. 16

FIGURE 1.13. The cone angle of various phosphines compared to their donation strength, with bulkier phosphines at larger cone angle. (Reprinted with permission from ref 37. Copyright 2015 American Chemical Society.) 17

FIGURE 1.14. Common water-soluble phosphines previously synthesized within the literature. Ligands Depicted: 1,3,5-triaza-7-phosphaadamantane (PTA); 3,7-diacetyl-1,3,7-triaza-5-phosphabicyclo[3.3.1]nonane (DAPTA); 1,4,7-triaza-9-phosphatricyclo[5.3.2.1]tridecane (CAP); tris(dimethylamino)phosphine (TDAP); 3,3',3"-phosphanetriyltris(benzenesulfonic acid) trisodium salt (TPPTS).. 19

FIGURE 1.15. Ball-and-stick X-ray crystal structure of $Co_6S_8(PTA)_6$•4HCl (1) as viewed from the side and top, respectively. Color scheme: Carbon, black; chlorine, green; cobalt, dark blue; nitrogen, light blue; phosphorus, orange; sulfur, yellow. (Reproduced from ref 9 with permission from The Royal Society of Chemistry.) 21

FIGURE 1.16. Crystal structure of **1** shown in a space-filling model with cobalt, dark blue; sulfur, yellow; phosphorus, orange; carbon, black; nitrogen, light blue; chlorine, green with hydrogens omitted for clarity. (Reproduced from ref 9 with permission from The Royal Society of Chemistry.) 21

FIGURE 1.17. The packing of the **1** as seen by the a) a-view, b) b-view, and c) c-view. 22

FIGURE 1.18. ^{1}H NMR solvent peak of **1** (35% DCl in D_2O, 300 MHz, 25 ºC) with a capillary of pure DCl solution sealed within the NMR tube. (Reproduced from ref 9 with permission from The Royal Society of Chemistry.) 23

FIGURE 1.19. UV-vis spectrum of 7.5 µM $Co_6S_8(PTA)_6$•4HCl in a 0.1 M HCl solution. (Reproduced from ref 9 with permission from The Royal Society of Chemistry.) 24

FIGURE 1.20. CV of 1 mM $Co_6S_8(PTA)_6$•4HCl in 0.5 M NaCl referenced against an Ag/AgCl electrode and taken on a GCE WE at 100 mV s^{-1}. (Reproduced from ref 9 with permission from The Royal Society of Chemistry.) 25

FIGURE 1.21. A 1 mM solution of **1** with a) 0.5 M NaCl or b) 1 M HCl supporting electrolyte referenced against an Ag/AgCl electrode and scanned at 100 mV s^{-1} on a GCE WE. (Reproduced from ref 9 with permission from The Royal Society of Chemistry.) 27

FIGURE 1.22. Symmetrical H-cell set up with the CF WE (blue/green connection), Ag/AgCl RE (white connection), and CF CrE (red connection) connected to a Gamry 1000E potentiostat, separated by a Selemion AMV anion exchange membrane, and sealed with a DuPont Kalrez perfluoroester O-ring. 32

FIGURE 1.23. CCD curves of a) the $Co_6S_8/Co_6S_8^+$ redox couple, b) the $Co_6S_8/Co_6S_8^{2+}$ redox couple, c) the capacity retention for the $Co_6S_8/Co_6S_8^+$ redox couple, and d) the pre and post in cell CV of **1** on CF. All cells were set up with 4 mL of **1** (1 mM, 1 M NaCl, H_2O) per side and measured against a Ag/AgCl RE. (Reproduced from ref 9 with permission from The Royal Society of Chemistry.) 33

FIGURE 1.24. Asymmetrical H-cell with a) the graphical depiction and b) the actual cell used. The purple solution contains 4 mL of $MV^{•+}$ (2.5 mM, 1 M NaCl, H_2O) and the brown solution contains 4 mL of $Co_6S_8(PTA)_6^+$ (2.5 mM, 1 M NaCl, H_2O) under an argon atmosphere, separated by Selemion AMV anion exchange membrane, and sealed by a DuPont Kalrez perfluoroester O-ring, and connected to an external circuit through solid graphite electrodes (SGEs). (Reproduced from ref 9 with permission from The Royal Society of Chemistry.) 34

FIGURE 1.25. Asymmetric H-cell performance depicted with a) the CCD curves and b) the CE and EE denoted by dotted lines. The charging and discharging capacities denoted as smooth lines. (Reproduced from ref 9 with permission from The Royal Society of Chemistry.) 35

FIGURE 1.26. Common water-soluble phosphines previously synthesized within the literature. Depicted: 1,3,5-triaza-7-phosphaadamantane (PTA); 3,7-diacetyl-1,3,7-triaza-5-phosphabicyclo[3.3.1]nonane (DAPTA); 1,4,7-triaza-9-phosphatricyclo[5.3.2.1]tridecane (CAP); tris(dimethylamino)phosphine (TDAP); 3,3’,3”-phosphanetriyltris(benzenesulfonic acid) trisodium salt (TPPTS) 40

FIGURE 1.27. Crystal structure of $Fe_4S_4(CN)_4^{4-}$. Color scheme: Iron, red; sulfur, yellow; carbon, black; nitrogen, blue. 41

FIGURE 2.1. Synthetic map of various approaches to forming multicluster solids......... 43

FIGURE 2.2. Cluster salt crystal structures of a) $[Au_8(PPh_3)_8][C_{60}]_2$ formed by salt metathesis (Reprinted with permission from ref 71. Copyright 2008 John Wiley & Sons.) and b) $[Co_6Te_8(PEt_3)_6][Fe_8O_4pz_{12}Cl_4]$ formed through charge transfer. (Reprinted (adapted) with permission from ref 68. Copyright 2014 American Chemical Society.) 44

FIGURE 2.3. Structures of in-situ formation of $Ti_6O_4(O\textit{i}Pr)_{10}(O_3P\text{-}Phen)_2(L)_2\ Cu_yX_y$ (L = isonicotinic acid, nicotinic acid, pyridine-3-sulfonic acid, 2-pyrazine-carboxylic acid, or 1,4-diazabicyclo[2.2.2]octane; y = 2, 4; X = Cl, I) coordination polymers. Color Scheme: $(Ti_6O_4(O\textit{i}Pr)_{10}(O_3P\text{-}Phen)_2$, green box; light blue, copper; pink, iodide; gold, iodide or chloride; red, oxygen; yellow, phosphorus or sulfur; black, carbon; dark blue, nitrogen.(Reprinted (adapted) with permission from ref 72. Copyright 2017 American Chemical Society.). 45

FIGURE 2.4. Formation of the a) Cu6S6 and Cu4I4 cluster framework using a thiol containing diatopic linker and b) the crystal structure obtained from SCXRD. Color Scheme: Light blue, copper; yellow, iodide; purple, sulfur; gray, carbon; dark blue, nitrogen; and hydrogens have been omitted for clarity. (Reproduced from ref 66 with permission from The Royal Society of Chemistry.) 46

FIGURE 2.5. The a) SEM of UiO-66 with the unmodified linker (left) and modified linker (right) with b) the molecular depiction. (Reprinted with permission from ref 80. Copyright 2013 American Chemical Society https://pubs.acs.org/doi/10.1021/ja407176p.) 47

FIGURE 2.6. An indium oxide cluster with an a) open metal site and b) complexes formed using the post synthetically installed hook. (Reprinted (adapted) with permission from ref 81. Copyright 2013 American Chemical Society.) 48

FIGURE 2.7. The crystal structure of Prussian Blue consisting of iron cations coordinated to the nitrogens of the ferrocyanide anion. Color Scheme: Blue, nitrogen; carbon, black; red-orange, iron....... 49

FIGURE 2.8. Linear POM synthesized in (1) using copper (I) iodide SBUs to create ordered polymeric framework (2) or (3). (Reprinted with permission from ref 89. Copyright 2016 John Wiley & Sons.)............................. 50

FIGURE 2.9. A 2D and 3D accessible redox active SAF based around the redox active Co6Se8(PEt2BzCOOH)6 superatom monomer with zinc oxide SBUs. Color Scheme: Green, selenium; blue, cobalt; orange, phosphine; grey, carbon; red, oxygen; and hydrogens were omitted for clarity. (Reprinted with permission from ref 90. Copyright 2017 American Chemical Society https://pubs.acs.org/doi/10.1021/acscentsci.7b00328.)........................ 51

FIGURE 2.10. The SCXRD structure of the different clusters within 2 a) the asymmetrical unit, b) the neutral Cu_4I_4 cluster, c) the anionic $Cu_4I_6^{2-}$ ladder cluster, and d) 1 as found with distortions in the packing. Color Scheme: Dark blue, cobalt; yellow, sulfur; orange, phosphorus; teal, copper; purple, iodide; light blue, nitrogen; black, carbon; hydrogens have been omitted for clarity.. 54

FIGURE 2.11. The thermogravimetric analysis of the metalloligand (black) and SAF 2 (red) under compressed air (solid line) and inert atmosphere (dashed). The sample was tested from 30 – 1000 ºC at a ramp rate of 5 ºC/min. 56

FIGURE 2.12. Cyclic voltammograms of a) 2 (black, solid state modified GCE WE, 100 mV/s, 0.5 M NaCl supporting electrolyte) and 1 mM Co6S8(PTA)6 (red, GCE WE, 500 mV/s, 1 M HCl supporting electrolyte) and b) 2 (solid state modified GCE WE, 100 mV/s, 0.5 M NaCl supporting electrolyte) made from the same emulsion before spiking (black) and after spiking (blue). All cyclic voltammograms used a three-electrode set up referenced against a Ag/AgCl electrode with a platinum CrE. . 58

FIGURE 2.13. Absorption spectrum obtain by UV-vis diffuse reflectance using a BaSO4 background and the Kubelka-Munk transformation. The inset shows the calculated band gap based on the Tauc relation.................................. 60

FIGURE 2.14. Lewis basic phosphines such as 4-bis(diphenylphosphino)pyridine (BDPP), tris(dimethylamino)phosphine (TDAP), and tris(thiophenol)phosphine (TTPP). 62

LIST OF SCHEMES

SCHEME 1.1. Fedin’s direct synthesis of $Fe_6S_8(THP)_6Cl_2$ 41

SCHEME 2.1. Stepwise synthesis of compound **2**. The framework depicted is of the a-view with as ball and stick depiction of the clusters and wireframe PTA ligands. Color Scheme: Dark blue, cobalt; yellow, sulfur; orange, phosphorus; teal, copper; purple, iodide; light blue, nitrogen; black, carbon; hydrogens have been omitted for clarity. 53

LIST OF EQUATIONS

EQUATION 1.1. Energy Efficiency. 9

EQUATION 1.2. Voltage Efficiency. 9

EQUATION 1.3. Coulombic Efficiency. 10

EQUATION 1.4. Randal-Sevcik. 28

EQUATION 1.5. Electron Transfer Kinetics. 29

EQUATION 1.6. Nernst Equation. 35

EQUATION 1.7. Asymmetrical H-cell Reaction Quotient. 36

EQUATION 1.8. Reaction Quotient of the Asymmetrical Cell. 37

EQUATION 2.1. Kubelka-Munk Function. 59

EQUATION 2.2. Tuac Relation. 59

EQUATION 2.3. Tuac Relation for UV-vis Diffuse Reflectance. 59

LIST OF ABBREVIATIONS

ARFB	Aqueous Redox Flow Battery
BDC	Benzene Dicarboxylate
BDPP	4-bis(diphenylphosphino)pyridine
Bz	Benzyl
CAP	1,4,7-triaza-9-phosphatricyclo[5.3.2.1]tridecane
CCD	Cyclic Charge Discharge
CE	Coulombic Efficiency
CF	Carbon Felt
CFE	Carbon Felt Electrode
CrE	Counter Electrode
CV	Cyclic Voltammetry
DAPTA	3,7-diacetyl-1,3,7-triaza-5-phosphabicyclo[3.3.1]nonane
dcbdt	1,4-dicarboxybenzene-2,3-dithiolate
DCM	Dichloromethane
DI	Deionized
DMAPP	Dimethallyl diphosphate
DMF	Dimethylforamide
E_a	Anodic Potential
E^o_{cell}	Standard Cell Potential
E_{cell}	Cell Potential
EE	Energy efficiency
E_g	Optical Band Gap

E_{oc}	Open Circuit Potential
EPR	Electron Paramagnetic Resonance
GCE	Glassy Carbon Electrode
iPr	Isopropyl
L	Ligand
MCC	Metal Chalcogenide Cluster
MeCN	Acetonitrile
MeOH	Methanol
MOF	Metal Organic Framework
MSC	Metal Sulfide Cluster
MV	Methyl Viologen
MW	Megawatt
NM	Nitromethane
NMR	Nuclear Magnetic Resonance
PC	Propylene Carbonate
PCS	Power Condition System
Phen	Phenanthroline
POM	Polyoxometallate
PSM	Post Synthetic Modification
PTA	1,3,5-triaza-7-phosphaadamantane
PVC	Polyvinyl chloride
pz	Pyrazolate
RE	Reference Electrode

RFB	Redox Flow Battery
SAF	Superatomic Framework
SBU	Secondary Building Unit
SCXRD	Single Crystal X-ray Diffraction
SGE	Solid Graphite Electrode
SOC	State of Charge
TBA	Tetrabutylammonium
t_c	Charge Time
t_d	Discharge Time
TDAP	Tris(dimethylamino)phosphine
TEA	Tetraethyl ammonium
TGA	Thermogravimetric Analysis
THF	Tetrahydrofuran
THP	Tris(hydroxymethyl)phosphine
THPCl	Tetrakis(hydroxymethyl)phosphonium chloride
TPPTS	trisodium salt
TTPP	tris(thiophenol)phosphine
UV	Ultraviolet
V_c	Charging Voltage
V_d	Discharging Voltage
VFB	Vanadium Flow Battery
WE	Working Electrode

CHAPTER 1: A COBALT SULFIDE CLUSTER-BASED CATHOLYTE FOR AQUEOUS REDOX FLOW BATTERIES

1.1 Introduction

1.1.1 Redox Flow Batteries

The concept of a redox flow battery (RFB) has been around for nearly 85 years. P.A. Pissoort applied for a patent detailing a rudimentary RFB in France in 1933.[1] However, the first in-depth study of RFBs was not done until 1970 by NASA.[2] The RFB design has not changed since this study, although the materials used to fabricate such devices have. The general RFB design consists of a typical anode/cathode with the electrochemically active species dissolved in an electrolyte solution that is separated by a porous membrane.[3] The dissolved electrochemically active species herein are referred to as the anolyte and catholyte, respectively. The anolyte and catholyte of a RFB are stored in separate tanks and transported by pumps to the stack, which is also known as the membrane/electrode interface. At this interface, the redox reactions occur at the electrodes surface and charge is balanced by ions diffusing through the membrane (FIGURE 1.1). The solution-based battery allows for flexibility in design because the electrodes do not double as the electrochemically active species.[4] In contrast to solid-state batteries, RFBs decouple energy and power, which eliminates the need for bulky electrodes.[5] This design permits RFBs to be scaled for grid and micro-grid scale energy storage. Thus, the amount of anolyte

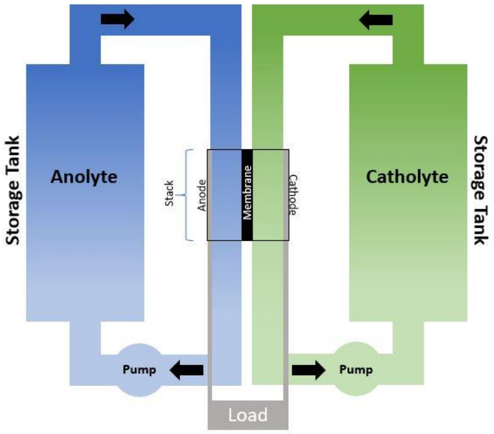

FIGURE 1.1. General scheme of a redox flow battery (RFB).

and catholyte determines the energy capacity while the number of stacks defines the amount of power that can be produced.[4] This is advantageous because large storage devices can easily be engineered, lowering manufacturing cost.

One attractive application for RFBs is to couple them to renewable energy resources in order to stabilize their power output onto the grid. RFBs have a quick response time to potential change as well as a long unit lifetime.[6] Renewable energy resources such as photovoltaic cells and wind farms have weather dependent power output. This is problematic because peak power usage and peak power production is misaligned. For example, peak power usage typically occurs in the evening and night. This poses an obvious issue for photovoltaics Wind power can also be intermittent and may not meet demand on windless days. To harvest peak energy produced during the day, large scale energy storage applications such as hydroelectric pump storage currently aids the grid at night. The hydroelectric method is practical for current energy storage demands; however, it does not offer fast response time.[7]

An energy storage device mediating the power between the grid and resource will need to efficiently deal with these oscillations on demand. Current solid-state batteries are not suited for such applications due to dendrite formation upon extensive cycling. Dendrite formation eventually expands and punctures the membranes of solid-state batteries, leading to imminent device failure.[5] At the 6 MW scale, the Sumitomo vanadium flow battery (VFB) showed quick response to potential change and efficient cycling without significant power loss during the 37-month trial period. The response of this VFB to a 30 MW wind farm was reported over a four-day period (FIGURE 1.2). The VFB used was able to sufficiently supply power to the grid whenever the wind stopped blowing and recharge when the wind picked back up. The black line represents the smoothed power output after being mediated through the VFB.[6] Smooth power output to the grid is crucial because the conversion from direct current to alternating current needs to be controlled so in phase power can steadily be produced.

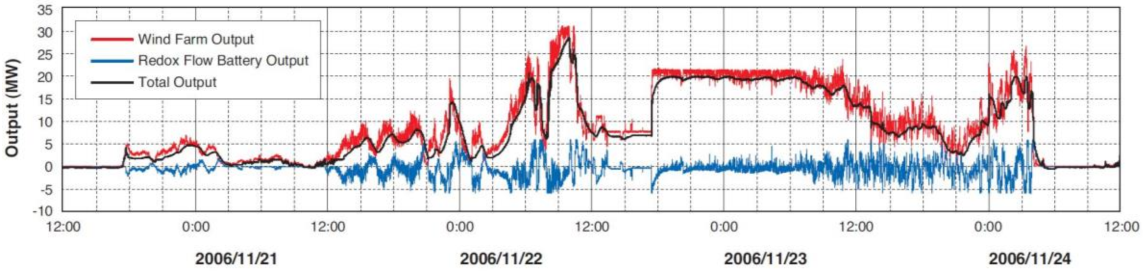

FIGURE 1.2. A plot of power output versus time for a 30 MW wind farm (red), 6 MW vanadium flow battery (blue), and the smoothed overall output (black).[6] (Reprinted with permission from ref 6. Copyright 2013 Sumitomo Electric.)

1.1.2 Fabrication Considerations

The cost of RFB fabrication is defined by three main factors: the electrochemically active species, the membrane, and the solvent.[8] These factors are all interconnected. The solvent is the easiest parameter to address when designing RFBs for large-scale

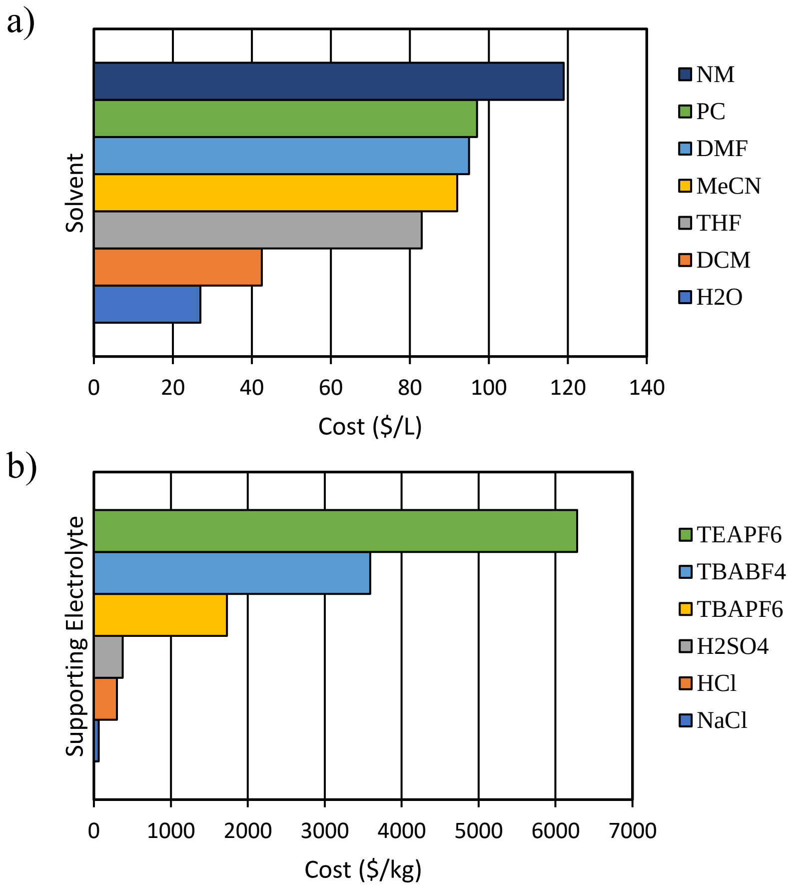

FIGURE 1.3. Cost of a) solvent and b) electrolyte based on market prices of 4L HPLC grade solvents and 98% pure electrolytes from Sigma Aldrich (2019). Solvent List: Nitromethane, (NM); propylene carbonate (PC); N,N-dimethylformamide (DMF); acetonitrile (MeCN); tetrahydrofuran (THF); dichloromethane (DCM); water (H_2O). Electrolyte List: Tetraethylammonium hexafluorophosphate ($TEAPF_6$); tetrabutylammonium tetrafluoroborate ($TBABF_4$); tetrabutylammonium hexafluorophosphate ($TBAPF_6$); sulfuric acid (H_2SO_4); hydrochloric acid (HCl); sodium chloride (NaCl).

implementation. Water is an ideal solvent for grid-scale energy storage because it is inexpensive, nonvolatile, environmentally benign, and readily available. Solvent price drastically increases when moving from aqueous to nonaqueous solutions (FIGURE 1.3a).

Developing efficient redox couples for use in aqueous redox flow batteries (ARFBs) is therefore highly cost effective.[9] Water has a 2.0 V electrochemical window in which electrochemical degradation will not occur.[10] The electrochemical window defines the solvent's stability at a range of voltages outside of which oxidation or reduction occurs. Consequently, maximizing the electrochemical window of an ARFB involves performing redox reactions just within this well-defined potential range. The electrochemical window is also sensitive to the supporting electrolyte. Specifically, acidic conditions cause a cathodic shift of both the reduction and oxidation of the aqueous cell. Basic conditions result in an anodic shift.[10] Aqueous electrolytes that do not affect the pH have the largest electrochemical window to take advantage of (TABLE 1.1). These supporting electrolytes are economical with sodium chloride having the lowest cost (FIGURE 1.3b).

TABLE 1.1. Tabulated values of the electrochemical window at different electrode surfaces under different conditions in aqueous solutions.[10]

Aqueous Electrochemical Window at Different Electrodes[10]			
pH	Carbon (V)	Platinum (V)	Mercury (V)
0	1.6	1.4	1.0
7	2.0	1.8	1.5
14	-	1.5	1.5

The final factor that impacts the electrochemical window is catalytic degradation of the solvent at the electrode's surfaces. A desirable electrode material is one in which electron transfer can occur quickly between the active species with no reaction between the electrode, electrolyte, or solvent itself. Catalytic degradation is dependent on the electrode material used and can be observed through changes in the electrochemical window (TABLE 1.1). This phenomenon arises because the kinetic rate of degradation is determined by the interaction between the electrode's surface and the solvent/electrolyte.[10] Thermodynamics define the potential at which oxidative or reductive degradation begins. These potentials are rarely observed due to overpotentials needed to drive slow kinetic processes. Carbon is an ideal electrode material for ARFBs because it is highly conductive, inexpensive, and has a large electrochemical window in aqueous salt solutions (TABLE 1.1).[10]

A neutral salt water solution will be the most economical and effective combination for ARFBs. One of the largest challenges faced is designing an electrochemically active species to efficiently operate on either side of the battery. The open circuit potential (E_{oc}) of an ARFB is dependent upon the voltage at which the half reactions of the anolyte (E_a) and the catholyte (E_c) occur (FIGURE 1.4). Maximum power output can be obtained by

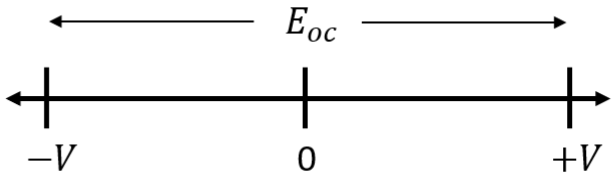

$$C^+ + e^- \rightarrow C^\cdot \qquad E_c = +V$$

$$A^\cdot \rightarrow A^+ + e^- \qquad E_a = -V$$

$$E_c - E_a = E_{oc}$$

FIGURE 1.4. Open circuit potential (E_{oc}) of the ARFB dependence on the half reaction potentials of the anolyte (E_a) and catholyte (E_c).

using anolytes and catholytes with half reaction potentials near the edge of the electrochemical window.[4]

One approach to obtaining maximum power output of the active species is through molecular engineering. Molecular engineering is the modification of known electrochemically active species in order to force half-reaction potentials to shift, solubility to increase, and to prevent degradation of molecules in their various oxidation states.[11] This approach was not used until approximately 2009 when some of the first molecules were designed.[12] Before then, transition metal salts ($AlCl_3$, $ZnCl_2$) and mixed-metal-halogen systems such as Zn/Br_2 and were used to create ARFBs.[2,13] The main advantage of using molecular engineering is the ability to optimize economical species which currently have not been able to reach the DOE's target of 100 \$/kWh.[3] Previous practices were not safe

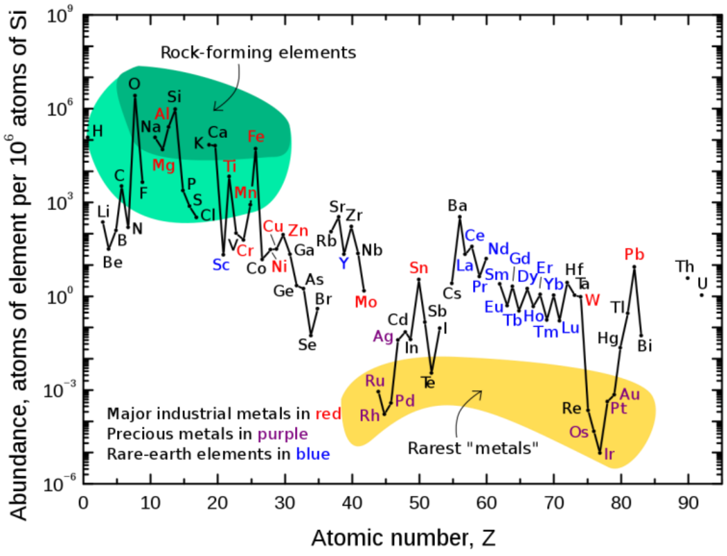

FIGURE 1.5. Elemental abundance on earth sorted by atomic number and normalized against silicon.[14]

for large scale due to highly corrosive and toxic materials. Ideally, redox active battery materials would consist of the rock-forming elements or compounds that can be efficiently manufactured (FIGURE 1.5).

The last major cost in ARFBs is the membrane, which determines battery lifetime, performance, and overall efficiency. The cost analysis of RFBs shows the financial impact of the membrane for two different cases: the power intensive and the energy intensive case (FIGURE 1.6). [8] The power intensive case represents a battery with a smaller energy capacity with the main cost being the membrane. However, as you scale up to a larger sized RFB, the membrane is relatively cheaper than the active species. This is only significant for comparing cost of microgrid and large-scale energy storage.[8] Microgrids play a key role in supporting small communities such as subdivisions, small towns, or large buildings in an urban environment. Here membrane cost has slowed the implementation of these energy storage devices in more urban environments.

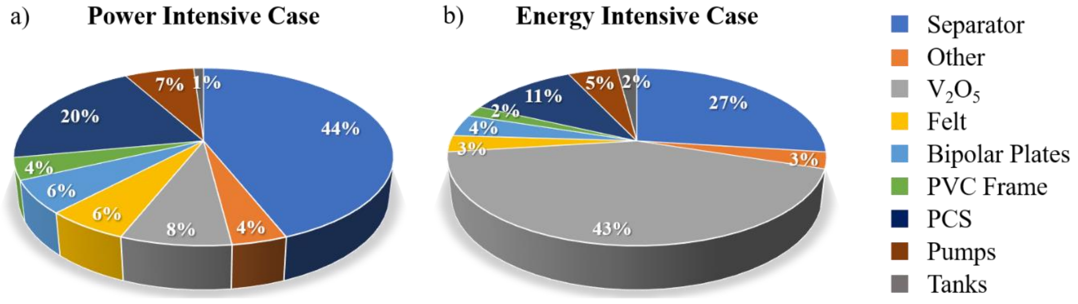

FIGURE 1.6. The cost analysis of a vanadium redox flow battery (VFB) for the a) power intensive case (0.25 MWh) and the b) energy intensive case (4 MWh).[8] (Reprinted with permission from ref 8. Copyright 2012 Elsevier.)

Much work has been done to help cut the cost of the currently popular perfluorinated Nafion™ membrane (approximately \$250-500 m^{-2}).[8] To help drive down cost, anion or cation exchange membranes have recently been employed in laboratory scale ARFBs. This is advantageous for ionic redox couples such as V^{2+}/V^{3+} and V^{4+}/V^{5+}, which are used within VFBs. By coupling a proton exchange membrane to a VFB, no crossover of the vanadium ions is detected. Companies such as Selemion have developed both anion and cation exchange membranes successfully using polystyrene. Membrane price per square meter has drastically fallen and have provided more economical alternatives to perfluorinated Nafion™.

1.1.3 Performance Analysis

A RFB's performance is analyzed by its ability to cycle, the electrochemical stability of the active species, and the efficiency at which the system operates under high load. The energy efficiency (EE) sums up these parameters which is collected experimentally from either static H-cells or fully operational RFBs. The EE can be further broken down and is the product of voltage efficiency (VE) and coulombic efficiency (CE) (EQUATION 1.1).[15–17]

$$EE = CE * VE \tag{1.1}$$

VE is defined as the ratio of the discharging voltage (V_d) to charging voltage (V_c) which is affected by mass transport of electrochemically active species, electron transfer kinetics, and supporting electrolyte diffusion through the membrane (EQUATION 1.2).[10,15–17] Supporting electrolyte diffusion is typically not a hindering factor until charge-discharge rates are faster than the migration of ions through the membrane.[15]

$$VE = \frac{V_d}{V_c} * 100\% \tag{1.2}$$

CE is the ratio of discharge time (t_d) to charge time (t_c), which is defined by the amount of time it takes for charge added to the system to equal the amount of charge extracted. CE is used to track irreversible faradaic loss within the charge-discharge steps and species crossover (EQUATION 1.3).[15–17] CE ratio will always be within unity unless the Faradaic loss happens only during the discharge or charge step.

$$CE = \frac{t_d}{t_c} * 100\% \tag{1.3}$$

There are two different types of cells that can be used to test battery performance: a static H-cell or a full laboratory scale RFB. A symmetric or asymmetric H-cell is much more primitive than a lab scale RFB and does not require pumps, tubing, bipolar plates, or a high surface area membrane/electrode interface.[18] In comparison to a lab scale RFB, an H-cell minimizes the coulombic loss by avoiding leaks through threading and other joints through poor device fabrication. An H-cell can be either asymmetric or symmetric. The asymmetric cell uses both an anolyte and catholyte and is a two-electrode set up (FIGURE 1.7a). A symmetric cell contains only one electrochemically active electrolyte on both sides and only measures what happens at the working electrode (FIGURE 1.7b).[18] The symmetric cell is comparable to the classical 3-electrode frit-based bulk electrolysis. Current membrane technologies have made this set up more advantageous than classical arrangements. Membranes have smaller pores than the zeolite-based frits preventing unwanted side products from crossing over that are generated at the counter electrode. Reactions with these unwanted side products can generate erroneous results about the true stability of the electrolyte of interest.[18] The only drawback to the symmetrical H-cell set up is the requirement of an external reference electrode. Porous glass Vycor frits to separate

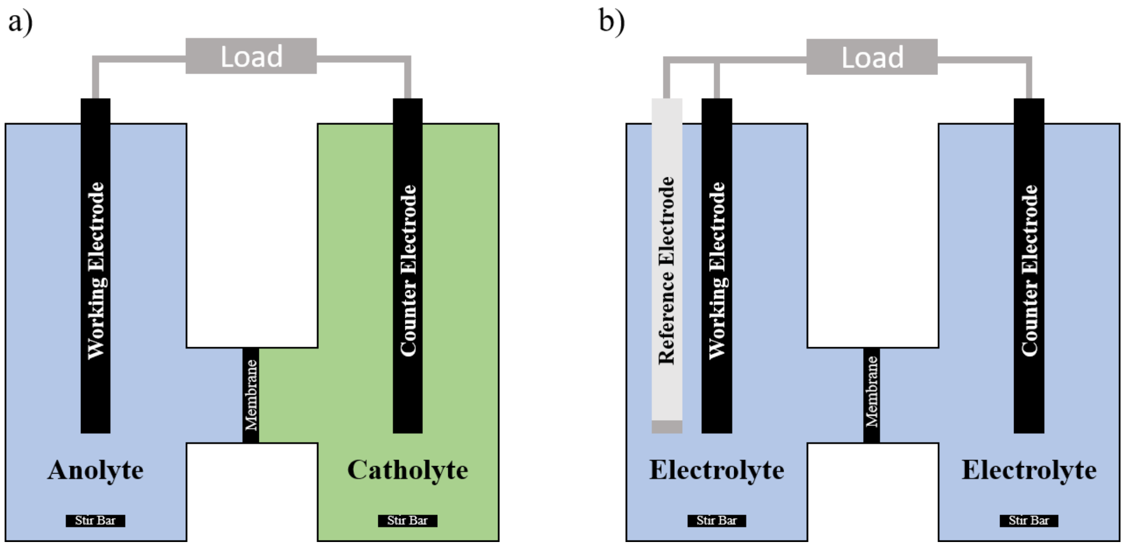

FIGURE 1.7. The cell design of an a) asymmetric H-cell and a b) symmetric H-cell.

the electrolyte and the reference electrode solution in which electrolyte exchange occurs. This is problematic when measuring a cell for long periods of time. The active species can diffuse into the reference electrode causing faradaic loss and is indicated by an increase in capacity fade. Capacity is the absolute measure of coulombs (commonly denoted in ampere-hours) available within the system. This measure shows cumulative faradaic losses over the entire charging/discharging experiment. The capacity fade is typically measured in percent per cycle and is used to predicted lifetimes of RFBs without having to cycle them until no active species remains.[18]

1.1.4 State of the Art

The current commercial technology being applied on a large scale within the energy sector are VFBs. These batteries operate in acidic solutions and generate a potential of 1.4 V per stack.[6] This technology not only has an attractive open circuit potential but also operates with vanadium ions as the anolyte and catholyte (FIGURE 1.8). Net crossover of active material through the membrane is zero if the same material is used on both sides of the battery. The desired oxidation states of any crossed species will be generated during the sequential charge-discharge cycle. A major disadvantage of VFBs is the corrosiveness of the sulfuric acid electrolyte and the cost of vanadium pentoxide. This high cost comes from the increasing demand for vanadium which has a limited supply.[9] The price of organic containing electrochemically active materials has steadily decreased over the years and now stands as a feasible alternative to vanadium.[19]

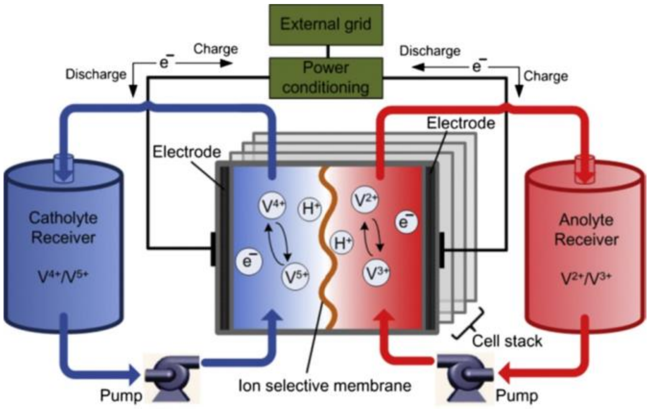

FIGURE 1.8. Graphical depiction of the current commercial VFB.[7] (Reprinted with permission from ref 7. Available under Creative Commons Attribution License (CC BY).).

From a technoeconomic standpoint, inexpensive redox couples are required to realize grid scale ARFBs. Marshak and coworkers have successfully incorporated low cost commercially available organics into ARFBs with an open circuit potential of 1.20 V (FIGURE 1.9).[20] This device used potassium ferricyanide (catholyte) and 2,6-dihydroxyanthraquinone (2,6-DHAQ) (anolyte) with potassium hydroxide supporting electrolyte (pH = 14).[20] This battery demonstrated respectable performance, yet was

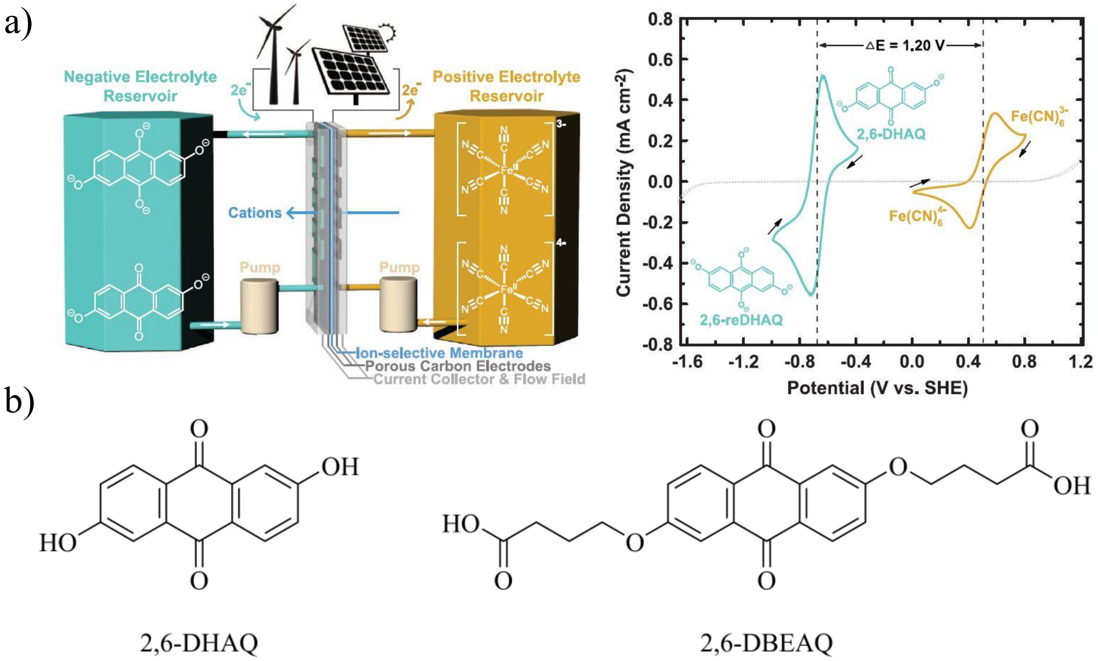

FIGURE 1.9. a) Graphical depiction (left) of commercially available 2,6-DHAQ (blue) anolyte coupled to a ferricyanide (gold) catholyte in a high pH ARFB tested by Marshack and coworkers with the cyclic voltammogram of the active species (right). b) Structure of 2,6-DHAQ used by Marshak and Aziz's derivative 2,6-DBEAQ.[21] (Reprinted (adapted) with permission from ref 21. Copyright 2015 The American Association for the Advancement of Science.)

plagued by the basic decomposition of both ferricyanide and anthraquinone in its reduced state. Aziz *et al*. have addressed this decomposition by synthesizing 4,4'-((9,10-anthraquinone-2,6-diyl)dioxy)dibutyrate (2,6-DBEAQ), causing the capacity fade to reach <0.01% per day over 250 cycles.[21] The other redox couple, ferricyanide, is a well-studied and inexpensive compound, which would be better used in neutral solutions where decomposition would not occur. Ferricyanide is an organometallic compound that has been integrated into an RFB. Organometallic compounds and other inorganic coordination compounds combine the tunability of organics with the electrochemical robustness of inorganic systems.[22]

One of the most well-known organometallics that has been studied to date is ferrocene. Ferrocene is a simple metal complex with a reversible one electron transfer.[23] Hu *et al.* cleverly designed a ferrocene derivative by appending a quaternary ammonium on the end of an aliphatic chain to bring ferrocene into aqueous solutions.[5] This design accomplished both high solubility and an open circuit potential of 1.05 V when coupled with methyl viologen (FIGURE 1.10). This design excelled during cycling under high current loads with a 99% CE, and a VE of 72% at 40 mA cm^{-2}.[5] The diffusion limit of ions crossing the membrane was reached with overpotential having to drive the reactions resulting in decreasing EE as the current density increased.[5,15]

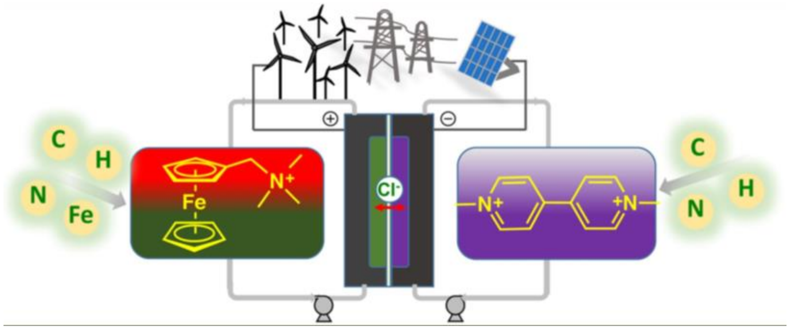

FIGURE 1.10. A graphical depiction of an ARFB using a water-soluble ferrocene derivative as the catholyte (red/green) and methyl viologen as the anolyte (purple) reported by Long and coworkers. [5] (Reprinted (adapted) with permission from ref 5. Copyright 2017 American Chemical Society.)

1.1.5 Metal Sulfide Clusters

The design of a cheap, electrochemically efficient material has been a hot topic within energy research since the start of the molecular engineering age began. Metal sulfide clusters (MSCs) are particularly interesting energy storage materials for several reasons. For example, they can be made from cheap precursors, are electrochemically robust, and can be synthetically modified with ease.[24,25] These clusters can be prepared in a number of different geometries including trigonal bipyramidal, tetrahedral, and octahedral.[26–28] MSCs can also be prepared as oligomers and can even be condensed into larger clusters (FIGURE 1.11).[29,30] MSCs are also found in nature, specifically, the Fe_2S_2 and Fe_4S_4 clusters are found in nature aiding electron transport processes.[31,32]

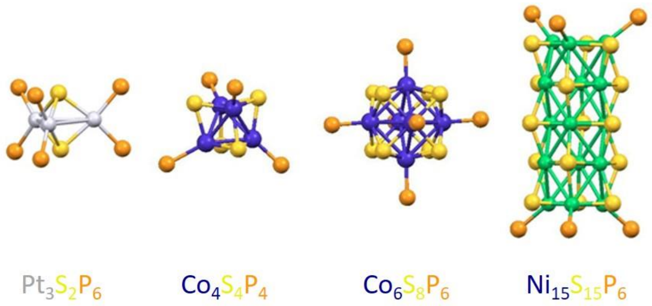

FIGURE 1.11. Common geometries of various MSCs. Geometries depicted are trigonal bipyramidal, tetrahedral, octahedral, and oligomeric, respectively.[26–29]

Iron sulfide clusters are important biologically. These clusters participate in bacterial mitochondrial electron transport, electron shuttling in chloroplast during photosynthesis, and prevent neurodegeneration within the human body.[31,33] Two cubane-like Fe_4S_4 clusters are located within the IspH protein and are held in place by four cysteine ligands (FIGURE 1.12).[34] A unique characteristic of MSC clusters that contributes to their favorable electrochemical profile is the charge delocalization within the metal-sulfide core.[24] This is observed with polarizable sulfur and phosphorus-based ligands. The electron delocalization was proven by Chen, who compared isostructural clusters containing either hard carbonyl ligands or phosphine ligands. Clusters with carbonyl ligands exhibited mixed

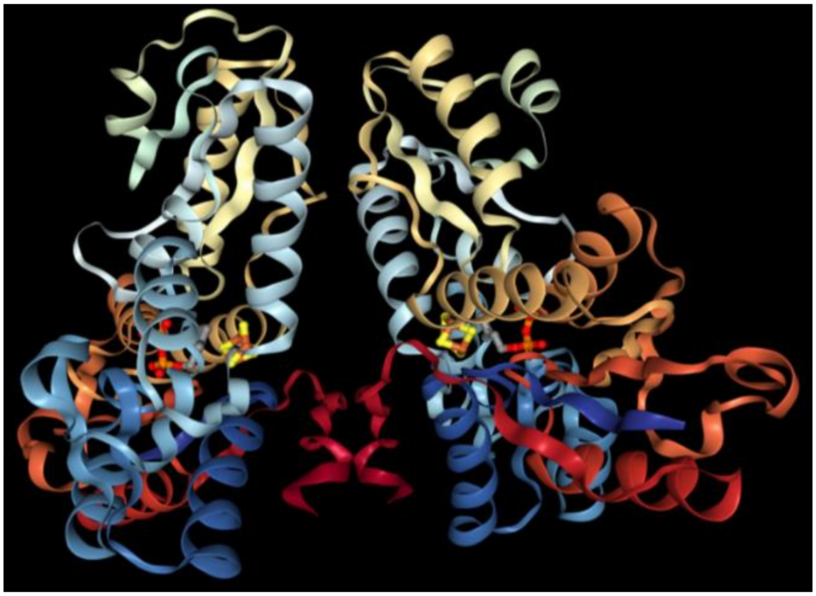

FIGURE 1.12. Single crystal X-ray diffraction (SCXRD) structure of a IspH protein complexed with dimethallyl diphosphate (DMAPP) with the iron (rust red) and sulfur (yellow) seen bound in the middle.[34]

valance character while the phosphine ligand-based clusters were not EPR active until significantly low temperatures were reached.[24]It can be said, without hesitation, that nature is more efficient than even our state-of-the-art for any process. With this said, it would be wise to learn from nature and tailor these natural products to efficiently achieve our goals.

MSCs are typically synthesized using transition metal salts, phosphine ligands, and a sulfur source.[28,30,35,36] Phosphines, PR_3 (R = H, alkyl, aryl), are neutral ligands that coordinate to metals via the lone pair. These ligands determine the solubility and electronic properties of the desired MSC.[9] Donation strength of the phosphine dictates the potential at which the metal core undergoes redox events. The cone angle of the phosphine influences the geometry of the MSC, with the angle being defined as the outside of the Van der Waals radius of the substituents to the metal center which serves as the angle's apex.[27] More sterically hindering substituents would have a larger Van der Waals radius and therefore would have a higher cone angle. Larger cone angles favor smaller MSCs such as the cubane-like tetrahedral cluster because lower coordination numbers minimize steric hinderance between ligands.[27,30] The electronic properties of the MSCs are based on the electron density of the alkyl/aryl appendages to the phosphine coordinated to the core. Electron rich phosphines are better donors causing anodic shifts in the reduction potential. Electron deficient phosphines cause cathodic shifts because of their poor donating ability.[37] Thus, predictions about the MSC’s electronic character can be made by considering the tabulated values of carbonyl stretching frequencies and the phosphine ligand’s cone angle (FIGURE 1.13).[37] Phosphine ligands are a synthetically useful and can be used to tailor MSCs to meet current energy storage needs.

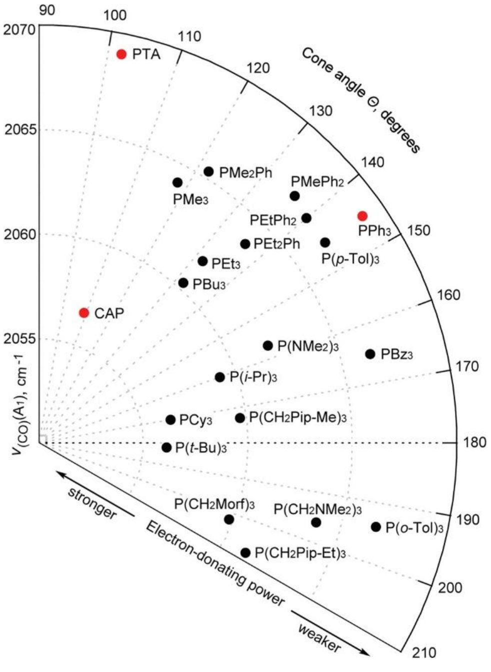

FIGURE 1.13. The cone angle of various phosphines compared to their donation strength, with bulkier phosphines at larger cone angle.[37] (Reprinted with permission from ref 37. Copyright 2015 American Chemical Society.)

1.1.6 Research Objectives

There are numerous MSC clusters to consider as candidates for use as a charge-storage species in an RFB. Octahedral clusters are ideal because of their highly symmetrical core, which gives multiple degenerate orbitals for efficient electron delocalization.[24,38] This allows the core to reversibly pass through multiple oxidation states with very little structural rearrangement.[39,40] Long-term energy storage is therefore achievable given that the ligand's electronics can support the building charge.

A water-soluble octahedral cluster would be an effective active species within an NaCl supported ARFB. Currently, only two water-soluble octahedral clusters are known, both of which have been synthesized by the Fedin research group located in Novosibirsk, Russia. Their approach is to treat water-soluble phosphine ligands such as tris(hydroxymethyl)phosphine (THP) with either $FeCl_2$ or $CoCl_2$, in the presence of H_2S.[41,42] This route affords $M_6S_8(THP)_6$ (M = Fe, Co) clusters. However, neither of this octahedral clusters were structurally characterized due to the hydrophilicity of the THP ligand. Furthermore, these clusters quickly degraded in the presence of oxygen.[41,42]

We hypothesized that the use of a more rigid and less reactive phosphine could provide access to water soluble octahedral MSCs with air stability (FIGURE 1.14).[43] Specifically, a rigid phosphine would allow purification by crystallization and structural determination by SCXRD. Out of the known water-soluble phosphines, 1,3,5-triaza-7-phosphaadamantane (PTA), is of particular interest. PTA mimics the adamantane cage with nitrogens in the 1,3, and 5 positions, and a phosphorus at the remaining tertiary center. This rigid, water-soluble phosphine is unique because it is thermally stable, air/moisture stable,

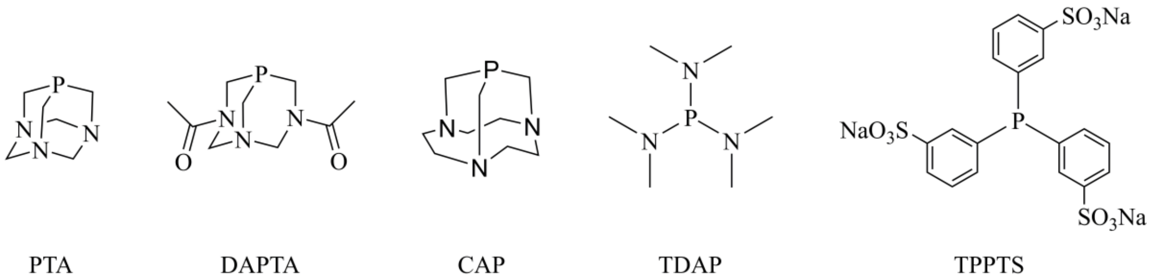

FIGURE 1.14. Common water-soluble phosphines previously synthesized within the literature.[37,44–46] Ligands Depicted: 1,3,5-triaza-7-phosphaadamantane (PTA); 3,7-diacetyl-1,3,7-triaza-5-phosphabicyclo[3.3.1]nonane (DAPTA); 1,4,7-triaza-9-phosphatricyclo[5.3.2.1]tridecane (CAP); tris(dimethylamino)phosphine (TDAP); 3,3’,3”-phosphanetriyltris(benzenesulfonic acid) trisodium salt (TPPTS).

and is commercially available.[47] Other interesting properties include the behavior of the heteroatoms within the aliphatic cage. PTA is a monoprotic base even at a low pH and is protonated or methylated preferably on the nitrogens instead of the phosphorus.[37] Neutral PTA has a reported water solubility of 1.5 M, with an acylated derivative, 3,7-Diacetyl-1,3,7-triaza-5-phosphabicyclo-[3.3.1]nonane (DAPTA), reaching 7.4 M. Therefore, PTA-ligated clusters could potentially be modified via acylation. Direct synthesis of new clusters by simple ligand modification can also be imagined.[45]

Direct synthesis of an hexanuclear octahedral metal sulfide cluster will be attempted using adapted literature.[41,42] This approach would most likely provide the desired metal sulfide octahedral cluster in good yield. Numerous Co_6S_8 clusters[28,36,48,49] are known in multiple oxidation states and only two derivatives of Fe_6S_8 clusters[25,35,40,41] exist. The first synthetic target will be to synthesize a Co_6S_8 cluster stabilized with PTA ligands. Given this, the following objectives will be attempted in order:

1) Synthesize $Co_6S_8(PTA)_6$ using adapted literature preparations.

2) Fabricate an ARFB with sodium chloride as the supporting electrolyte in both a symmetric and asymmetric H-cell.
3) Attempt to modify the $Co_6S_8(PTA)_6$ cluster post-synthetically to increase solubility and stability.
4) Synthesize other water-soluble metal-sulfide clusters using PTA.

1.2 Results and Discussion

1.2.1 Synthesis and Structural Characterization of $Co_6S_8(PTA)_6$•4HCl (**1**)

The $Co_6S_8(PTA)_6$ cluster was formed by bubbling hydrogen sulfide through a hot methanolic solution containing a 1:2 ratio of $CoCl_2$ to PTA at 45^{o}C. This synthetic procedure was adapted from a report by Cecconi *et al*.[48] By filtering and washing the precipitate, the crude cluster was isolated as a dark brown solid. The desired cluster was recrystallized from water/ethanol layering to yield single crystals of **1** as a tetrachloride salt. The structure was confirmed by SCXRD and element analysis with the formula of $Co_6S_8(PTA)_6$•4HCl (**1**).

Single crystals of **1** pack in an orthorhombic *Cmca* space group with well-resolved data giving a R-factor of 5.54% (FIGURE 1.15). The resulting structure of the cluster was highly symmetrical with all angles nearly ideal for the geometries involved. The cluster was tightly packed with the chloride atoms transverse between the layers of metal sulfide cores (FIGURE 1.17a-c). These chlorides surrounding the cluster are within hydrogen bonding distance to the nitrogens (N-Cl = 2.993 Å) suggesting that the nitrogen atoms are protonated, and that the metal sulfide core is not oxidized.

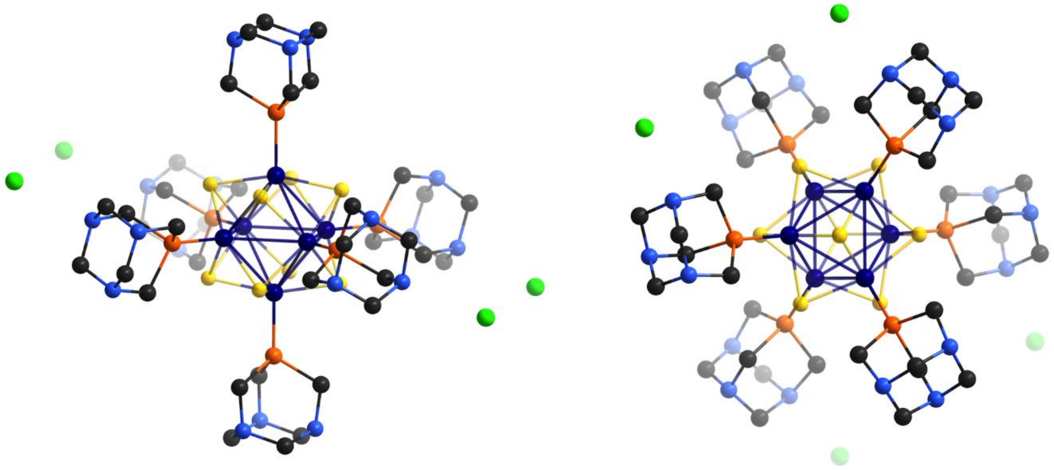

FIGURE 1.15. Ball-and-stick X-ray crystal structure of $Co_6S_8(PTA)_6$•4HCl (1) as viewed from the side and top, respectively.[9] Color Scheme: Carbon, black; chlorine, green; cobalt, dark blue; nitrogen, light blue; phosphorus, orange; sulfur, yellow. (Reproduced from ref 9 with permission from The Royal Society of Chemistry.)

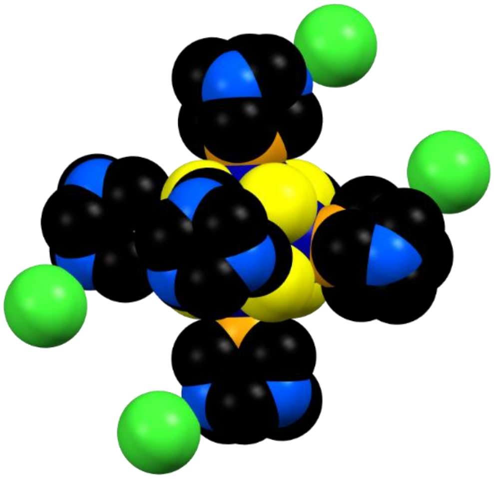

FIGURE 1.16. Crystal structure of **1** shown in a space-filling model with cobalt, dark blue; sulfur, yellow; phosphorus, orange; carbon, black; nitrogen, light blue; chlorine, green with hydrogens omitted for clarity.[9] (Reproduced from ref 9 with permission from The Royal Society of Chemistry.)

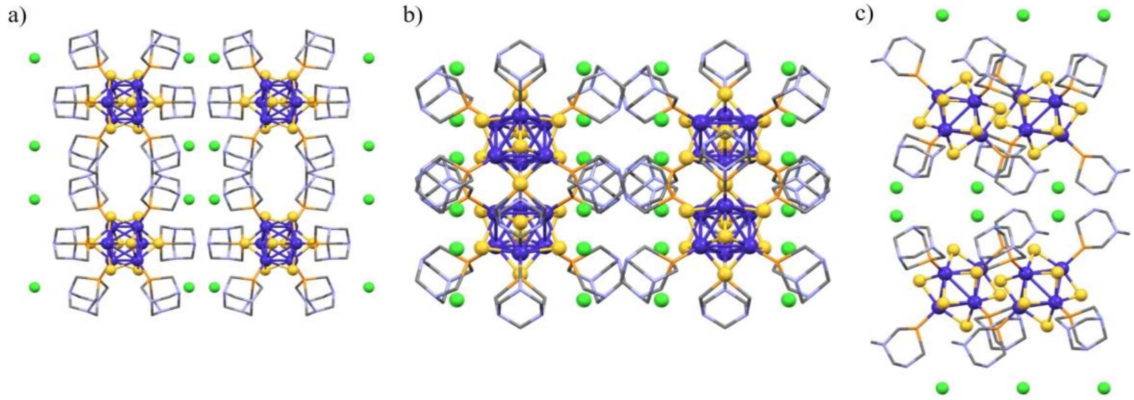

FIGURE 1.17. The packing of the **1** as seen by the a) a-view, b) b-view, and c) c-view.[9] (Reproduced from ref 9 with permission from The Royal Society of Chemistry.)

The Evans NMR method was used to determine that the core of **1** was not oxidized (Appendix G). The theory behind this method states that the signal from a deuterated solvent is different in the presence and absence of a paramagnetic substance.[50] As previously reported, these cluster cores are paramagnetic once oxidized to their monocationic state and are diamagnetic in their neutral and dicationic state.[48] Upon performing the experiment, no shift could be seen in the deuterated solvent signal confirming that the core is in fact neutral (FIGURE 1.18).

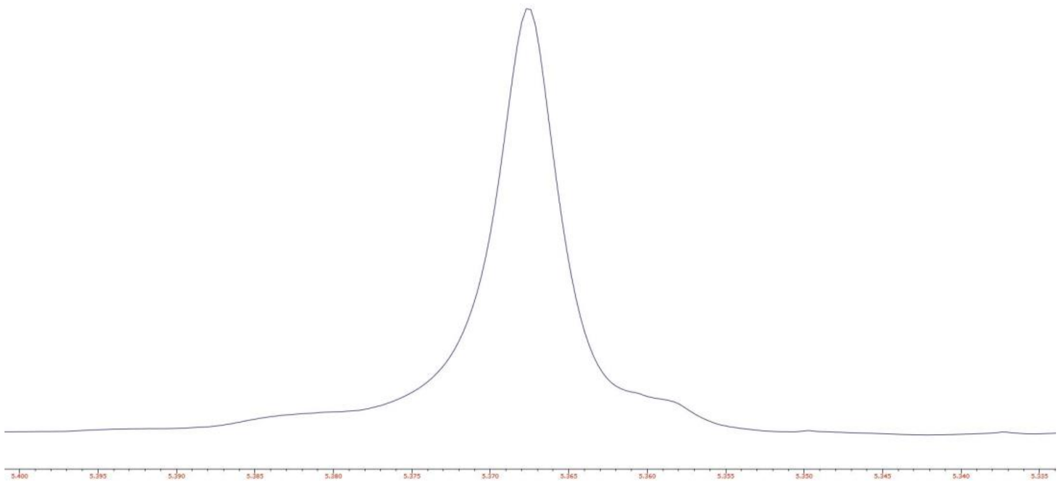

FIGURE 1.18. ^{1}H NMR solvent peak of **1** (35% DCl in D_2O, 300 MHz, 25 ºC) with a capillary of pure DCl solution sealed within the NMR tube.[9] (Reproduced from ref 9 with permission from The Royal Society of Chemistry.)

1.2.2 Solubility

Solubility is a crucial factor for calculating the maximum energy density obtainable in an ARFB. The solubility of **1** was determined through UV-Vis spectroscopy using standard analytical techniques (Appendix C). The cluster exhibited three adsorption peaks at 262, 342, and 400 nm in aqueous solutions, which are characteristic of the Co_6S_8 core. Slight shifts in the UV-Vis spectrum was observed for the absorptions of **1** when dissolved in a hydrochloric acid solution. The absorption peaks in a 0.1 M HCl solution are at 271, 338, and 395 nm, most likely arising from the change in protonation state (FIGURE 1.19). The shifts in absorption wavelength in acid were accompanied by a significant (*ca*. 25 mM) increase in the solubility of **1**. We attribute this enhanced solubility to protonation of the PTA ligands. This is not surprising, as protonated PTA is more soluble than neutral PTA (TABLE 1.3).

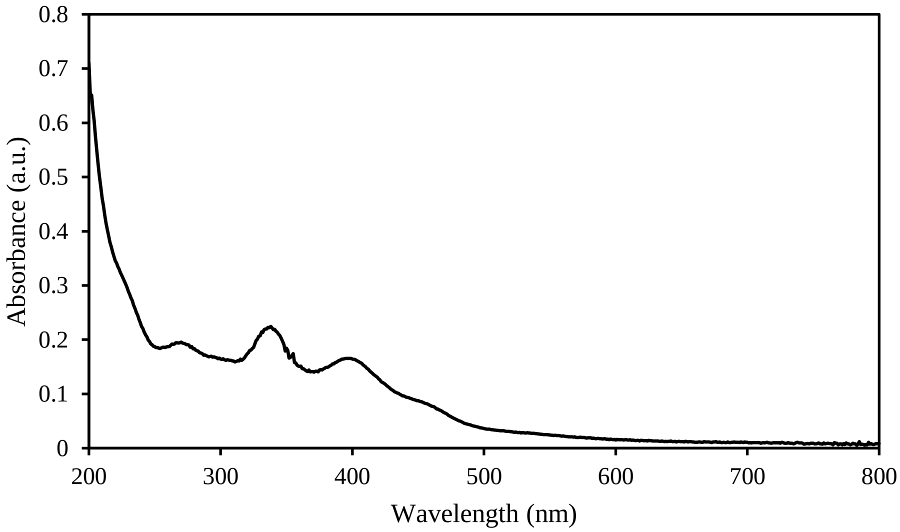

FIGURE 1.19. UV-Vis spectrum of a 7.5 µM solution of $Co_6S_8(PTA)_6$•4HCl in 0.1 M HCl (aq).[9] (Reproduced from ref 9 with permission from The Royal Society of Chemistry.)

TABLE1.2. The calculated solubility and adsorption coefficients from experimentally obtained data in both deionized (DI) water and hydrochloric acid solutions.

DI Water[a]		**0.1 M HCl**[a]	
λ (nm)	ε ($M^{-1}cm^{-1}$)	λ (nm)	ε ($M^{-1}cm^{-1}$)
262	39545	271	26627
342	-	338	30624
400	-	395	22615

[a]Maximum solubility of **1** found to 56.9 mM in DI water, and 85.4 mM in 0.1 M HCl.

The 56.9 mM maximum solubility can be attributed to the cluster's large size, which has a diameter of 1.6 nm measured from the outside of opposing PTA ligands. Unfortunately, the 18 hydrogen bond acceptors on the periphery of the cluster were insufficient to make up for the large size. Another factor that possibly contributes to the low solubility of **1** is the high symmetry of the nanocluster. High symmetry is known to lead to lower solubility. This is not the case for asymmetric molecules.[51]

1.2.3 Electrochemical Characterization by Cyclic Voltammetry

Cyclic voltammetry (CV) was first used to probe the electronic properties of our material in solution. Two reversible oxidations are observed at the half wave potentials

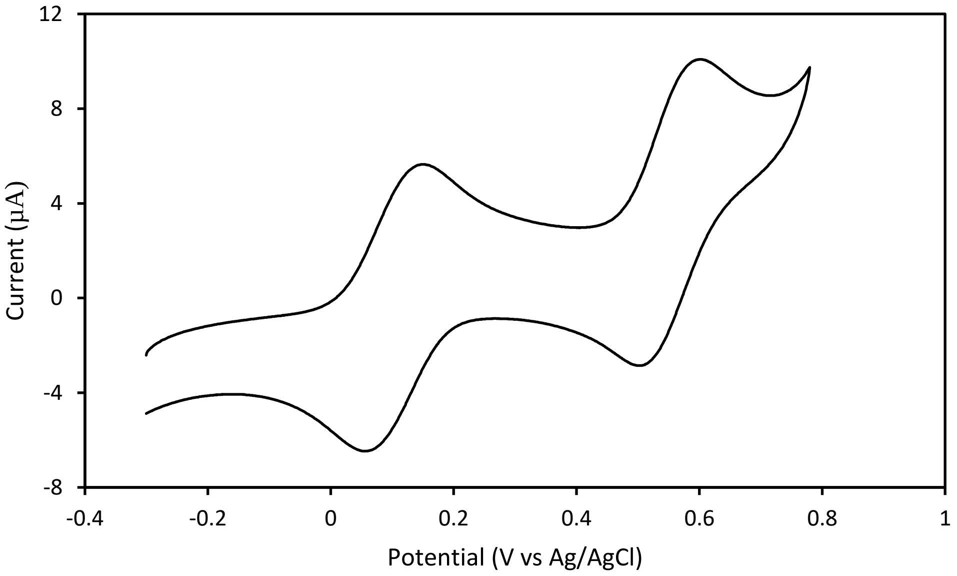

FIGURE 1.20. CV of 1 mM $Co_6S_8(PTA)_6$•4HCl in 0.5 M NaCl referenced against an Ag/AgCl electrode and taken on a GCE WE at 100 mV s^{-1}.[9] (Cyclic voltammetry was performed under at ambient conditions, Electrochemical window: -0.1 to 1.0 V) (Reproduced from ref 9 with permission from The Royal Society of Chemistry.)

($E_{1/2}$) of 90 mV and 540 mV (vs Ag/AgCl) with fast electron transfer at 100 mV s^{-1} (FIGURE 1.20). This however is not seen when the scan rate is lowered to 10 mV s^{-1}. The first oxidation remains fully reversible while the second oxidation becomes irreversible at low scan rates indicating that the dicationic state is only sTABLE on a short time scale.

CV was also used to probe the influence of pH on the oxidation potentials ($E_{1/2}$) (TABLE 1.3). As the acidity increases, the monocation oxidation/reduction remains reversible. The second oxidation, however, becomes irreversible even at faster scan rates. As protonation of the ligand shell increases, the PTA ligands are not electron rich enough to stabilize the building positive charge on the cluster. This ultimately causes the dicationic cluster to irreversibly decompose into an electrochemically inactive species. Increasing acidity also cathodically shifts the $E_{1/2}$ of both oxidations (TABLE 1.3). By the same reasoning, the increasing positive charge on the ligand shell makes the cluster harder to oxidize.

TABLE 1.3. Change in potential of 1 mM **1** in a citric acid and sodium phosphate dibasic buffer at various pH. Cyclic voltammograms were run at 100 mV s^{-1} on a GCE and referenced versus a Ag/AgCl electrode with the report potential for the monocation only.[9] (Reproduced from ref 9 with permission from The Royal Society of Chemistry.)

pH	**$E_{1/2}$ (V)**
7	0
6	0.01
5	0.07
4	0.16
1	0.29

The stability of **1** was tested in both salt water and acidic solutions. This was done by solvating **1** at a known concentration and monitoring the solution by CV over multiple days. Minimal decomposition of **1** was observed for both salt water and acidic solutions (FIGURE 1.21a-b). The acid stability is quite remarkable when comparing **1** to the other

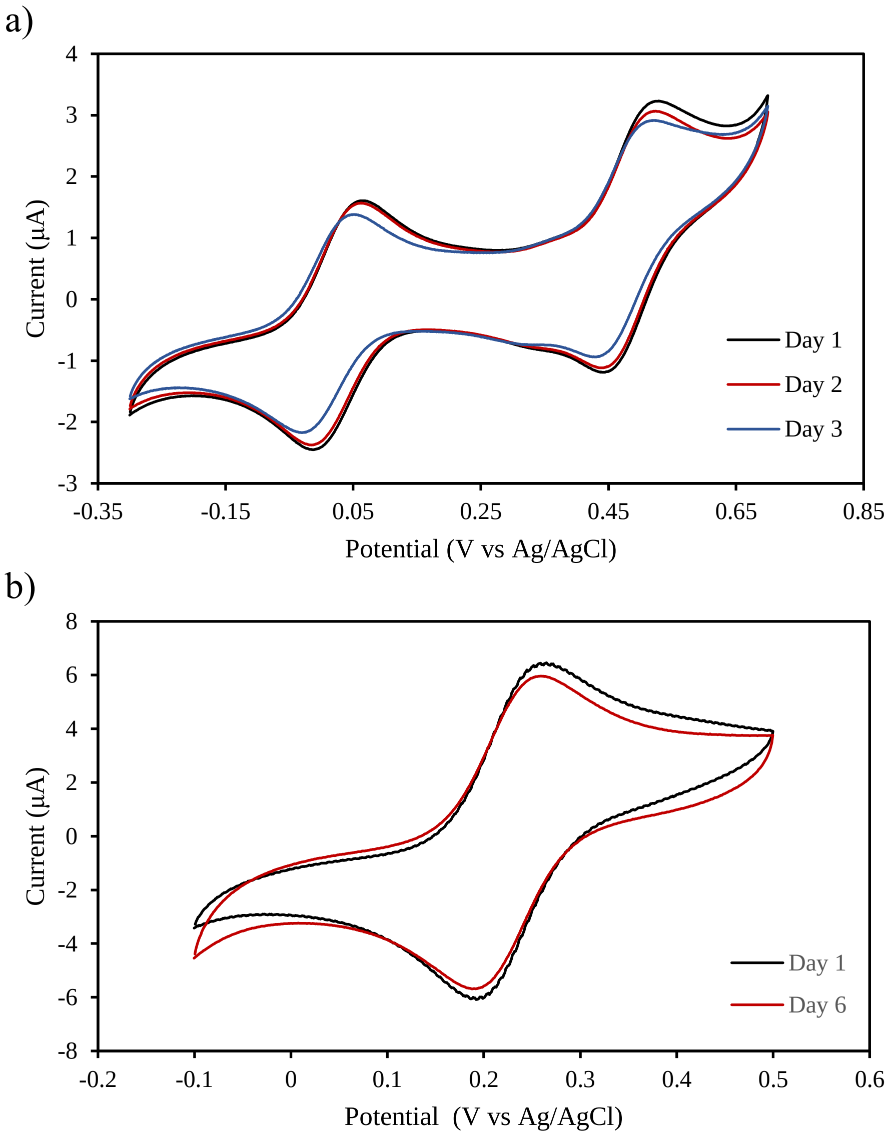

FIGURE 1.21. A 1 mM solution of **1** with a) 0.5 M NaCl or b) 1 M HCl supporting electrolyte referenced against an Ag/AgCl electrode and scanned at 100 mV s^{-1} on a GCE WE.[9] (Cyclic voltammetry was performed under at ambient conditions, Electrochemical window: a) -0.1 to 1.0 V; b) 0 to 1.2 V) (Reproduced from ref 9 with permission from The Royal Society of Chemistry.)

water soluble Co_6S_8 and Fe_6S_8 THP ligated clusters.[41,42] Both clusters reportedly evolve hydrogen sulfide in the presence of acid. Other groups report the ability to methylate the bridging sulfide of the $Mo_6S_8(PEt_3)_6$ cluster core in a non-aqueous system.[52] These results suggest that the bridging sulfides are nucleophilic. The PTA ligand is therefore unique because it shields the core from electrophiles. The 18 Lewis basic nitrogens surrounding the core become positively charged once protonated, electrostatically repealing other cationic species (see space-filling structure FIGURE 1.16).

Cyclic voltammetry was also used to obtain the diffusion and electron transfer rate coefficients in both salt water (0.5 M NaCl) and acidic solutions (1M HCl). Diffusion coefficients were obtained using the Randal-Sevcik EQUATION, which is a valid method for chemically reversible redox couples (EQUATION 1.4, Appendix H).[10] With forward peak current (i_p) linearly dependent on scan rate (υ), the slope of the line would contain the diffusion coefficient (D) and other parameters such as moles of electrons transferred (n), area of the electrode (A), species concentration (C), universal gas constant (R), and temperature (T).

$$i_p = 0.4463nFAC\left(\frac{nF\upsilon D}{RT}\right)^{1/2} \tag{1.4}$$

The electron transfer rate coefficient (k_0) was obtained using the Nicholson method (Appendix H).[53] Information about the reaction at the electrode can be obtained once the kinetics of the transfer become competitive with the scan rate. To simplify the mathematical expression, dimensionless parameters (α, ψ) were used for the derivation and must be properly estimated to give accurate results. For a chemically reversible electron transfer, α can be estimated to be 0.5 which further simplifies the original derivation done by Nicholson in 1965 (EQUATION 1.5). Here, the dimensionless rate

$$\psi = \frac{k^0}{\left(\frac{\pi D F \upsilon}{RT}\right)^{1/2}} \tag{1.5}$$

parameter (ψ) is dependent on the peak separations of the anodic and cathodic waves which increases linearly with scan rate. As long as this holds true, peak separation can then be used to estimate ψ using the data reported in TABLE 1 of Nicholson's paper.[53]

Diffusion coefficients of 6.9 x 10^{-7} and 1.12 x 10^{-6} cm^2 s^{-1} were obtained by CV for the mono- and dication, respectively. These diffusion rates are close to those of similarly sized polyoxovandates but slower than small aqueous organic species like TEMPO or methyl viologen.[19,54] This can be attributed to the size of the cluster limiting the mass transport in solution. The diffusion coefficient for **1** was found to be slower in acid than in neutral aqueous solutions. We assume that this is due to a higher solution viscosity (TABLE 1.4). The electron rate coefficient varied from 2.2 x 10^{-3} in salt water to 7.5 x 10^{-3} cm s^{-1} is hydrochloric acid (TABLE 1.4). The faster electron transfer rate can be attributed higher ion mobility of the electrolyte in solution.[10]

TABLE 1.4. Experimentally determined diffusion and electron transfer coefficient tested in both salt water and acidic solutions.[9] (Reproduced from ref 9 with permission from The Royal Society of Chemistry.)

	0.5 M NaCl		**1 M HCl**	
	Monocation	Dication[a]	Monocation	Dication[a,b]
D	6.9 x 10^{-7}	1.12 x 10^{-6}	5.48 x 10^{-7}	-
k_0	2.2 x 10^{-3}	-	7.5 x 10^{-3}	-

[a] Electrochemical parameter was unobtainable because of nonlinearity of the ΔE_p and υ relationship

[b] Curve is irreversible under the given conditions

1.2.4 Cost Analysis

The synthetic cost of **1** was calculated to compare it against the state-of-the-art VFB electrolytes. Cost per mole of electrolyte will be calculated as a fair measure. The state-of-the-art electrolyte used in VFBs is vanadium pentoxide. Estimations were calculated using the bulk material prices (Alibaba.com) to approximate cost on an industrial scale. This calculation was based on recently reported RFB cost approximations by Friedl and coworkers.[55] This estimation used bulk metric ton quantities to determine the cost of synthetic precursors with intermediates synthesized from industrially available starting materials. The synthetic costs of tetrakis(hydroxymethyl)phosphonium chloride (THPCl), 1,3,5-Triaza-7-phosphaadamantane (PTA), and **1** were individually calculated (TABLE 1.5). Methanol solvent was not included in calculation of the total preparative cost. A quantitative yield for each step was assumed in all calculations.

TABLE 1.5. Preliminary cost analysis for preparation of **1**.[9] (Reproduced from ref 9 with permission from The Royal Society of Chemistry.)

Compound[a]	MW	Equiv	mol	$/g	Amount (g)	$	Intermediate
PH_3	33.99	1	1	0.01	33.99	0.34	THPCl
HCl	36.46	1	1	0.003	36.46	0.11	
Formaldehyde[b]	30.02	4	4	0.0004	120.10	0.13	
NaOH	39.99	1	1	0.0002	39.99	0.008	PTA
Methenamine	140.19	1	1	0.0008	140.19	0.12	
Formaldehyde[b]	30.02	1	1	0.0004	30.02	0.03	
$CoCl_2 \cdot 6H_2O$	273.91	1	1	0.005	273.91	1.37	Cluster (**1**)
H_2S	34.08	1.33	1.33	0.012	45.44	0.54	

[a] All compounds were sourced in bulk from Alibaba.com
[b] Based on a 37% Formalin solution with d = 1.083.

The cost of **1** was found to be higher than the current state-of-the-art VFB, when comparing price per mole. However, cluster **1** is competitive in its ability to operate in neutral solutions. In contrast, VFBs require 1 M H_2SO_4 to effectively solvate the active species. Overall, MSCs can become competitive at the price per mole level upon optimizing the systems solubility and using the inexpensive iron-based congener.

TABLE 1.6. Price comparison of active electrolytes estimated on an industrial scale.[9] (Reproduced from ref 9 with permission from The Royal Society of Chemistry.)

	\$/kg	\$/mol
1	2.78	4.73
V_2O_5	8.00[a]	1.45

[a]Based on optimistic pricing determined by Viswanathan and co-workers.[8]

1.2.5 Symmetrical H-cell Fabrication and Performance Analysis

A symmetrical H-cell was first fabricated in order to isolate the charge-discharge performance of **1** (Appendix I). These cells were tested using cyclic galvanostatic charge discharge (CCD) without exclusion from air, and as previously discussed in Section 1.1.3, operate in a similar manner to bulk electrolysis (FIGURE 1.22). All symmetrical cells were referenced against a Ag/AgCl electrode (RE) with carbon felt (CF) working (WE) and counter electrodes (CrE).

Two different symmetrical H-cells were tested during this phase of research. The first H-cell experiment was used to study first oxidation state only ($Co_6S_8/Co_6S_8^+$ redox couple). The second H-cell study was cycled through both oxidation states in an attempt to confirm the instability of the second oxidation process ($Co_6S_8^+/Co_6S_8^{2+}$ redox couple). The experiments allowed us to conclude that the $Co_6S_8/Co_6S_8^+$ redox couple is a feasible and stable catholyte for ARFBs (FIGURE 1.23a,c-d). This cell was cycled 26 times before the experiment was terminated. Very low capacity loss can be noted with the small decrease being attributed to uptake into the Vycor tip of the RE, which can be visually confirmed (FIGURE 1.22, 1.23c). This will not be a prominent loss mechanism in an asymmetric H-cell as discussed in Section 1.1.3. A pre and post in cell CV of the catholyte was also taken for both oxidation states to investigate stability during cycling. Slight differences can be noted; however, these could arise from changes in the electrodes surface or resistance increases from blocked pores within the membrane/Vycor tip of the RE. The second oxidation was found to be instable by CCD. The onset of the first oxidation occurs at 0 V and the voltage spikes until it reaches the second oxidation. Instead of a slow logarithmic increase, the voltage plateaus until the time cutoff forces the direction of the current to switch. As cycles progress, the time it takes to oxidize **1** to its monocationic state decreases which is indicative that the concentration of **1** is steadily decreasing and the decomposition product is not electrochemically active in the range of potentials swept. Phosphine oxidation is speculated to cause this instability.

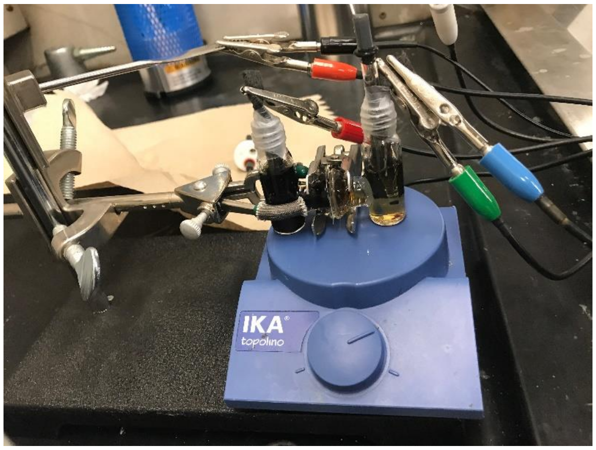

FIGURE 1.22. Symmetrical H-cell set up with the CF WE (blue/green connection), Ag/AgCl RE (white connection), and CF CrE (red connection) connected to a Gamry 1000E potentiostat, separated by a Selemion AMV anion exchange membrane, and sealed with a DuPont Kalrez perfluoroester O-ring.

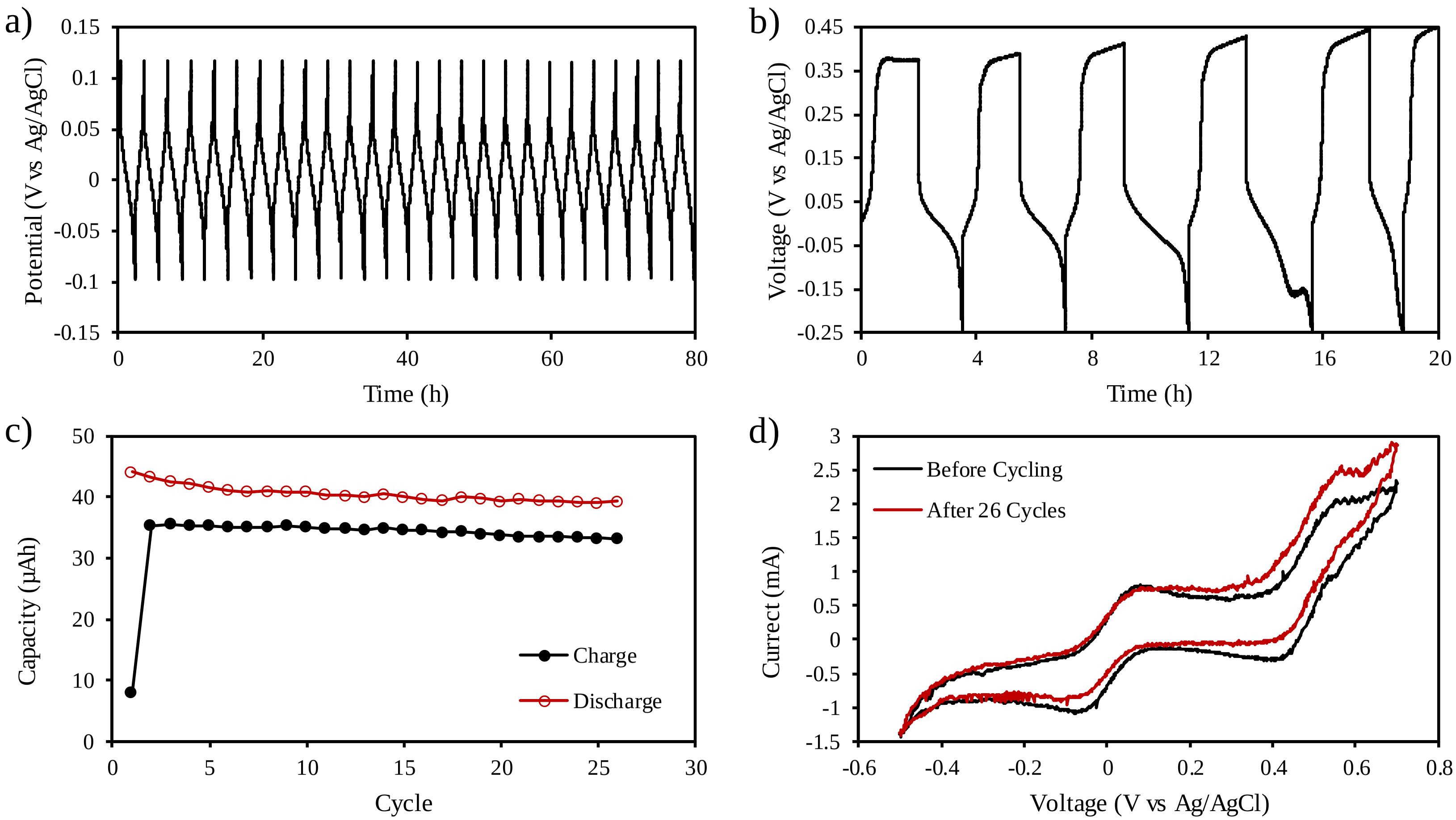

FIGURE 1.23. CCD curves of a) the $Co_6S_8/Co_6S_8^+$ redox couple, b) the $Co_6S_8/Co_6S_8^{2+}$ redox couple, c) the capacity retention for the $Co_6S_8/Co_6S_8^+$ redox couple, and d) the pre and post in cell CV of **1** on CF. All cells were set up with 4 mL of **1** (1 mM, 1 M NaCl, H_2O) per side and measured against a Ag/AgCl RE. [9] (Reproduced from ref 9 with permission from The Royal Society of Chemistry.)

1.2.6 Asymmetrical H-cell Fabrication and Performance Analysis

The asymmetric H-cell experiment was performed next after no catastrophic flaws with the cluster's performance were observed in the symmetric tests (Appendix J). The cell was designed with cluster acting as the catholyte. Methyl viologen (MV^{2+}) was employed as the anolyte and a Selemion AMV anion exchange membrane was used to ensure no electrochemically active species would crossover (FIGURE 1.24). The theoretical cell voltage (E^{o}_{cell}) was 0.75 V based on the reduction potential of MV^{2+} (-0.66 V vs Ag/AgCl) and the reduction potential of $Co_6S_8^{+}$ (0.09 V vs Ag/AgCl). However, the open circuit potential (E_{cell}) stabilized at 0.63 V (FIGURE 25a). Current was only passed into the cells until 80% state of charge (SOC) was reached, giving a predicted cell voltage is 0.67 V.

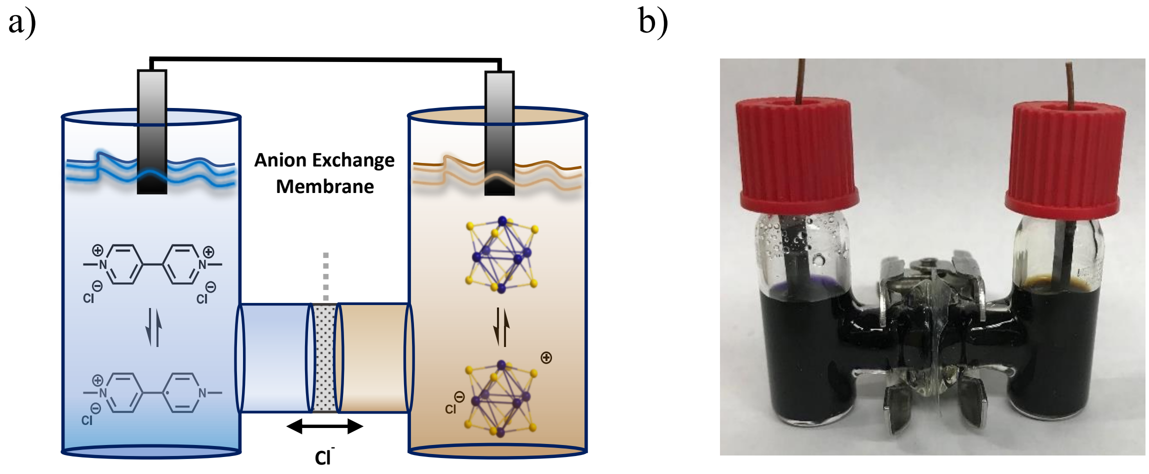

FIGURE 1.24. Asymmetrical H-cell with a) the graphical depiction and b) the actual cell used. The purple solution contains 4 mL of $MV^{\bullet +}$ (2.5 mM, 1 M NaCl, H_2O) and the brown solution contains 4 mL of $Co_6S_8(PTA)_6^{+}$ (2.5 mM, 1 M NaCl, H_2O) under an argon atmosphere, separated by Selemion AMV anion exchange membrane, and sealed by a DuPont Kalrez perfluoroester O-ring, and connected to an external circuit through solid graphite electrodes (SGEs).[9] (Reproduced from ref 9 with permission from The Royal Society of Chemistry.)

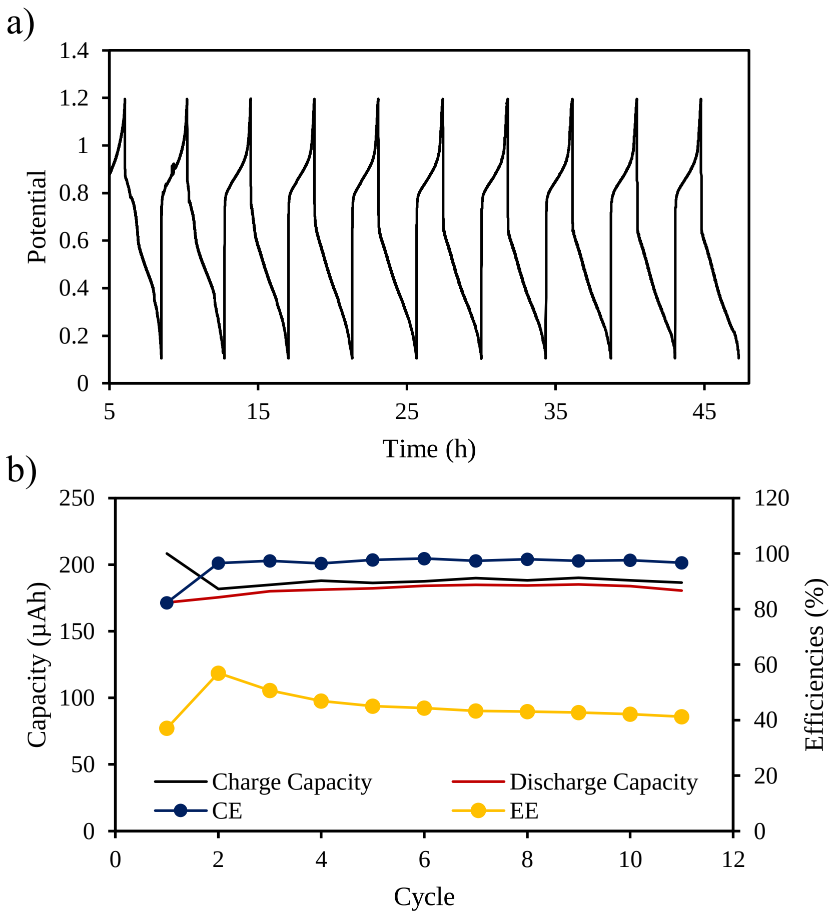

FIGURE 1.25. Asymmetric H-cell performance depicted with a) the CCD curves and b) the CE and EE denoted by dotted lines. The charging and discharging capacities denoted as smooth lines.[9] (Reproduced from ref 9 with permission from The Royal Society of Chemistry.)

This 7.2% voltage drop has been identified and verified through the Nernst Equation. Based on the voltage dependence of the cell on the anolyte and catholyte concentration ratio (Q) in the Nernst Equation one possible cause of this potential drop is the inability to completely dry **1** in ambient conditions (EQUATION 1.6).[10] The reaction of interest is the

$$E_{cell} = E^{o}_{cell} - \frac{RT}{nF} ln(Q) \tag{1.6}$$

spontaneous forward reaction of the charged battery with Q being the quotient of the products and reactants (EQUATION 1.7). While **1** is air stable as

$$MV^{\bullet+} + Co_6S_8^{+} \rightarrow MV^{2+} + Co_6S_8$$

$$Q = \frac{[MV^{2+}][Co_6S_8]}{[MV^{\bullet+}][Co_6S_8^{+}]} \qquad (1.7)$$

the tetrahydrochloride salt, the volatile HCl evaporates upon drying. This causes the electron donating ability to increase until the cluster becomes unstable in air. Thus, accurate weighing of the cluster was difficult to achieve without residual solvent adding to the mass. Under the assumption that the [**1**] is lower than the calculated value based on the mass weighed, the concentration can be predicted using the CCD curves. Knowing the time and amount of current passed from each charging and discharging cycle, the exact number of coulombs were extracted and converted into moles of **1** assuming it was the limiting reagent within the electrochemical reaction (TABLE 1.7). Voltage cutoffs were reached, forcing the current to switch directions during cycling instead of the time cutoffs. This was indicative that the limiting reagent had been fully reduced or oxidized. Continuing with the notion that **1** has been fully oxidized for the charged cell, EQUATION 7 can be rewritten with [**1**] limiting the maximum concentration of products and end concentration of

TABLE 1.7. Experimentally measured concentration of **1** calculated through the capacity.[9] (Reproduced from ref 9 with permission from The Royal Society of Chemistry.)

	Current (µA)	Time (s)	Coulombs (C)	e^- (x 10^{18})	**1** (µmols)	[**1**] (mM)
Charging	107	6220	0.665	4.15	6.89	1.72
Discharging	71	9260	0.657	4.10	6.81	1.70

reactants (EQUATION 1.8). The final calculation for Q can be done using a concentration of 2.5 x 10^{-3} M for MV^{2+} and an averaged measured concentration of 1.71 x 10^{-3} M for **1**.

$$Q = \frac{[MV^{2+}] - [Co_6S_8\ ]}{[Co_6S_8\ ]^2} \tag{1.8}$$

The obtained value for Q is 268, giving a predicted cell voltage from EQUATION 6 to be 0.61 V. This predicted value is within 20 mV of the experimentally obtained E_{cell}, indicating that the assumptions are within reason.

The EE remained above 40% while cycling. This deviation from 100% efficiency was specifically affected by the VE. Equation 2 from Section 1.1.3 defines this as the ratio between the charging voltage (V_c) and the discharging voltage (V_d) with mass transport, ion diffusion, and electron kinetics affecting these parameters. A large voltage drop can be denoted between the end of the charging cycle and beginning of the discharging cycle (FIGURE 1.25a), but this effect is not seen during the symmetrical cell cycling (FIGURE 23a). Out of all the parameters changed, the switch from CFEs to SGEs is likely to cause the drop in VE. CFEs are typically used because of their high surface area and reasonable prices. These CFEs worked well with the symmetrical H-cell because they were not sealed nor extremely air sensitive. The CFEs however failed to work for the asymmetric H-cell because of its requirement for an inert atmosphere. Many attempts were made at employing the CFEs before the SGEs were used. The advantage that the SGEs have over CFEs is that they can make an efficient push contact to a wire which can be fed through the septum seal of the H-cell (FIGURE 1.24b). These SGEs however have much lower surface areas causing overpotentials to assist driving the reaction at the set current densities. By finding an alternative to the SGEs or modifying them through scratching, the VE should rise increasing the overall EE.

1.3 Experimental Details

1.3.1 General Considerations

All reagents were purchased from commercial sources and used as is. The following were used from the commercial suppliers: cobalt(II) chloride (anhydrous) (Alfa Aesar, 99.9%), tetrakis(hydroxymethyl)phosphonium chloride (Aldrich, 80% in solution), formaldehyde (Aldrich, 37% in solution), hexamethylenetetramine (Aldrich, 99.9%), sodium sulfide nonahydrate (Acros Organic, 98%), phosphoric acid (Macron, 85% in solution), sodium chloride (Sigma Aldrich, 99.999%), methyl viologen hydrate (Acros Organics, 98%), sodium hydroxide (Macron, 99%), potassium hydroxide (Macron, Reagent Grade). 1,3,5-Triaza-7-phosphaadamantane (PTA) was synthesized according to a literature method reported by Donald J. Daigle.[44]

Solvents were bought from commercial suppliers and used without further purification. Acetone (Fisher), methanol (Macron) and 190 proof ethanol (Koptec) were degassed via sparging with nitrogen before use. All manipulations were performed under inert atmosphere using standard Schlenk techniques.

Experimental details and instrumentation used is described in Appendices A-J.

1.3.2 Synthesis of **1**

$CoCl_2$ (0.259 g, 2 mmol) was stirred with PTA (0.628 g, 4 mmol) in 35 mL of sparged methanol at 45 ^{o}C. The solution was allowed to stir for 1 h during which the color changed from purple ($CoCl_2$ hydrate), to orange (after PTA addition), to green until a dark purple precipitate formed. Hydrogen sulfide was then generated in a separate flask by dripping 85% H_3PO_4 on to $Na_2S•9H_2O$ at 24 drops per minute. The hydrogen sulfide was allowed to purge through the needle and line connected to the flask before being bubbled into the hot methanol solution. The hydrogen sulfide was bubbled through for 1 h and the dark purple precipitate turned into a fine dark brown suspension. The excess H_2S was trapped in a caustic solution pH ~14 and neutralized with bleach. The reaction mixture was stirred for 5 h and then filtered under inert conditions. The dark brown solid was washed with acetone and the product collected was dissolved in a minimal amount of water and layered 1:3 with 190 proof ethanol inside a scintillation vial. The vial was allowed to sit until the layers fully mixed. This method yielded sharp, dark brown, single X-ray quality crystals (0.327 g, 58%). Note: crystals of **1** appear to be unstable when dried for extended periods of time under high vacuum. ^{1}H NMR (500 MHz, D_2O): δ 2.97 (s, 4 H, NH), 2.84 (m, 18 H, N-C$\mathbf{H_2}$-N), 2.71 (m,18 H, N-C$\mathbf{H_2}$-N), 2.48 (m, 36 H, P-C$\mathbf{H_2}$-N) (Appendices D-F). Elemental analysis for $C_{36}H_{76}Cl_4Co_6N_{18}P_6S_8$, Calculated: C 25.45, H 4.51, N 14.84, S 15.10, Cl 8.35. Found: C 24.94, H 4.49, N 14.15, S 13.38, Cl 8.70. %

1.3.3 Conclusions

Our proof of concept showed exceptional performance for the first ARFB containing an octahedral metal sulfide cluster. This novel cluster was synthesized in one step using inexpensive and abundant starting materials with its only drawback being modest solubility. Very little decomposition occurred between the neutral and first cationic oxidation state, verifying previously reported stability for these materials. Overall, clever design of the ARFB was demonstrated by incorporating an anion exchange membrane into the cell consisting of cationic species exhibiting little to no capacity fade.

1.3.4 Future Work

The solubility limitation can be addressed through use of other water-soluble phosphine ligands. More specifically, the PTA derivative DAPTA can be used. This ligand has a reported water solubility of 7.4 M which is significantly higher than the reported water solubility of PTA (1.5 M).[45] This ligand is also less symmetrical than PTA meaning that the complex formed should have enhanced aqueous solubility (FIGURE 1.26).

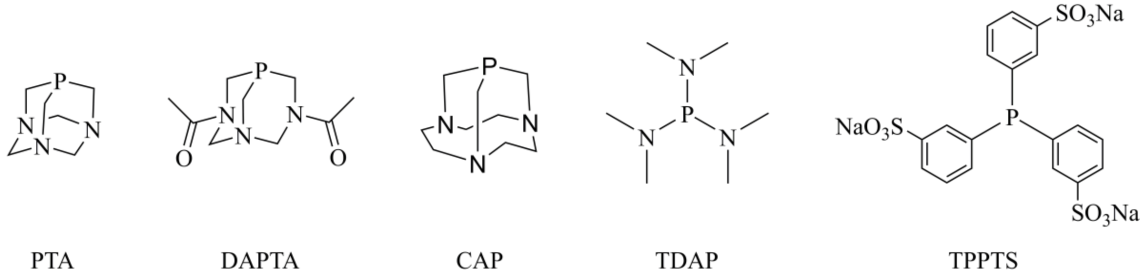

FIGURE 1.26. Common water-soluble phosphines previously synthesized within the literature. Depicted: 1,3,5-triaza-7-phosphaadamantane (PTA); 3,7-diacetyl-1,3,7-triaza-5-phosphabicyclo[3.3.1]nonane (DAPTA); 1,4,7-triaza-9-phosphatricyclo[5.3.2.1]tridecane (CAP); tris(dimethylamino)phosphine (TDAP); 3,3',3"-phosphanetriyltris(benzenesulfonic acid) trisodium salt (TPPTS).

Cyanide ligands are also potential targets. These ligands are small, bind strongly, and have known ligated metal chalcogenide clusters (MCCs) in the literature for non-aqueous systems (FIGURE 1.27).[56–58] By performing a simple salt metathesis, these known MCCs can potentially be used as water soluble electrolytes. Cyanide ligands also have the ability to globally displace the phosphines surrounding the MCC core. This approach could create an anionic Co_6S_8 cluster potentially address modest solubility of $Co_6S_8(PTA)_6$•4HCl . Phosphine displacement has been demonstrated on a Fe_4S_4 cluster with reported moderate yield.[57]

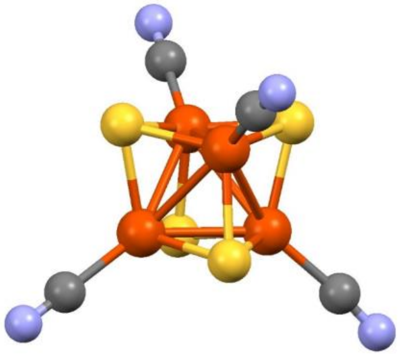

FIGURE 1.27. Crystal structure of $Fe_4S_4(CN)_4^{4-}$.[57] Color Scheme: Iron, red; sulfur, yellow; carbon, black; nitrogen, blue.

A water-soluble iron sulfide octahedral cluster is the ultimate goal. Iron is by far one of the most economical and abundant elements available on a large scale. However, the direct synthesis of Fe_6S_8 clusters is limited. Fedin and coworkers presented a straight forward prep, which seems to be an effective method (SCHEME 1.1). The cluster degrades slowly over time and is air and water sensitive. These issues may be addressed by replacing the THP ligand with PTA using the same synthesis.

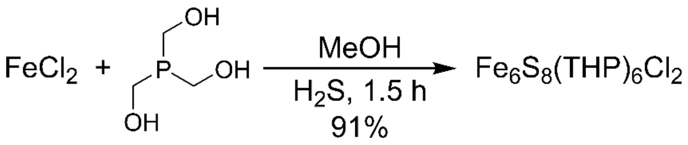

SCHEME 1.1. Fedin's direct synthesis of $Fe_6S_8(THP)_6Cl_2$.[41]

CHAPTER 2: $Co_6S_8(PTA)_6$: A SUPERATOMIC METALLOLIGAND FOR ORDERED TERNARY CLUSTER SOLIDS

2.1 Introduction

2.1.1 Clusters as Building Blocks in Solid-State Materials

Nanoscale materials have spurred interest within the scientific community due to their novel physical properties and tunable nature. Specifically, nanoscale materials display unique attributes not accessible from bulk materials or molecular species, opening a window of opportunity to advance current technologies. Using a hierarchical approach, new nanomaterials can be designed from the “bottom up”.[59] This methodology allows control over the end product and seeks to provide access to crystalline ordered solids. Obtaining atomically precise materials is an important aim of nanomaterial synthesis. Defects within the lattice detract from a materials performance, thus, minimizing their occurrence is crucial.[60,61] One approach to creating highly ordered nanomaterials is by using precise molecular clusters as precursors.[62]

Formation of cluster-based solids has a great deal of interest in the fields of catalysis, energy storage, stabilization of high energy materials, and other industrial applications.[63–65] The current cluster-based materials typically include only one metal cluster and form highly crystalline solids. Frameworks consisting of only one type of metal cluster limits the number of possible functionalities. To expand the construction of multifunctional nanomaterials, multicluster solids may give rise to new synergistic properties.[66] Multicluster solids have remained a challenge to make in comparison to their monocluster predecessors. Due to this challenge, the field has grown slowly however multiple synthetic routes have been demonstrated (FIGURE 2.1).

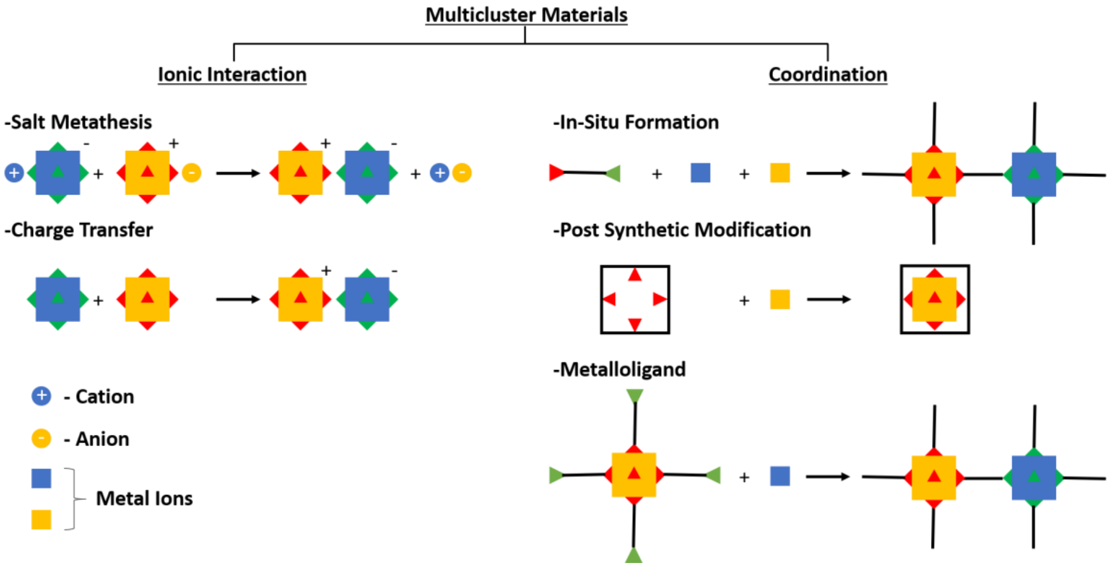

FIGURE 2.1. Synthetic map of various approaches to forming multicluster solids.

2.1.2 Multicluster Ionic Solids: Salt Metathesis and Charge Transfer

Solids built from more than one different cluster can form via salt metathesis or from charge-transfer reactions between two clusters (FIGURE 2.2). The resulting superatomic lattices are thus held together through electrostatic attractions. With these reactions being spontaneous, slow nucleation is attained by diffusion-based mixing of the species of interest. Ionic intercluster salts can exhibit a wide range of different properties depending on the constituent building blocks. Pyroelectricity, ferromagnetic ordering, ohmic conductivity, and phase transitions all have been observed in this class of solid-state materials.[62,67–69] It has been shown that certain superatomic salts pack differently based on which chalcogenide or halide bridging ligand is used within the cluster. This precision also varies with the number of bridging ligand pockets that exist which also influences the packing of these superatomic lattices. Work done by Shott and coworkers has sought to identify the forces directing the assembly of these superatomic lattices.[70]

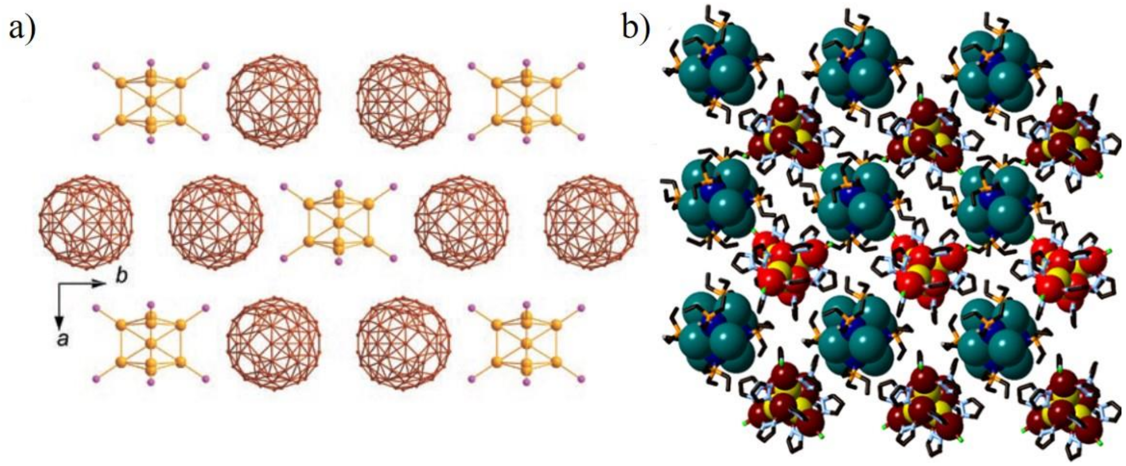

FIGURE 2.2. Cluster salt crystal structures of a) $[Au_8(PPh_3)_8][C_{60}]_2$ formed by salt metathesis[71] (Reprinted with permission from ref 71. Copyright 2008 John Wiley & Sons.) and b) $[Co_6Te_8(PEt_3)_6][Fe_8O_4pz_{12}Cl_4]$ formed through charge transfer.[68] (Reprinted (adapted) with permission from ref 68. Copyright 2014 American Chemical Society.)

2.1.3 Multicluster Coordination: In-Situ Formation

A more popular approach to creating multicluster solids is through *in situ* formation of metal cluster secondary building units (SBUs) around a ditopic ligand. One-pot synthesis is the simplest of the coordination-based approaches and can be achieved through solvothermal reactions, or solvent evaporation. This route relies on the metal ions used to have a different affinity for each end of a ditopic linker. Many cases involve oxophilic and nitrophilic metal ions in the presence of a linker containing a carboxylate, and a heterocycle containing a nitrogen.[72] Other *in situ* routes not involving metal oxides use metal

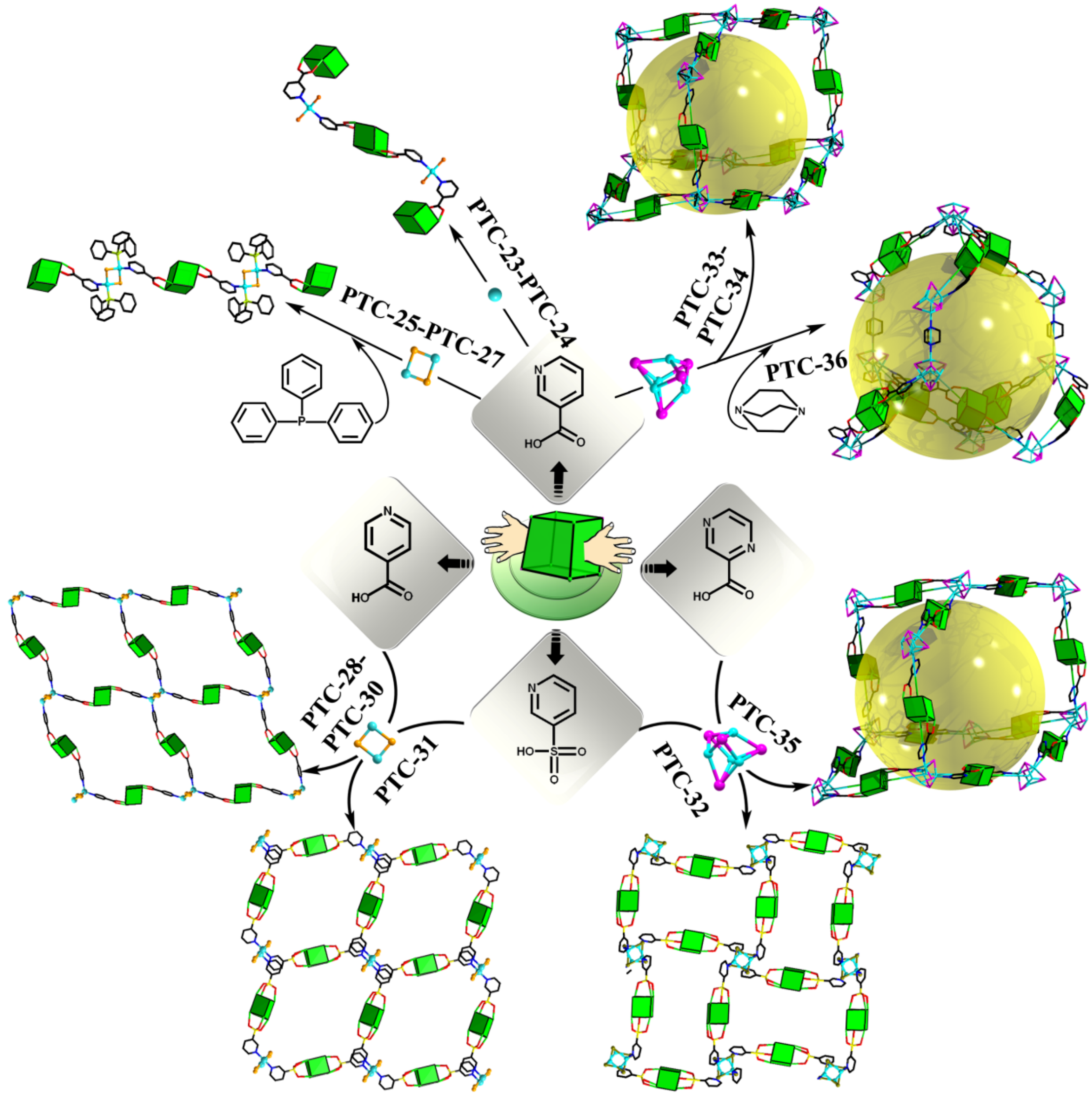

FIGURE 2.3. Structures of in-situ formation of $Ti_6O_4(O\textit{i}Pr)_{10}(O_3P\text{-}Phen)_2(L)_2\ Cu_yX_y$ (L = isonicotinic acid, nicotinic acid, pyridine-3-sulfonic acid, 2-pyrazine-carboxylic acid, or 1,4-diazabicyclo[2.2.2]octane; y = 2, 4; X = Cl, I) coordination polymers.[72] Color Scheme: $(Ti_6O_4(O\textit{i}Pr)_{10}(O_3P\text{-}Phen)_2$, green box; light blue, copper; pink, iodide; gold, iodide or chloride; red, oxygen; yellow, phosphorus or sulfur; black, carbon; dark blue, nitrogen. (Reprinted (adapted) with permission from ref 72. Copyright 2017 American Chemical Society.)

chalcogenide formation as an alternative.[66] However, there are fewer examples of this approach due to a lack or reliable procedures to obtain ordered metal chalcogenide SBUs.

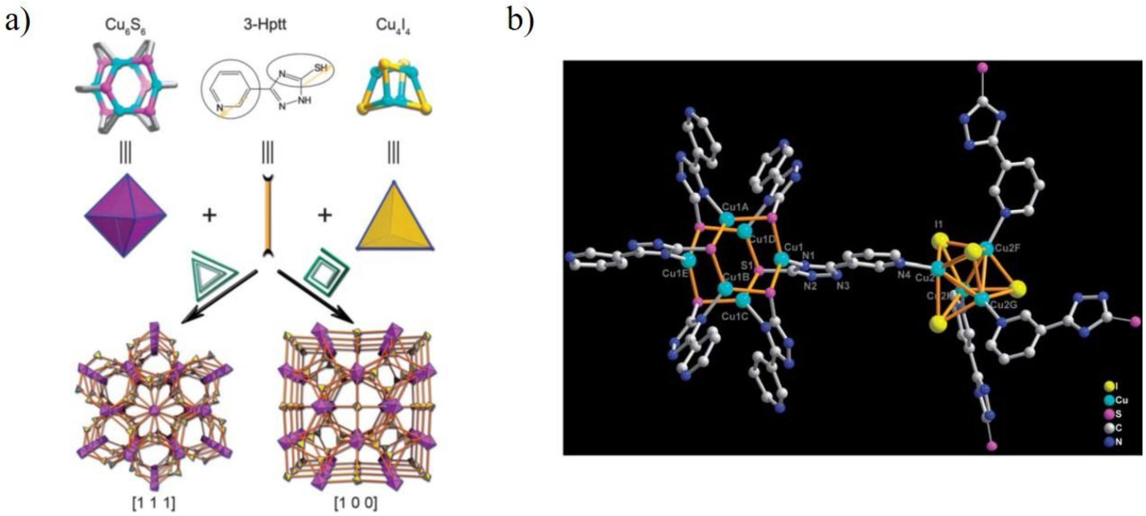

FIGURE 2.4. Formation of the a) Cu_6S_6 and Cu_4I_4 cluster framework using a thiol containing diatopic linker and b) the crystal structure obtained from SCXRD. Color Scheme: Light blue, copper; yellow, iodide; purple, sulfur; gray, carbon; dark blue, nitrogen; and hydrogens have been omitted for clarity.[66] (Reproduced from ref 66 with permission from The Royal Society of Chemistry.)

Copper(I) iodide is a popular transition metal source when forming cluster-based frameworks from nitrogen-based linkers. There are several known polytopic copper iodide SBUs. In fact, Cu_4I_4 SBUs are photoluminescent.[73,74] This photoluminescence arises from copper-copper interactions within the cubane-like Cu_4I_4.[75]

2.1.4 Multicluster Formation: Post Synthetic Modification

Forming known frameworks and modifying the ligands to create insertion points for clusters is advantageous because of the rich amount of literature there is on monocluster frameworks.[76–78] These known monocluster frameworks are easily modified, including some of the first high crystalline metal organic frameworks (MOFs) such as UiO-66 (FIGURE 2.5).[79,80]

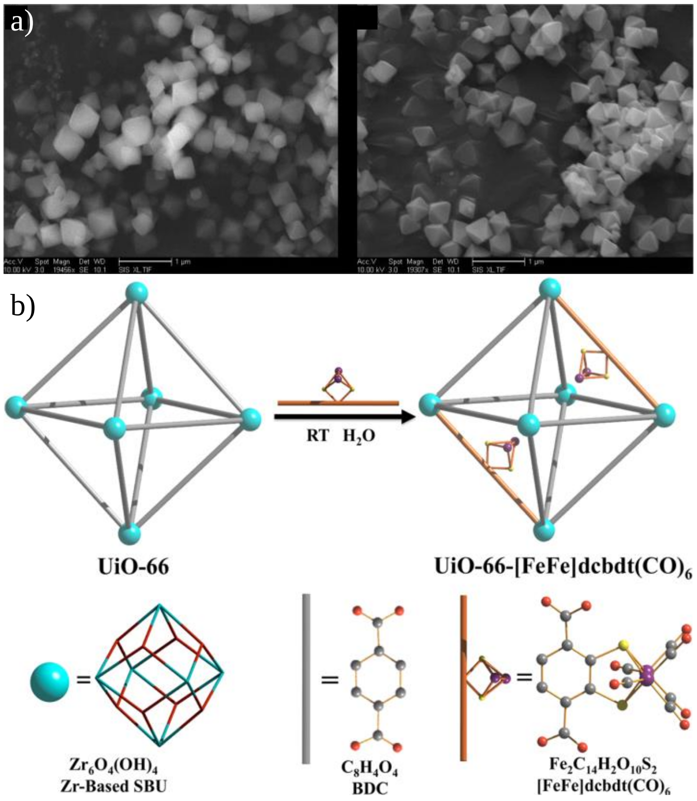

FIGURE 2.5. The a) SEM of UiO-66 with the unmodified linker (left) and modified linker (right) with b) the molecular depiction.[80] (Reprinted with permission from ref 80. Copyright 2013 American Chemical Society https://pubs.acs.org/doi/10.1021/ja407176p)

The post synthetic modification (PSM) technique is advantageous over direct synthetic approaches for the formation of multicluster materials. Specifically, many clusters cannot form or survive the reaction conditions of framework synthesis. PSM is a much milder technique, which allows for the use of reactive species. This has been employed for catalytic clusters like the iron carbonyl cluster, which can be used as a hydrogen evolution catalyst but decomposes readily above 50 ºC.[80] Other PSM routes include adding in molecular "hooks" that can extend out into the pores instead of being tightly bound to the linker.[81] Pore size can be tuned through targeted coordination at these sites to trap certain guests. This has been shown to be a viable strategy for pore-size modulation and can be used to enhance the separation of smaller species (FIGURE 2.6).

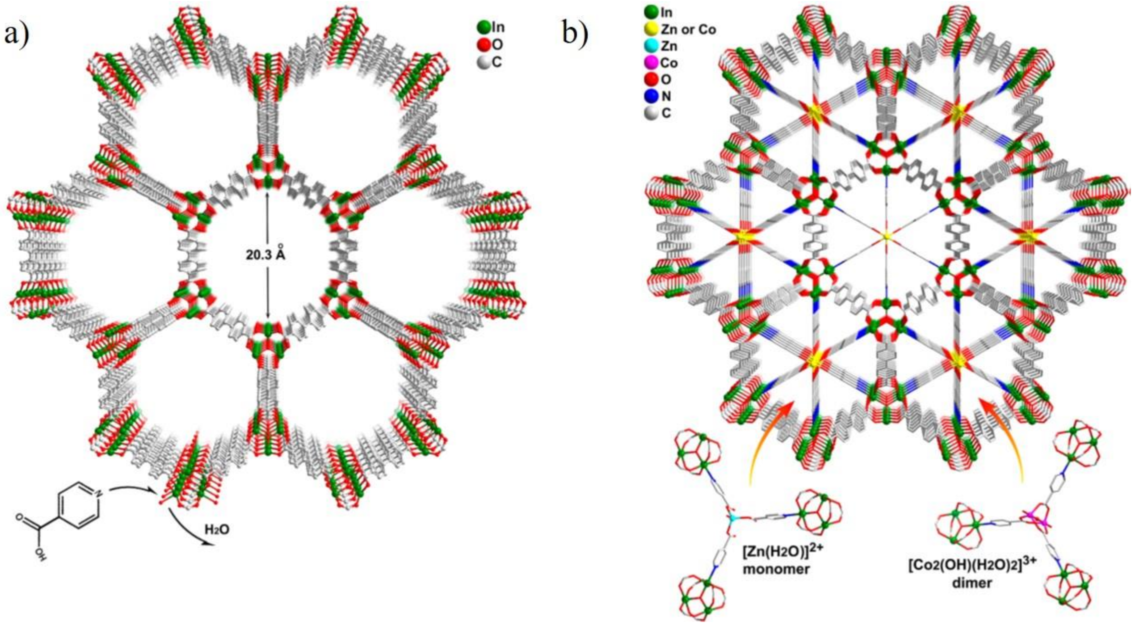

FIGURE 2.6. An indium oxide cluster with an a) open metal site and b) complexes formed using the post synthetically installed hook.[81] (Reprinted (adapted) with permission from ref 81. Copyright 2013 American Chemical Society.)

2.1.5 Multicluster Formation: Metalloligand Linker

According to Srivastada and Gupta, a metalloligand can be defined as a metal complex capable of making further bonds.[82] Metalloligands have been been used to make both, homometallic and heterometallic coordination polymers.[83–85] For example, one of the most well-known homometallic coordination polymers formed via the metalloligand

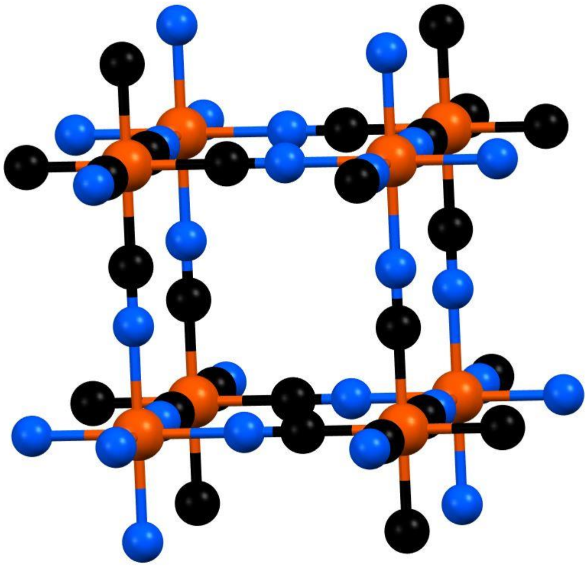

FIGURE 2.7. The crystal structure of Prussian Blue consisting of iron cations coordinated to the nitrogens of the ferrocyanide anion.[86] Color Scheme: Blue, nitrogen; carbon, black; red-orange, iron.

approach is the dye Prussian Blue (FIGURE 2.7).[86] This approach, however, has rarely been used to form multicluster coordination polymers. Metalloligands are advantageous because they can control the topology of their corresponding solids.[82] Recently, a few examples of polyoxometalates[87,88] (POMs) and metal oxide clusters been reported as preformed metalloligands for the stepwise assembly of multicluster materials (FIGURE 2.8).[74,89] Uniquely, POMs represent one class of "superatom" that has been used for framework synthesis. These large cluster-based solids can be referred to as superatomic frameworks (SAFs), which are an emerging class of solid-state materials constructed from nanometer sized superatoms. Apart from POMs, the only other class of superatom that has been incorporated into a coordination-based, multicluster framework, are metal chalcogenide clusters (MCCs). Currently, only one MCC has been reported in a SAF

(FIGURE 2.9).[90] This MCC specifically is the $Co_6Se_8(PEt_2BzCOOH)_6$ cluster which is analogous to the previously described $Co_6S_8(PTA)_6$. The MCC based SAF depicted shows three reversible oxidation processes within the framework itself and is made possible by the minimized structural rearrangement discussed in Section 1.1.5 for MSCs. For redox active materials incorporated into a solid, minimal molecular rearrangement is crucial to maintain the structural integrity of the solid. Any distortions or excess strain can promote degradation to a lower energy state which would be undesirable if these materials were implemented in energy storage devices.

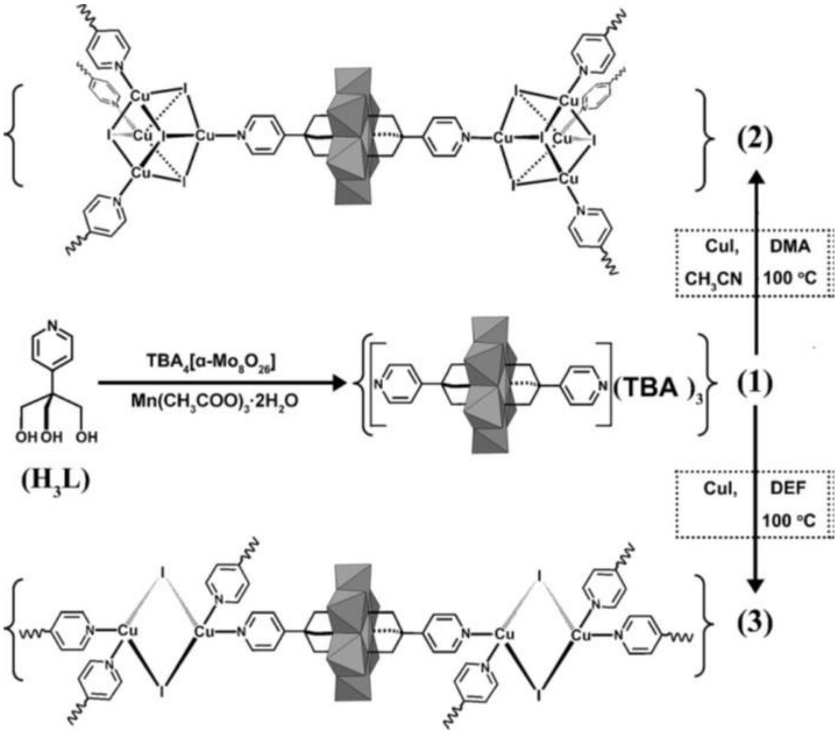

FIGURE 2.8. Linear POM synthesized in (1) using copper(I) iodide SBUs to create ordered polymeric framework (2) or (3).[89] (Reprinted with permission from ref 89. Copyright 2016 John Wiley & Sons.)

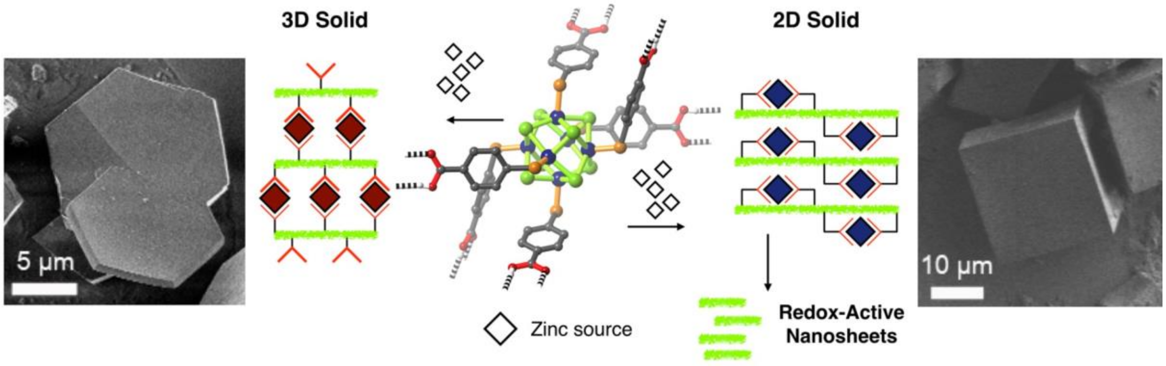

FIGURE 2.9. A 2D and 3D accessible redox active SAF based around the redox active $Co_6Se_8(PEt_2BzCOOH)_6$ superatom monomer with zinc oxide SBUs.[90] Color Scheme: Green, selenium; blue, cobalt; orange, phosphine; grey, carbon; red, oxygen; and hydrogens were omitted for clarity. (Reprinted with permission from ref 90. Copyright 2017 American Chemical Society https://pubs.acs.org/doi/10.1021/acscentsci.7b00328)

2.1.6 Research Goals

Previously described $Co_6S_8(PTA)_6$•4HCl is a possible candidate for incorporation into a SAF. This inspiration comes from the successful formation of the analogous Co_6Se_8 framework in which the phosphine ligated cluster withstood the reaction conditions of solvothermal synthesis. The $Co_6S_8(PTA)_6$•4HCl cluster has 18 Lewis basic nitrogen atoms surrounding the periphery opening the opportunity to use this ligand as a superatomic metalloligand for a coordination-based network. Preferably, the nitrophilic copper(I) iodide will be used to form cluster SBUs giving rise to a multifunctional, multicluster crystalline solid. The following research objectives will be attempted in the following order:

1) Explore the use of $Co_6S_8(PTA)_6$•4HCl as a metalloligand in forming multicluster materials with copper iodide based SBUs.
2) Characterize new solids and identify key optical, electrical, and physical properties that can be used to make a functioning device.

2.2 Results and Discussion

2.2.1 Synthesis and Structural Characterization of $2[Co_6S_8(PTA)_6H^+]$•$2[Cu_4I_4]$•$[Cu_4I_6^{2-}]$(**2**)

Heating a 1:2 mixture $Co_6S_8(PTA)_6$•4HCl and CuI in a solution of acetonitrile/water under solvothermal conditions, at 60 °C for 48 hours, leads to the formation of dark black crystals of **2**. Powder X-ray diffraction (PXRD, Appendix M) and scanning electron microscopy (SEM, Appendix N) were used to determine the purity of **2**. The experimental and predicted PXRD patterns correspond well with each other for both **2** and its metalloligand precursor. Micrographs from SEM depict that the bulk sample was crystalline, homogenous, and monodispersed. Single-crystal X-ray diffraction (SCXRD) reveals that compound **2** crystallizes in the monoclinic space group $P2_1/c$ and comprises three distinct polynuclear cluster subunits. Remarkably, the $Co_6S_8(PTA)_6$ metalloligand remains intact and is surrounded by four Cu_4I_4 clusters and one $Cu_4I_6^{2-}$ cluster (SCHEME 2.1). This crystalline solid is nonporous, which we can attribute to the large amount of copper iodide clusters coordinated around the central $Co_6S_8(PTA)_6$ superatom. There are five copper iodide clusters coordinated to five of the six PTA ligands present. The sixth PTA is uncoordinated and occupies void space. This sixth ligand is most likely uncoordinated due to steric constraint. The three clusters present include the monoprotonated $Co_6S_8(PTA)_6$•H^+ metalloligand, and two copper(I) iodide SBUs. The superatomic metalloligand remained intact during the solvothermal synthesis with only HCl exchanged on the periphery. When compared to the $Co_6S_8(PTA)_6$•4HCl starting material, which is highly symmetrical, the cluster incorporated into the framework has minor structural distortions (FIGURE 2.10d). Angles between the phosphorus were measured through a centroid calculated into the middle of the cobalt square bipyramidal

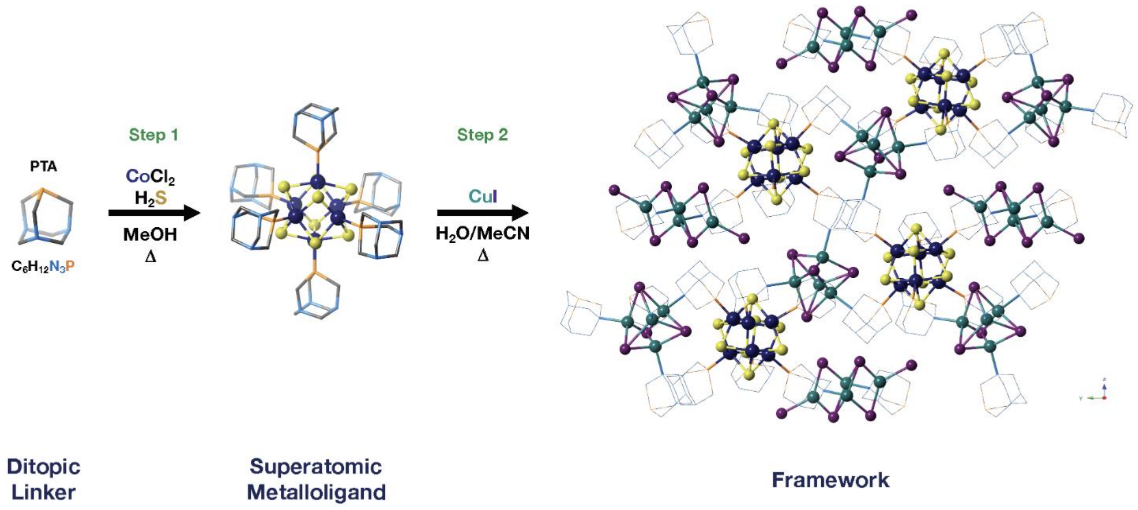

SCHEME 2.1. The stepwise reaction scheme going from the diatopic linker to the framework. The framework depicted is of the a-view with as ball and stick depiction of the clusters and wireframe PTA ligands. Color Scheme: Dark blue, cobalt; yellow, sulfur; orange, phosphorus; teal, copper; purple, iodide; light blue, nitrogen; black, carbon; hydrogens have been omitted for clarity.

core. The phosphorus-centroid-phosphorus angle of the molecular cluster averages (180.0 ± 0.0)º for opposing and (90.7 ± 1.7)º for adjacent phosphorus. The framework-based angles have an increased deviation from ideal with the average adjacent phosphorus being (89.5 ± 3.7)º and opposing being (174 ± 1.8)º (FIGURE 2.10d). These distortions most likely arise due to the steric strain of having five copper iodide clusters coordinated to the outer PTA ligands. These distortions have caused all atoms within the

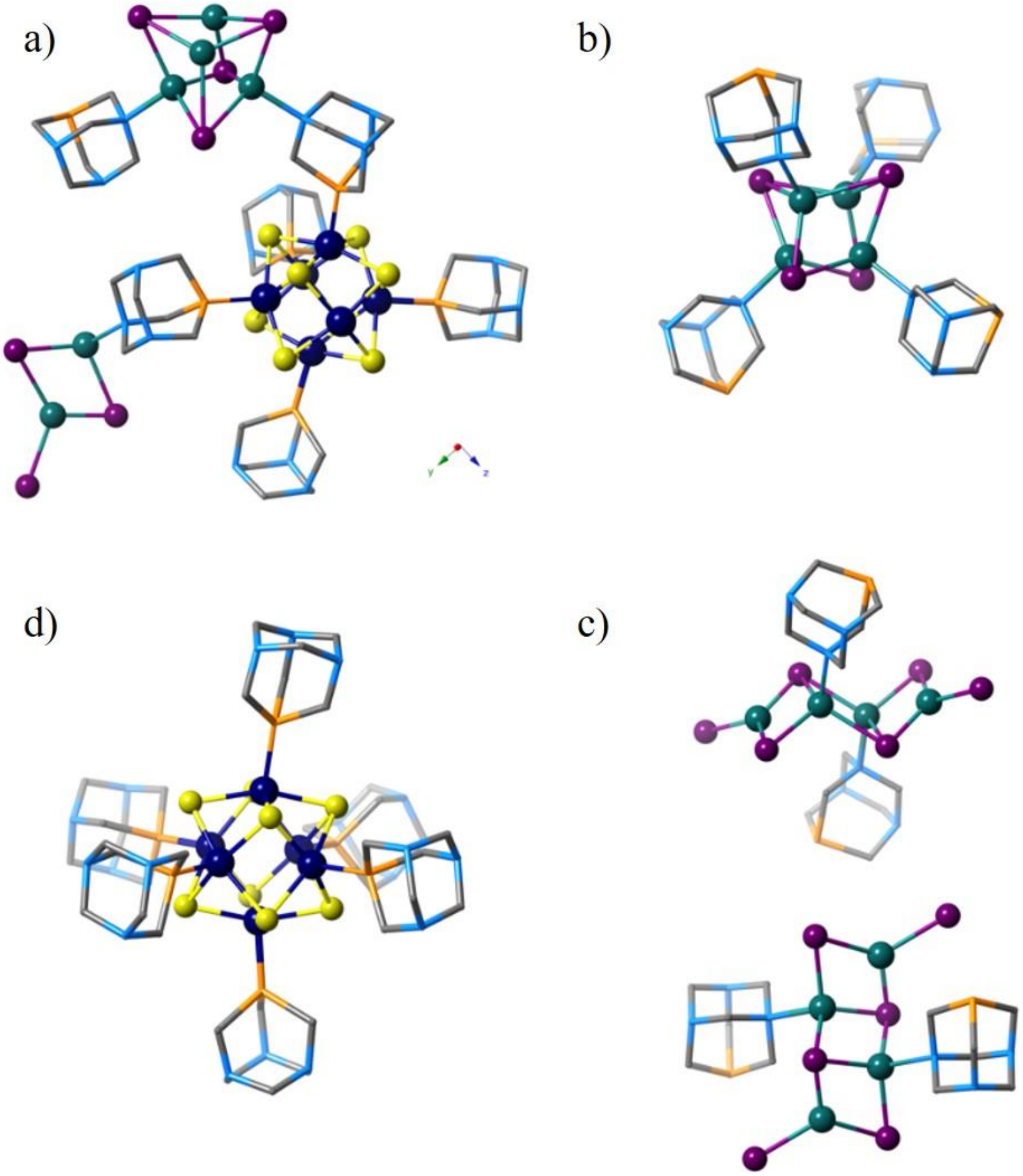

e

FIGURE 2.10. The SCXRD structure of the different clusters within **2** a) the asymmetrical unit, b) the neutral Cu_4I_4 cluster, c) the anionic $Cu_4I_6^{2-}$ ladder cluster, and d) **1** as found with distortions in the packing. Color Scheme: Dark blue, cobalt; yellow, sulfur; orange, phosphorus; teal, copper; purple, iodide; light blue, nitrogen; black, carbon; hydrogens have been omitted for clarity.

cluster to become unique with different bond lengths and angles to accommodate the imposed strain. The hexanuclear cobalt core did reflect variation from ideal geometry but was largely unchanged otherwise.

The cubane-like Cu_4I_4 cluster is a known neutral, photoluminescent active cluster with no known reversible redox processes. This cluster has an average bond angle of (109.5 ± 2.0)° within **2** which is within reason of having ideal geometry. This suggests that this cluster is not as sterically strained as the $Co_6S_8(PTA)_6{\bullet}H^+$ superatom.

The dianionic $Cu_4I_6^{2-}$ ladder-like cluster is an inorganic anion that commonly forms in the presence of protonated amines.[73] The presence of this ladder cluster is leads us to believe that the Co_6S_8 core was not oxidized, but instead that the PTA ligand was protonated. Within the structure it is tightly bound between two of the $Co_6S_8(PTA)_6{\bullet}H^+$ superatoms (FIGURE 2.10a,c).

2.2.2 Thermogravimetric Analysis

Thermogravimetric analysis was used to characterize the metalloligand and SAF stability using both an inert nitrogen atmosphere and air to gauge reactivity (FIGURE 2.11). The SAF exhibits enhanced air stability in comparison to **1**. Metalloligand **1** can be seen increasing in weight at 265 ºC shortly after decomposition began. This indicates that the cluster is reacting with oxygen since this spike is not observed when TGA is performed under an inert atmosphere. The SAF stability is dictated by the Co_6S_8 core with the decomposition of the metalloligand occurring at 205 ºC under air and at 215 ºC under an inert atmosphere.

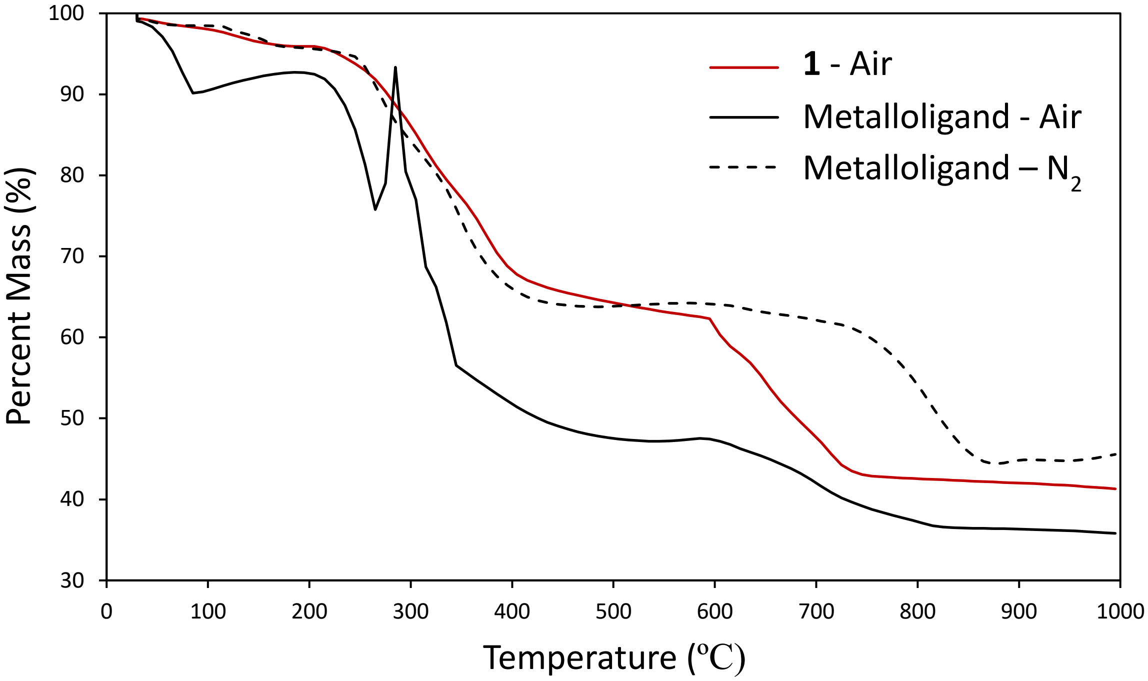

FIGURE 2.11. The thermogravimetric analysis of the metalloligand (black) and SAF **2** (red) under air (solid line) and inert atmosphere (dashed). The sample was tested from 30 – 1000 ºC at a ramp rate of 5 ºC/min.

2.2.3 Cyclic Voltammetry

The metalloligand is stable at ambient conditions as a tetrahydrochloride salt. This reactivity exhibited in the TGA curves arises from its decreasing reduction potential as the volatile HCl leaves. As such, all measurements and reactions required fresh samples. A modified GCE WE was fabricated in order to probe the electrochemical properties of the SAF. The electrode was used by drying an emulsion of 60% carbon black, 30% **2**, and 5% polyvinylidene fluoride suspended in N-methyl-2-pyrrolidone on the end of a GCE WE. Cyclic voltammetry supports the air stability of **2** based on the reduction potential ($E_{1/2}$ = 0.27 V vs Ag/AgCl) being sufficiently higher than that of diatomic oxygen (FIGURE 2.12a). The electronic environment of **2** is similar to **1** at a pH of 0 (FIGURE 2.12a). At a pH of 0, **1** has an electron deficient ligand shell due to the protonated amines creating cationic PTA ligands.

The Co_6S_8 ligand shell is suspected to be monoprotonated in **2**, however this alone should not account for the highly cathodic reduction potential observed. The bonds between the copper clusters and the PTA ligand must be dative leaving partial positive charges on the surrounding ligands. This may also account for no second oxidation being observed in **2**.

To confirm that the redox wave of interest was coming from the SAF and not the emulsion materials, two electrodes were fabricated from the same emulsion (Appendix O). The first solid state modified GCE was fabricated as normal and then the emulsion was spiked with an additional aliquot of **2** before fabricating the second. An increase in current can be seen when the two cyclic voltammograms are overlaid (FIGURE 2.12b).

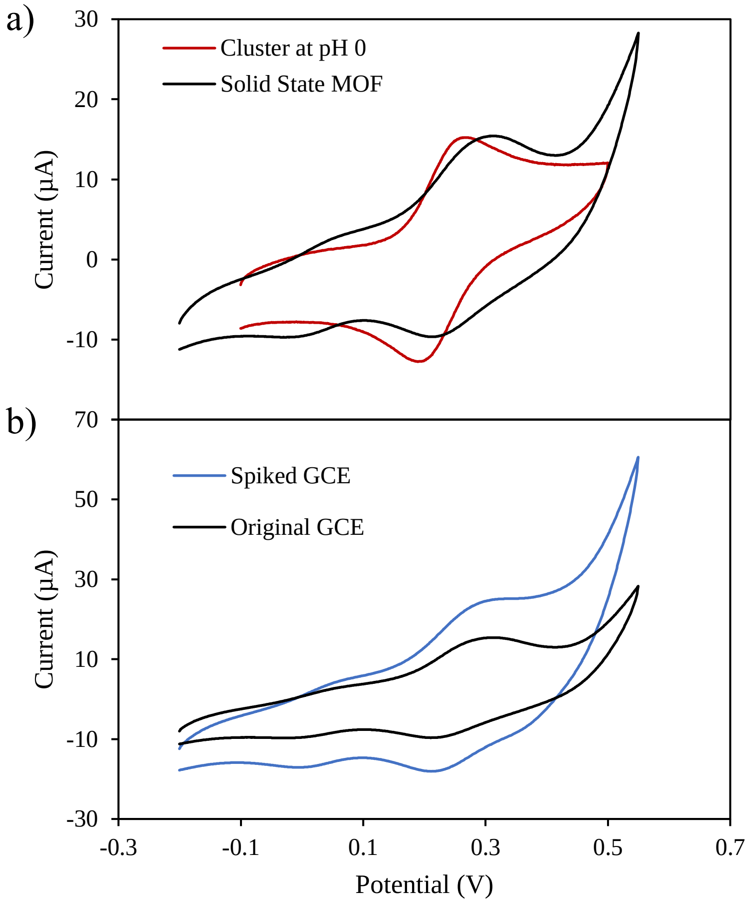

FIGURE 2.12. Cyclic voltammograms of a) **2** (black, solid state modified GCE WE, 100 mV/s, 0.5 M NaCl supporting electrolyte) and 1 mM $Co_6S_8(PTA)_6$ (red, GCE WE, 500 mV/s, 1 M HCl supporting electrolyte) and b) **2** (solid state modified GCE WE, 100 mV/s, 0.5 M NaCl supporting electrolyte) made from the same emulsion before spiking (black) and after spiking (blue). All cyclic voltammograms used a three-electrode set up referenced against a Ag/AgCl electrode with a platinum CrE. (Electrochemical windows: -0.1 to 1.0 V.)

2.2.4 Photophysical Measurements

UV-Vis diffuse reflectance was used to calculate the optical band gap of **2** in the solid state through the Kubelka-Munk function. With the reflectance (R) from within the integrating sphere being used to obtain an absorbance equivalent $(F(R))$.[91] Further transformation of the Kubelka-Munk function allows for the optical band gap (E_g) to be

$$F(R) = \frac{(1-R)^2}{2R} \tag{2.1}$$

obtained by substituting $F(R)$ in for absorbance (α) within the Tauc relation. Other constants needed for the relation are the proportionality constant (A), Plank's constant (h), and frequency (ν).[92,93] The optical band gap of **2** was calculated to be 1.98 eV. This is a band gap typically found within semiconductor materials however all observed electrical

$$\alpha h\nu = A\left(h\nu - E_g\right)^{1/2} \tag{2.2}$$

$$[F(R)h\nu]^2 = A\left(h\nu - E_g\right) \tag{2.3}$$

properties were ohmic. Comparing the absorbance of the metalloligand to **2**, there is a significant increase around 420 nm (FIGURE 2.13). This increase in absorbance at 420 nm corresponds to the copper iodide clusters which typically absorb in this area. The photoluminescence properties were also probed at various temperatures and excitation wavelengths since the copper iodide clusters are known to be strongly emissive. However, no photoluminescence was observed, which is most likely do to quenching from the Co_6S_8 cluster. Reducing and oxidizing agents were used on these films to prevent quenching; however, no emission was observed.

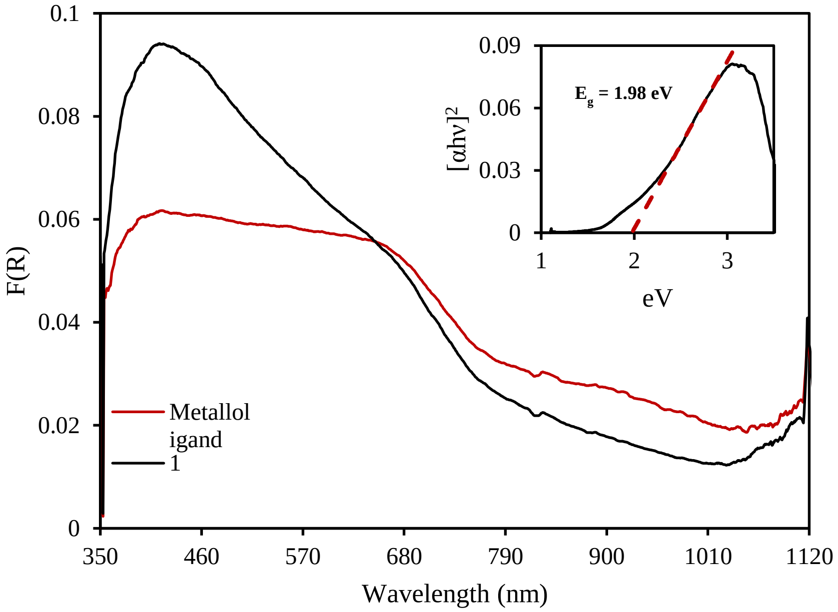

FIGURE 2.13. Absorption spectrum obtain by UV-Vis diffuse reflectance using a $BaSO_4$ background and the Kubelka-Munk transformation. The inset shows the calculated band gap based on the Tauc relation.

2.3 Experimental Details

2.3.1 General Information

All reagents were purchased from commercial sources and used as is. The following was used from the commercial suppliers: copper(I) iodide (Sigma Aldrich), $Co_6S_8(PTA)_6$•4HCl (PTA = 1,3,5-triaza-7-phosphaadamantane) was synthesized according to a literature method reported by Freeman *et al.*[9]Acetonitrile (Fisher), 2-methylpyrrolidone (Sigma) and diethyl ether (JT Baker) were bought from commercial suppliers and used as received.

Experimental details and instrumentation used is described in Appendices K-O.

2.3.2 Synthesis of **2**

$Co_6S_8(PTA)_6$•4HCl (6.0 mg, 3.5 µmol) was dissolved in deionized water (0.33 mL) and copper(I) iodide (1.34 mg, 7 µmol) was dissolved in acetonitrile (1.33 mL) followed by sonication before mixing the solutions. Upon combining the solutions, the mixture was sonicated for 60 s and sealed in a 1-dram vial before transferring to a convection oven. The reaction was allowed to react at 60 ^oC for 48 h. The black crystals that formed on the walls of the vial were collected and washed with acetonitrile (2 x 5 mL) and then diethyl ether (3 x 5 mL). The sampled was dried under vacuum to yield rhombic single crystals of **2** (2.15 mg, 26%).

2.3.3 Conclusion

As demonstrated, preformed superatomic metalloligands offer an advantageous route towards formation of heterometallic multicluster materials. This synthetic route gives control over the formation of new phosphine-based solids. Clusters such as the Co_6S_8 or previously reported Co_6Se_8 cannot be incorporated into frameworks as an SBU. By incorporating them into materials through the metalloligand approach, their properties can be integrated into functional solids.

2.3.4 Future Work

With the great diversity of phosphine ligands that exist, numerous SBUs can be used to create crystalline polymeric frameworks. A simple approach would be to continue investigating Lewis basic phosphine coordinated superatoms with an extended network formed solvothermally with copper iodide cluster SBUs (FIGURE 2.14).

Of particular interest, TDAP would have interesting Lewis basic properties. TDAP has two sp^2 hybridized nitrogens and one sp^3 hybridized nitrogen due to competition between electron donation from the nitrogen to the phosphorus and sterics. This geometry has been confirmed through SCXRD on various metal complexes.[46] The extended coordination network that forms using this ligand would favor the free, less hindered sp^3

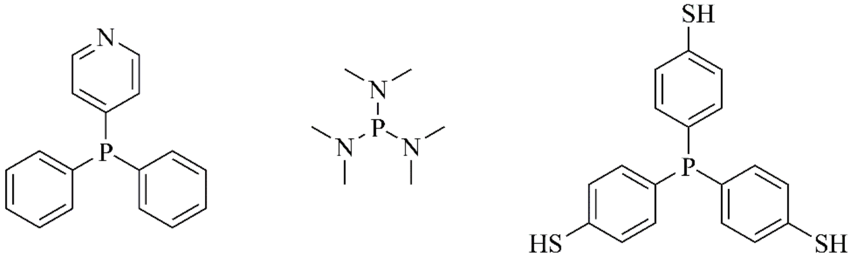

BDPP TDAP TTPP

FIGURE 2.14. Lewis basic phosphines such as 4-bis(diphenylphosphino)pyridine (BDPP), tris(dimethylamino)phosphine (TDAP), and tris(thiophenol)phosphine (TTPP).

nitrogen. The cone angle of TDAP is similar to that of triisopropylphosphine meaning that the tetranuclear metal sulfide cluster could be synthesized and included into future SAFs.

Similarly, BDPP could be used to generate an extended solid network. This solid network would be based around the hexanuclear octahedral metal sulfide cluster because of the similar cone angle to triphenylphosphine. These nitrogen-based linkers are limited to soft metals like copper(I), in which other linkers such as TTPP should be explored. Thiophenol containing phosphines would give us the ability to attempt the synthesis of heterometallic multi-chalcogenide cluster systems which have not been explored yet within the literature.

REFERENCES

(1) Alotto, P.; Guarnieri, M.; Moro, F. *Renew. Sustain. Energy Rev.* **2014**, *29*, 325–335.

(2) Bartolozzi, M. *J. Power Sources* **1989**, *27*, 219–234.

(3) Winsberg, J.; Hagemann, T.; Janoschka, T.; Hager, M. D.; Schubert, U. S. *Angew. Chemie - Int. Ed.* **2017**, *56*, 686–711.

(4) Pan, F.; Wang, Q. *Molecules* **2015**, *20*, 20499–20517.

(5) Hu, B.; DeBruler, C.; Rhodes, Z.; Liu, T. L. *J. Am. Chem. Soc.* **2017**, *139*, 1207–1214.

(6) Shibata, T.; Kumamoto, T.; Nagaoka, Y.; Kawase, K. *SEI Tech. Rev.* **2013**, *76*, 14–22.

(7) Luo, X.; Wang, J.; Dooner, M.; Clarke, J. *Appl. Energy* **2015**, *137*, 511–536.

(8) Viswanathan, V.; Crawford, A.; Stephenson, D.; Kim, S.; Wang, W.; Li, B.; Coffey, G.; Thomsen, E.; Graff, G.; Balducci, P.; et al. *J. Power Sources* **2014**, *247*, 1040–1051.

(9) Freeman, M. B.; Wang, L.; Jones, D. S.; Bejger, C. M. *J. Mater. Chem. A* **2018**, *6*, 21927–21932.

(10) Bard, A.; Faulkner, L. *Electrochemical Methods: Fundamentals and Applications. -2nd Ed.*; John Wiley: New York, 1944.

(11) Ding, Y.; Zhang, C.; Zhang, L.; Zhou, Y.; Yu, G. *Chem. Soc. Rev.* **2018**, *47*, 69–103.

(12) Xu, Y.; Wen, Y.; Cheng, J.; Cao, G.; Yang, Y. *Electrochem. commun.* **2009**, *11*, 1422–1424.

(13) Lim, H. S.; Lackner, A. M.; Knechtli, R. C. **1978**, *124*, 1154–1157.

(14) U.S. Geological Survey. *https://pubs.usgs.gov/fs/2002/fs087-02/* (Accessed July 2019).

(15) Chen, D.; Hickner, M. A.; Agar, E.; Kumbur, E. C. *J. Memb. Sci.* **2013**, *437*, 108–113.

(16) Benjamin, A.; Agar, E.; Dennison, C. R.; Kumbur, E. C. *Electrochem. commun.* **2013**, *35*, 42–44.

(17) Jing, M.; Wei, Z.; Su, W.; He, H.; Fan, X.; Qin, Y.; Liu, J.; Yan, C. *J. Power Sources* **2016**, *324*, 215–223.

(18) Goulet, M.-A.; Aziz, M. J. *J. Electrochem. Soc.* **2018**, *165*, A1466–A1477.

(19) Hagemann, T.; Winsberg, J.; Grube, M.; Nischang, I.; Janoschka, T.; Martin, N.; Hager, M. D.; Schubert, U. S. *J. Power Sources* **2018**, *378*, 546–554.

(20) Lin, K.; Chen, Q.; Gerhardt, M. R.; Tong, L.; Kim, S. B.; Eisenach, L.; Valle, A. W.; Hardee, D.; Gordon, R. G.; Aziz, M. J.; et al.*Science.* **2015**, *349*, 1529–1532.

(21) Kwabi, D. G.; Lin, K.; Ji, Y.; Kerr, E. F.; Goulet, M. A.; De Porcellinis, D.; Tabor, D. P.; Pollack, D. A.; Aspuru-Guzik, A.; Gordon, R. G.; et al. *Joule* **2018**, *2*, 1894–1906.

(22) Leung, P.; Shah, A. A.; Sanz, L.; Flox, C.; Morante, J. R.; Xu, Q.; Mohamed, M. R.; Ponce de León, C.; Walsh, F. C. *J. Power Sources* **2017**, *360*, 243–283.

(23) Hwang, B.; Park, M.-S.; Kim, K. *Chem Sus Chem* **2015**, *8*, 310–314.

(24) Chen, Z. *J. Clust. Sci.* **1995**, *6*, 357–377.

(25) Goddard, C. A.; Long, J. R.; Holm, R. H. *J Chem Soc Dalt. Trans* **1987**, *35*, 831.

(26) Sokolov, M. N.; Anyushin, A. V.; Virovets, A. V.; Mirzaeva, I. V.; Zakharchuk, N. F.; Fedin, V. P. *Inorg. Chem. Commun.* **2011**, *14*, 1659–1660.

(27) Deng, L.; Bill, E.; Wieghardt, K.; Holm, R. H. *J. Am. Chem. Soc.* **2009**, *131*, 11213–11221.

(28) Hong, M.; Huang, Z.; Lei, X.; Wei, G.; Kang, B.; Liu, H. *Polyhedron* **1991**, *10*, 927–934.

(29) Berti, E.; Cecconi, F.; A. Ghilardi, C.; Midollini, S.; Orlandini, A. *Inorg. Chem. Commun.* **1999**, *2*, 146–148.

(30) Goh, C.; Segal, B. M.; Huang, J.; Long, J. R.; Holm, R. H. *J. Am. Chem. Soc.* **1996**, *118*, 11844–11853.

(31) Ye, H.; Rouault, T. A. *Biochemistry* **2010**, *49*, 4945–4956.

(32) Pohl, B. S.; Opitz, U. *Angew. Chemie - Int. Ed.* **1993**, *32*, 863–864.

(33) Hoffman, B. M.; Lukoyanov, D.; Yang, Z.-Y.; Dean, D. R.; Seefeldt, L. C. *Chem. Rev.* **2014**, *114*, 4041–4062.

(34) Span, I.; Gräwert, T.; Bacher, A.; Eisenreich, W.; Groll, M. *J. Mol. Biol.* **2012**, *416*, 1–9.

(35) Cecconi, F.; Ghilardi, C. A.; Midollini, S.; Orlandini, A.; Zanello, P. *J. Chem. Soc., Dalt. Trans.* **1987**, *4*, 831–835.

(36) Cecconi, F.; Ghilardi, C. A.; Midollini, S.; Orlandini, A. *Inorganica Chim. Acta* **1991**, *184*, 141–145.

(37) Britvin, S. N.; Lotnyk, A. *J. Am. Chem. Soc.* **2015**, *137*, 5526–5535.

(38) Long, J. R.; Holm, R. H. *J. Am. Chem. Soc.* **1994**, *116*, 9987–10002.

(39) Saito, T.; Yamamoto, N.; Nagase, T.; Tsuboi, T.; Kobayashi, K.; Yamagata, T.; Imoto, H.; Unoura, K. *Inorg. Chem.* **1990**, *29*, 764–770.

(40) Bencini, A.; Palii, A. V.; Ostrovsky, S. M.; Tsukerblat, B. S.; Uytterhoeven, M. G. *Mol. Phys.* **1995**, *86*, 1085–1097.

(41) Anyushin, A. V.; Korotaev, E. V.; Andreeva, A. Y.; Ryzhikov, M. R.; Mainichev, D. A.; Sokolov, M. N.; Fedin, V. P. *Russ. Chem. Bull.* **2016**, *65*, 173–180.

(42) Anyushin, A. V.; Sokolov, M. N.; Virovets, A. V.; Zakharchuk, N. F.; Mainichev, D. A.; Fedin, V. P. *Inorg. Chem. Commun.* **2012**, *24*, 225–226.

(43) Moiseev, D. V.; James, B. R. *Inorganica Chim. Acta* **2011**, *379*, 23–27.

(44) Joó, F.; Kovács, J.; Kathó, Á.; C.Bényei, A.; Decuir, T.; Dubois, D. J. Inorganic Syntheses; Darensbourg, M. Y., Ed.; Wiley: New York, 1998; Vol. 32; p 40.

(45) Darensbourg, D. J.; Ortiz, C. G.; Kamplain, J. W. *Organometallics* **2004**, *23*, 1747–1754.

(46) Moloy, K. G.; Peterser, J. L.; Moloy, K. G. *J. Am. Chem. Soc.* **1995**, *117*, 7696–7710.

(47) Phillips, A. D.; Gonsalvi, L.; Romerosa, A.; Vizza, F.; Peruzzini, M. *Coord. Chem. Rev.* **2004**, *248*, 955–993.

(48) Cecconi, F.; Ghilardi, C. A.; Midollini, S.; Orlandini, A.; Zanello, P. *Polyhedron* **1986**, *5*, 2021–2031.

(49) Fenske, D.; Hachgenei, J.; Ohmer, J. *Angew. Chemie Int. Ed. English* **1985**, *24*, 706–709.

(50) Schubert, E. M. *J. Chem. Educ.* **1992**, *69*, 62.

(51) Pinal, R. *Org. Biomol. Chem.* **2004**, *2*, 2692–2699.

(52) Matsumoto, T.; Namiki, R.; Chang, H.-C. *Eur. J. Inorg. Chem.* **2018**, *2018*, 3900–3904.

(53) Nicholson, R. S. *Anal. Chem.* **1965**, *37*, 1351–1355.

(54) Vangelder, L. E.; Kosswattaarachchi, A. M.; Forrestel, P. L.; Cook, T. R.; Matson, E. M. *Chem. Sci.* **2018**, *9*, 1692–1699.

(55) Friedl, J.; Lebedeva, M. A.; Porfyrakis, K.; Stimming, U.; Chamberlain, T. W. *J. Am. Chem. Soc.* **2018**, *140*, 401–405.

(56) Roland, B. K.; Selby, H. D.; Carducci, M. D.; Zheng, Z. *J. Am. Chem. Soc.* **2002**, *124*, 3222–3223.

(57) Scott, T. A.; Zhou, H.-C. *Angew. Chemie Int. Ed.* **2004**, *43*, 5628–5631.

(58) Fedin, V. P.; Kalinina, I. V.; Samsonenko, D. G.; Mironov, Y. V.; Sokolov, M. N.; Tkachev, S. V.; Virovets, A. V.; Podberezskaya, N. V.; Elsegood, M. R. J.; Clegg, W.; et al. *Inorg. Chem.* **2002**, *38*, 1956–1965.

(59) Lee, W.-K.; Odom, T. W. *ACS Nano* **2019**, *13*, 6170-6177.

(60) Jiang, H.-L.; Makal, T. A.; Zhou, H.-C. *Coord. Chem. Rev.* **2013**, *257*, 2232–2249.

(61) Ball, J. M.; Petrozza, A. *Nat. Energy* **2016**, *1*, 16149.

(62) Pinkard, A.; Champsaur, A. M.; Roy, X. *Acc. Chem. Res.* **2018**, *51*, 919–929.

(63) Leong, W. L.; Vittal, J. J. *Chem. Rev.* **2011**, *111*, 688–764.

(64) Sun, L.; Park, S. S.; Sheberla, D.; Dincă, M. *J. Am. Chem. Soc.* **2016**, *138*, 14772–14782.

(65) Li, S.; Wang, Y.; Qi, C.; Zhao, X.; Zhang, J.; Zhang, S.; Pang, S. *Angew. Chemie - Int. Ed.* **2013**, *52*, 14031–14035.

(66) Shan, X.; Jiang, F.; Yuan, D.; Zhang, H.; Wu, M.; Chen, L.; Wei, J.; Zhang, S.; Pan, J.; Hong, M. *Chem. Sci.* **2013**, *4*, 1484.

(67) Roy, X.; Lee, C. H. C.-H.; Crowther, A. C.; Schenck, C. L.; Besara, T.; Lalancette, R. A.; Siegrist, T.; Stephens, P. W.; Brus, L. E.; Kim, P.; et al. *Science.* **2013**, *341*, 157–160.

(68) Turkiewicz, A.; Paley, D. W.; Besara, T.; Elbaz, G.; Pinkard, A.; Siegrist, T.; Roy, X. *J. Am. Chem. Soc.* **2014**, *136*, 15873–15876.

(69) Green, M. L. H.; Hamnett, A.; Qin, J.; Baird, P.; Bandy, J. A.; Prout, K.; Marseglia, E.; Obertelli, S. D. *J. Chem. Soc. Chem. Commun.* **1987**, *4*, 1811–1814.

(70) Shott, J. L.; Freeman, M. B.; Saleh, N. A.; Jones, D. S.; Paley, D. W.; Bejger, C. *Inorg. Chem.* **2017**, *56*, 10984–10990.

(71) Schulz-Dobrick, M.; Jansen, M. *Angew. Chemie - Int. Ed.* **2008**, *47*, 2256–2259.

(72) Fang, W.-H.; Wang, J.-F.; Zhang, L.; Zhang, J. *Chem. Mater.* **2017**, *29*, 2681–2684.

(73) Liu, W.; Fang, Y.; Li, J. *Adv. Funct. Mater.* **2018**, *28*, 1705593.

(74) Wang, X. L.; Qin, C.; Wang, E. B.; Su, Z. M.; Li, Y. G.; Xu, L. *Angew. Chemie - Int. Ed.* **2006**, *45*, 7411–7414.

(75) Vitale, M.; Palke, W. E.; Ford, P. C. *J. Phys. Chem.* **1992**, *96*, 8329–8336.

(76) Wang, Z.; Cohen, S. M. *Chem. Soc. Rev.* **2009**, *38*, 1315.

(77) Bosch, M.; Yuan, S.; Rutledge, W.; Zhou, H. C. *Acc. Chem. Res.* **2017**, *50*, 857–865.

(78) Shakirova, J. R.; Grachova, E. V.; Gurzhiy, V. V.; Thangaraj, S. K.; Jänis, J.; Melnikov, A. S.; Karttunen, A. J.; Tunik, S. P.; Koshevoy, I. O. *Angew. Chemie - Int. Ed.* **2018**, *57*, 14154–14158.

(79) Kandiah, M.; Nilsen, M. H.; Usseglio, S.; Jakobsen, S.; Olsbye, U.; Tilset, M.; Larabi, C.; Quadrelli, E. A.; Bonino, F.; Lillerud, K. P. *Chem. Mater.* **2010**, *22*, 6632–6640.

(80) Pullen, S.; Fei, H.; Orthaber, A.; Cohen, S. M.; Ott, S. *J. Am. Chem. Soc.* **2013**, *135*, 16997–17003.

(81) Zheng, S.-T. T.; Zhao, X.; Lau, S.; Fuhr, A.; Feng, P.; Bu, X. *J. Am. Chem. Soc.* **2013**, *135*, 10270–10273.

(82) Srivastava, S.; Gupta, R. *CrystEngComm* **2016**, *18*, 9185–9208.

(83) Hao, L.; Lu, Y.; He, Z.-Z.; Liu, Z.; Wang, E. *Inorg. Chem. Commun.* **2015**, *55*, 88–91.

(84) Mohapatra, C.; Chandrasekhar, V. *Cryst. Growth Des.* **2014**, *14*, 406–409.

(85) Li, D.-J.; Mo, L.-Q.; Wang, Q.-M. *Inorg. Chem. Commun.* **2011**, *14*, 1128–1131.

(86) Buser, H. J.; Ludi, A.; Schwarzenbach, D.; Petter, W. *Inorg. Chem.* **1977**, *16*, 2704–2710.

(87) Song, Y. F.; Tsunashima, R. *Chem. Soc. Rev.* **2012**, *41*, 7384–7402.

(88) Pope, M. T.; Müller, A. *Angew. Chemie Int. Ed. English* **1991**, *30*, 34–48.

(89) Li, X. X.; Wang, Y. X.; Wang, R. H.; Cui, C. Y.; Tian, C. Bin; Yang, G. Y. *Angew. Chemie - Int. Ed.* **2016**, *55*, 6462–6466.

(90) Champsaur, A. M.; Yu, J.; Roy, X.; Paley, D. W.; Steigerwald, M. L.; Nuckolls, C.; Bejger, C. M. *ACS Cent. Sci.* **2017**, *3*, 1050–1055.

(91) Cordon, G. B.; Lagorio, M. G. *J. Chem. Educ.* **2009**, *84*, 1167.

(92) Abdullahi, S. S.; Güner, S.; Koseoglu, Y.; Murtala, I.; Adamu, B. I.; Abdulhamid, M. I. *J. Niger. Assoc. Math. Phys.* **2016**, *35*, 241–246.

(93) Barras, A.; Cordier, S.; Boukherroub, R. *Appl. Catal. B Environ.* **2012**, *123–124*, 1–8.

(94) Konopka, S. J.; McDuffie, B. *Anal. Chem.* **1970**, *42*, 1741–1746.

(95) Deblase, C. R.; Silberstein, K. E.; Truong, T. T.; Abruña, H. D.; Dichtel, W. R. *J. Am. Chem. Soc.* **2013**, *135*, 16821–16824.

APPENDIX A: INSTRUMENTATION & DATA COLLECTION FOR $Co_6S_8(PTA)_6•4HCl$

Ultraviolet-visible Spectroscopy

UV-vis spectra were obtained on a Cary 300 UV-vis spectrophotometer with quartz cells (1 cm path length) with all solutions made using volumetric glassware and micropipettes. The samples were prepared under ambient conditions.

Electrochemical Measurements

All electrochemical measurements were obtained on a Gamry 1000E potentiostat and were recorded on Gamry Framework Software (Version 7.02). Analysis of the data was done using Gamry Echem Analyst (Version 7.02).

Static Electrochemical Measurements

For cyclic voltammetry and chronoamperometry, a three-electrode set up was used with a BASi glassy carbon working electrode, silver wire as the counter electrode, and a Ag/AgCl quasireference electrode.

Galvanostatic Half Cell Cyclic Charge Discharge

An Adam & Chittenden H cell (8 mL) was used with a Selemion AMV anion exchange membrane and sealed with a Viton rubber O-ring. Graphite felt electrodes (Fuel Cell Store) were cut and placed into an oven at 200 ^oC for 1 h before use. The graphite felt electrodes were submerged to have a surface area of (1 mm x 10 mm x 3mm). The half-cell was referenced versus Ag/AgCl quasireference electrode.

Galvanostatic Full Cell Cyclic Charge Discharge

An Adam & Chittenden H-cell (8 mL) was used with a Selemion AMV anion exchange membrane and sealed with a Kalrez Perfluoroelastomer O-ring (DuPont). Solid graphite electrodes were cut and dried at 200 ^{o}C before use. The graphite electrodes were submerged to have a surface area of (1 mm x 10 mm x 3mm). The cell was sparged for an hour with water-saturated argon and tested under an argon atmosphere. The H cell was stirred vigorously during charge-discharge measurements.

APPENDIX B: CRYSTAL DATA FOR $Co_6S_8(PTA)_6$•4HCl

TABLE 1. Crystal Data of **1**

Identification code	UNCC_Co6S8_PTA6
Empirical formula	$C_{36}H_{76}Cl_4Co_6N_{18}P_6S_8$
Formula weight	1698.84
Temperature/K	100(2)
Crystal system	orthorhombic
Space group	Cmca
a/Å	23.1218(19)
b/Å	10.7247(9)
c/Å	24.0502(17)
α/°	90
β/°	90
γ/°	90
Volume/$Å^3$	5963.8(8)
Z	4
ρcalc g/cm^3	1.892
μ/mm^{-1}	2.301
F(000)	3464
Crystal size/mm^3	0.1 × 0.05 × 0.02
Radiation	Mo Kα (λ = 0.71073 Å)
2Θ range for data collection/°	6.58 to 50
Index ranges	$-29 \leq h \leq 21$, $-9 \leq k \leq 14$, $-31 \leq l \leq 31$
Reflections collected	10020
Independent reflections	2694 [Rint = 0.0733, Rsigma = 0.0932]
Data/restraints/parameters	2694/0/191
Goodness-of-fit on F^2	1.059
Final R indexes [I>=2σ (I)]	R1 = 0.0489, wR2 = 0.1040
Final R indexes [all data]	R1 = 0.0749, wR2 = 0.1136
Largest diff. peak/hole / e $Å^{-3}$	0.84/-0.68

APPENDIX C: SOLUBILITY EXPERIMENTS FOR $Co_6S_8(PTA)_6$•4HCl

*Solubility of $Co_6S_8(PTA)_6$•4HCl (**1**) in water*

A 0.233 mM working stock solution of **1** (9.9 mg, 5.82 mmol) was prepared in water (25.00 mL). A quartz cell was filled with DI water (4.00 mL) and the UV-vis spectrum was recorded. The quartz cell was then spiked with the working stock solution (40 µL) six times with the UV-vis spectrum acquired after each spike at λ = 262 nm. A calibration curve was obtained by plotting the absorbances against concentration. A supersaturated solution was obtained by sonicating an excess of solid in 1 mL which was then allowed to sit overnight to equilibrate. An aliquot from the supersaturated solution (10 µL) was diluted to 25 mL and then diluted again (1 mL to 5 mL) to reach the linear range of the calibration curve.

*Solubility of $Co_6S_8(PTA)_6$•4HCl (**1**) at pH 1*

A 0.257 mM working stock solution of **1** (4.36 mg, 2.57 mmol) was prepared in a solution of pH 1 with HCl (10.00 mL). A quartz cell was filled with DI water (4.00 mL) and the UV-vis spectrum was recorded. The quartz cell was then spiked with the working stock solution (40 µL) seven times with the UV-vis spectrum acquired after each spike at λ = 338 nm. A calibration curve was obtained by plotting the absorbances against concentration. A supersaturated solution was obtained by sonicating an excess of solid in 1 mL which was then allowed to sit overnight to equilibrate. An aliquot from the supersaturated solution (5 µL) was diluted to 25 mL and then used as Unknown 1. An aliquot (2 mL) of the 25 mL solution was diluted to 4 mL and used as Unknown 2. Both unknowns fell on the linear range and the saturation point of the solution was calculated as the average.

APPENDIX D: WATERGATE ^{1}H NMR SPECTRUM OF $Co_6S_8(PTA)_6$•4HCl
(D_2O, 500 MHz, 25 ^oC)

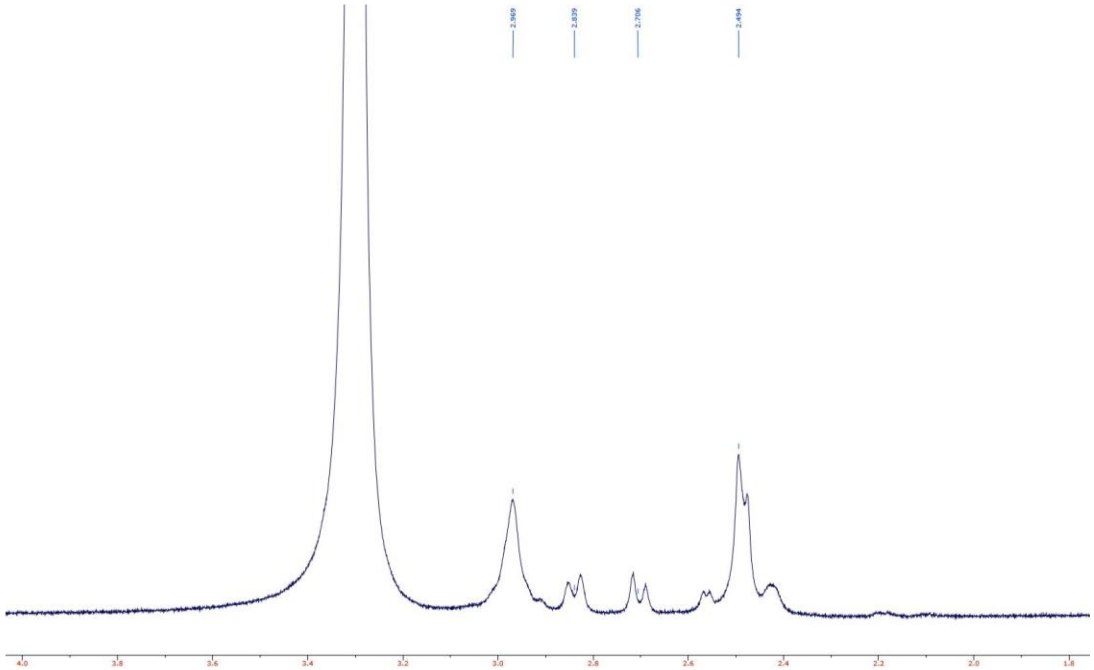

APPENDIX E: WATERGATE ^{1}H NMR SPECTRUM OF $Co_6S_8(PTA)_6$•4HCl (D_2O/Sat K_2CO_3, 500 MHz, 25 °C)

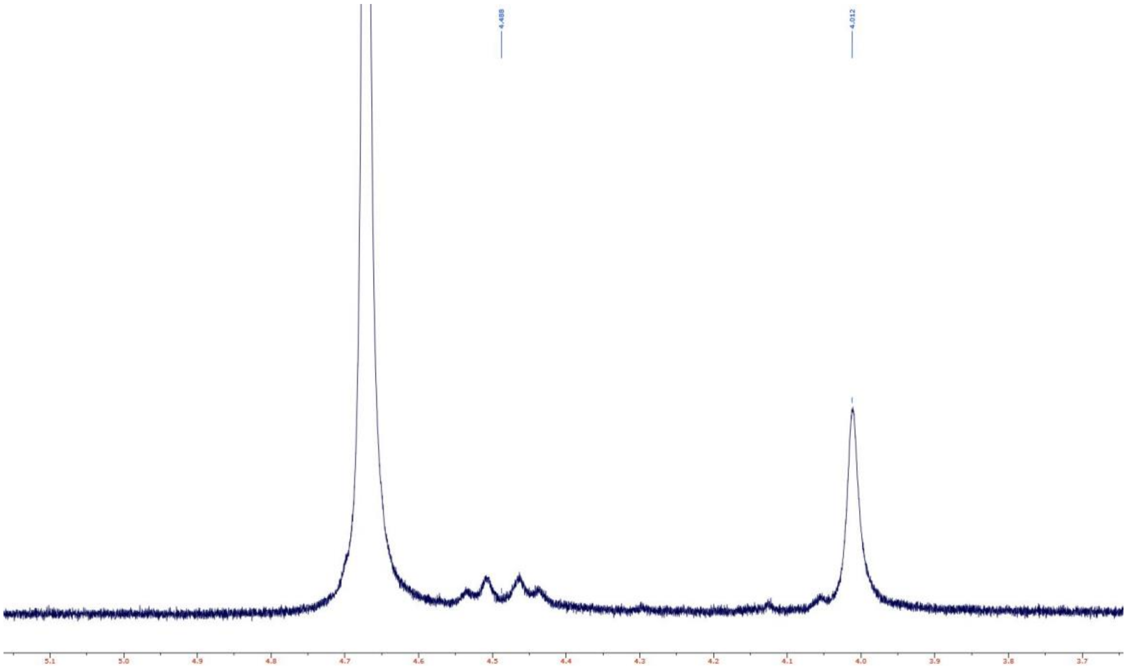

APPENDIX F: ^{31}P NMR OF $Co_6S_8(PTA)_6{\bullet}4HCl$ (D_2O, 500 MHz, 25 ^{o}C).

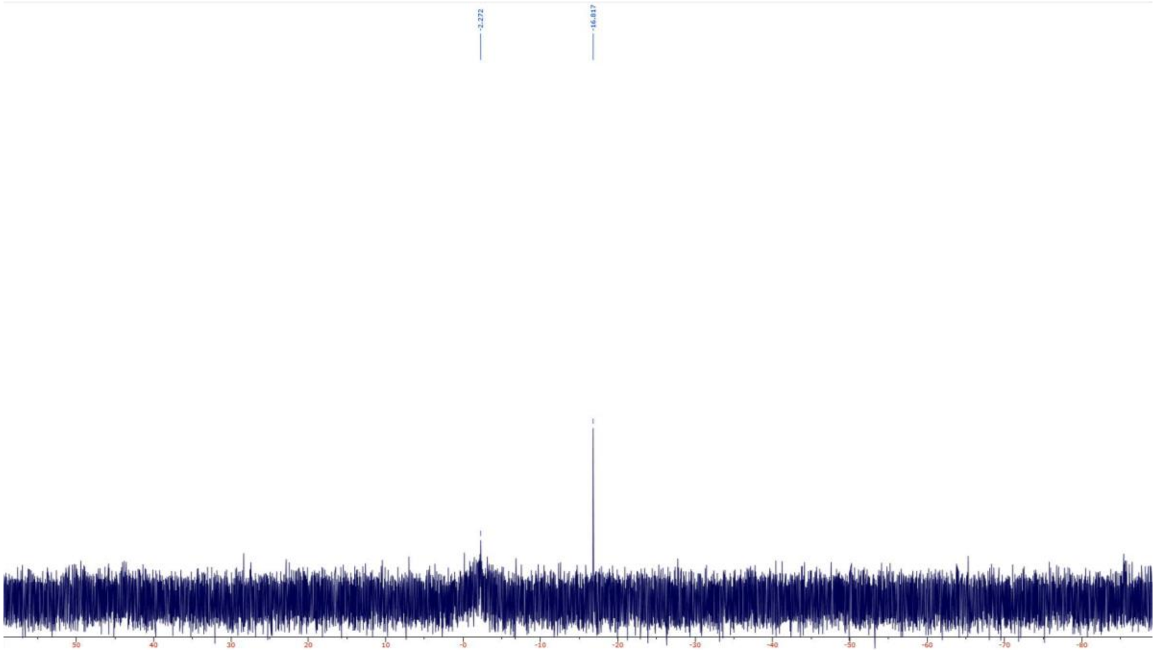

APPENDIX G: EVANS METHOD SAMPLE PREPARATION

A concentrated solution of **1** was made using a standard solution of 35% DCl in D_2O. A sealed capillary of the pure 35% DCl solution was added to the NMR tube and the spectrum was ran. Only one DCl signal was observed.

APPENDIX H: ELECTROCHEMICAL CONSTANT EXPERIMENTS

Diffusion Coefficients

A BASi glassy electrode (GC) working electrode (WE) was polished with alumina on a felt surface and the had its area standardized by chronoamperometry by using the known diffusion coefficient of $K_3Fe(CN)_6$ following conditions from previously reported literature.[94] The same electrodes were rinsed and then used at varying scan rates (ν) in a solution of 1 (1 mM) with NaCl (0.5 M) as the supporting electrolyte. The same method was applied while studying 1 (1 mM) with HCl (1.0 M) as the supporting electrolyte. By applying the Randles-Sevcik (EQUATION 1.4), the diffusion coefficient (D) of 1 was found at room temperature (T) for both the mono (water and acid) and dicationic species (water only).

Electron Transfer Coefficients

A BASi glassy electrode (GC) working electrode (WE) was polished with alumina on a felt surface. The scan rates were varied in a solution of **1** (1 mM) with NaCl (0.5 M) as the supporting electrolyte. The same method was applied while studying **1** (1 mM) with HCl (1.0 M) as the supporting electrolyte. The peak separation (ΔE_p) was measured as a function of scan rate and then used to find the dimensionless rate parameter (ψ) using the Nicholson method[53] assuming α = 0.5. The electron transfer rate coefficient (k^0) was calculated (EQUATION 1.5) by plotting the ψ as a function of the inverse square root of the scan rate ($\nu^{-1/2}$).

APPENDIX I: HALF-CELL PARAMETERS WITH THEORETICAL CAPACITY CALCULATION SAMPLE

Half Cell Experiments

A 1 mM aqueous stock solution (10 mL) of **1** (17.1 mg, 10 mmol) with NaCl (0.5846 g, 10.0 mmol) was made. The stock solution of **1** (4 mL) was pipetted into each side of the H-cell. The theoretical capacity (C_p) was calculated to find the capacity at an 80% state of charge (SOC) using EQUATION 2 based on solution volume (V), concentration (C), number of electrons transferred (n), and Faradays constant (F).

$$C_p = \frac{1000VCnF}{3600}$$

Theoretical Capacity:

-From Co_6S_8 to $Co_6S_8^{1+}$

$$Cp \ = \frac{\left(1000\ \frac{mA}{A}\right) * (0.004\ L) * (0.001\ M) * (1\ e^{-}) * \left(96485 \frac{C}{mol}\right)}{3600\ \frac{s}{h}}$$

$$C_p = 0.107\ mAh$$

$$80\%\ SOC = \ 0.085\ mAh$$

Set Experimental Parameters:

Charging current was set to 28.5 µA for 3 h and the discharging current was set for 21 µA for 4 h with cut off voltages at 0.12 and -0.1 V, respectively.

-From Co_6S_8 to $Co_6S_8^{2+}$

$$Cp = \frac{\left(1000\ \frac{mA}{A}\right) * (0.004\ L) * (0.001\ M) * (2\ e^{-}) * \left(96485\frac{C}{mol}\right)}{3600\ \frac{s}{h}}$$

$$C_p = 0.214\ mAh$$

$$80\%\ SOC = 0.171\ mAh$$

Set Experimental Parameters:

Charging current was set to 85.6 µA for 2 h and the discharging current was set for 43 µA for 3 h with cut off voltages at 0.7 and -0.25 V, respectively.

APPENDIX J: FULL CELL EXPERIMENT

A 2.5 mM aqueous solution (25 mL) of methyl viologen hydrate (17.2 mg $MV^{2+} \bullet H_2O$, 62.5 μmol) used as the cell anolyte. The anolyte (5 mL) consisted of NaCl (0.2922 g, 5.0 mmol) and the methyl viologen solution. The cathylote is a 2.5 mM aqueous solution (5 mL) of **1** (21.2 mg, 12.5 μmol) and NaCl (0.2922 g, 5.0 mmol). The H Cell was assembled in atmosphere with 4 mL of the anolyte and catholyte added to each side and was sparged with water-saturated argon for one hour before cycling experiments. The cell was tested at 80% SOC.

Set Experimental Parameters:

Charging current was set to 107 μA for 2 h and the discharging current was set to 71 μA for 3 h with cut off voltages at 0.1 and 1.2 V, respectively. The theoretical capacity is 0.268 mAh with a capacity of 0.214 mAh at 80% SOC.

APPENDIX K: INSTRUMENTATION & DATA COLLECTION FOR $2[Co_6S_8(PTA)_6H^+]2[Cu_4I_4][Cu_4I_6^{2-}]$

Diffuse Reflectance Spectroscopy

Diffuse reflectance data was measured using Oriel Integrating Sphere with a Thermo Oriel 50-500W Xenon Lamp with a light intensity set to150 W. All data was collected against a $BaSO_4$ background. The collected data was obtained and exported from SpectraSuite Software (Version 6.1).

Thermogravimetric Analysis

Thermogravimetric analysis was performed using a Mettler Toledo TGA/SDTA851^e supplied by Al 300 compressed air. Data analysis was done using STARe Software (Version 9.01).

Electrochemical Measurements

All electrochemical measurements were obtained on a Gamry 1000E potentiostat and were recorded on Gamry Framework Software (Version 7.02). Analysis of the data was done using Gamry Echem Analyst (Version 7.02).

Static Electrochemical Measurements

For cyclic voltammetry, a three-electrode set up was used with a BASi glassy carbon working electrode, platinum as the counter electrode, and a Ag/AgCl quasireference electrode.

Scanning Electron Microscopy

Images were obtained on a JEOL JSM-6460LV SEM instrument using a 10 kV accelerating voltage while collecting data through SEM Control User Interface (Version 6.21).

Powder X-Ray Diffraction

Powder X-Ray Diffraction patterns were obtained using a PANalytical's X'Pert PRO Materials Research Diffractometer with data collected and worked up on X'Pert Data Collector (Version 2.2).

APPENDIX L: CRYSTAL DATA FOR $2[Co_6S_8(PTA)_6H^+]2[Cu_4I_4][Cu_4I_6^{2-}]$

TABLE 1. Crystal Data of **2**

Identification code	MK_MF11618_Mo_X1_cold_Le
Empirical formula	$C_{30}H_{73}Co_6Cu_6I_7N_{18}P_6S_8$
Formula weight	2823.60
Temperature/K	100(2)
Crystal system	monoclinic
Space group	$P2_1/n$
a/Å	12.6827(7)
b/Å	23.6684(13)
c/Å	25.2736(18)
α/°	90
β/°	103.392
γ/°	90
Volume/Å^3	7380.3(8)
Z	5
ρcalc g/cm^3	2.5447
μ/mm^{-1}	6.329
F(000)	5388.7
Crystal size/mm^3	0.19 × 0.07 × 0.06
Radiation	Mo Kα (λ = 0.71073 Å)
2Θ range for data collection/°	6.6 to 50
Index ranges	$-17 \leq h \leq 12$, $-26 \leq k \leq 31$, $-27 \leq l \leq 32$
Reflections collected	31418
Independent reflections	12898 [Rint = 0.0879, Rsigma = 0.1980]
Data/restraints/parameters	12898/200/784
Goodness-of-fit on F^2	0.986
Final R indexes [I>=2σ (I)]	R1 = 0.1015, wR2 = 0.2567
Final R indexes [all data]	R1 = 0.1723, wR2 = 0.3048
Largest diff. peak/hole / e Å^{-3}	11.82/-7.86

APPENDIX M: POWDER X-RAY DIFFRACTION (PXRD)

Crystals of the metalloligand and **2** were isolated and cleaned as reported. PXRD samples were prepared by drop-casting the crystals out of diethyl ether onto a warm glass slide. Each of the samples were mounted onto an aluminum stage and aligned before the measurement began. The PXRD pattern of **2** (top) and the metalloligand (bottom) plotted against their predict pattern (black).

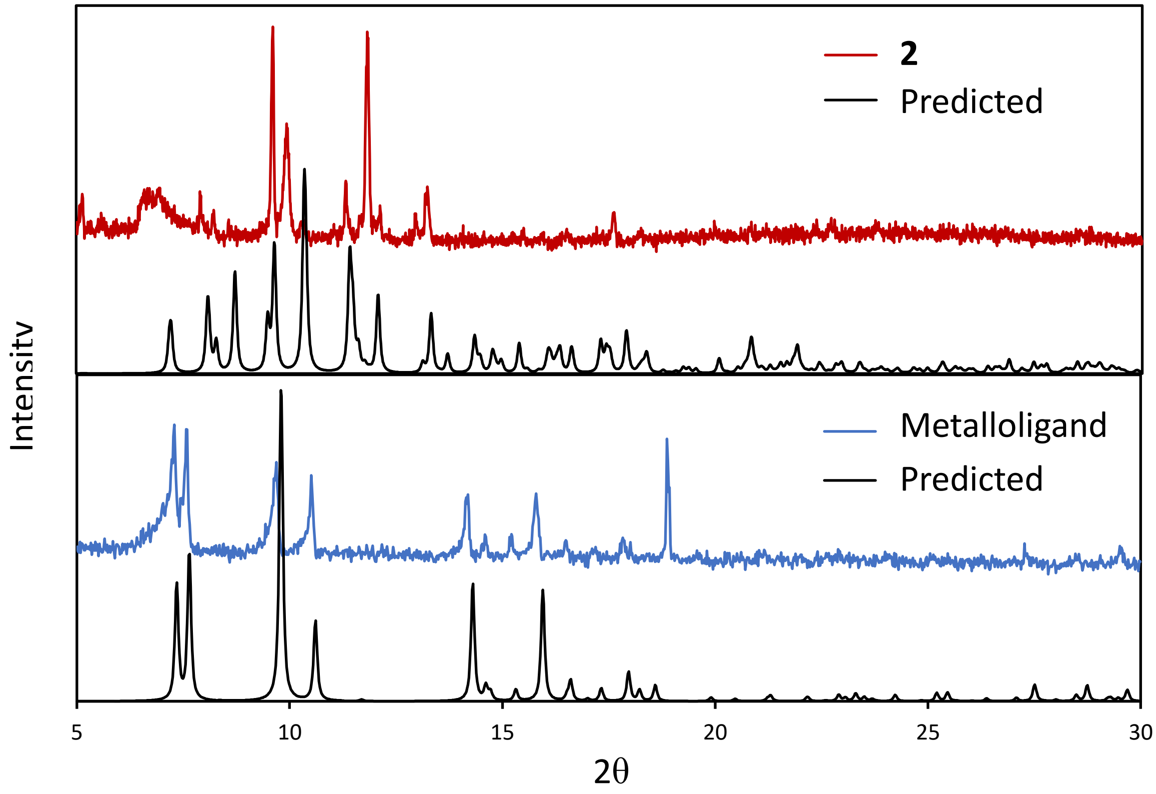

APPENDIX N: SCANNING ELECTRON MICROSCOPY IMAGES OF $2[Co_6S_8(PTA)_6H^+]2[Cu_4I_4][Cu_4I_6^{2-}]$

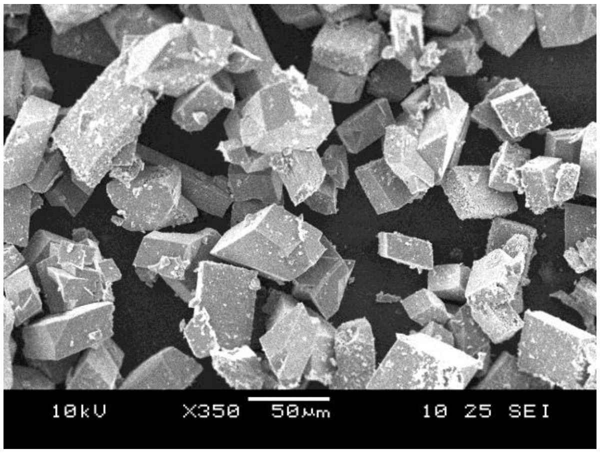

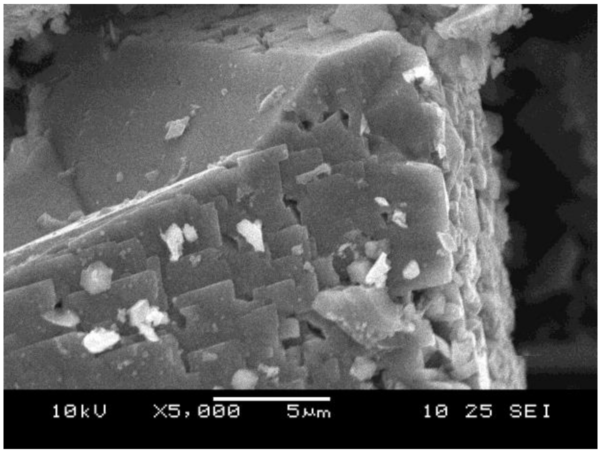

APPENDIX O: MODIFIED GLASSY CARBON ELECTRODE WITH $2[Co_6S_8(PTA)_6H^+]2[Cu_4I_4][Cu_4I_6^{2-}]$

Modified glassy carbon electrodes were fabricated using a similar preparation for covalent organic frameworks within the literature.[95] An emulsion of carbon black, polyvinylidene fluoride, and **2** (65:5:30 w/w) were finely ground with NMP (5 drops). The surface of the glassy carbon electrode was coated with 1 drop of the emulsion and dried overnight under vacuum. An additional glassy carbon electrode was fabricated by spiking the same emulsion with an additional amount of **2**.